NONLINEAR XFEM MODELING OF DELAMINATION IN FIBER REINFORCED COMPOSITES CONSIDERING UNCERTAIN FRACTURE PROPERTIES AND EFFECT OF FIBER BRIDGING

by

Damoon Motamedi

B.Sc., The University of Tehran, 2006

M.Sc., The University of Tehran, 2008

A THESIS SUBMITTED IN PARTIAL FULFILLMENT OF

THE REQUIREMENTS FOR THE DEGREE OF

DOCTOR OF PHILOSOPHY

in

THE COLLEGE OF GRADUATE STUDIES

(Civil Engineering)

THE UNIVERSITY OF BRITISH COLUMBIA

(Okanagan)

June 2013

Abstract

Initiation and propagation of a crack in composite materials can affect their global mechanical properties severely. From a numerical modeling perspective, most conventional macro-level methods reported for composite laminates are based on the assumption that a Representative Volume Element (RVE) of the material is periodically repeated over the entire sample. However, a considerable amount of spatial non-uniformity in material and geometrical parameters can exist in both unidirectional (UD) and woven fabric composites. The scattered distribution of fibers, fibers penetration between composite layers, voids within the matrix, human errors during sample preparation, and imperfect thickness distribution can be among the most common sources of such non-uniformity. In turn, these non-uniformities can make the numerical simulation of composites under the assumption of a periodic RVE unreliable, and thereby, the stochastic modeling of effective material properties becomes essential for a more precise assessment of composites' mechanical behaviour.

In the present work, a new three-dimensional (3D) stochastic extended finite element method (XFEM) is proposed and implemented to model the delamination surface in composite samples by integrating the capabilities of the finite element method (FEM) commercial software (ABAQUS) into a user-defined FORTRAN code and MATLAB package. XFEM is known to offer significant advantages over conventional FEM by enabling optimal convergence rates in the presence of pronounced discontinuities/singularities such as cracks. The effect of nonlinear modeling parameters such as cohesive zone length, penalty stiffness factor and large deformation are also considered in the proposed approach to add to the accuracy of simulations. The XFEM model is first tested and validated against previously reported data in the literature. Next, a statistical distribution is sought from data non-

repeatability during a set of double cantilever beam (DCB) and end-notched flexure (ENF) tests conducted on Poly (phenylene Sulfide) PPS/Glass thermoplastic composite samples. Results from the experiments and XFEM are compared and demonstrate the capability of the new numerical approach in capturing non-repeatable material response, often seen during the fracture testing of UD composites to characterize their mode I and mode II fracture properties.

Table of Contents

List of Tables

List of Figures

List of Symbols

A_{large}	Critical energy release rate large displacement correction factor
a_0	Initial delamination/crack length
a_{cr}	Crack/delamination length in the current configuration
Δa_{cr}	Crack/delamination increment
a_{ij}	Material compliance matrix components
B and B_{ij}	Cartesian derivatives of shape functions matrix and components
$\overline{B}$	Transformed Cartesian matrix of derivatives
$\overline{B}_{Coh}$	Cohesive/contact matrix of shape functions
b^H	Crack surface (Heaviside) enriched degree of freedom
C and C_{ijkl}	Material stiffness matrix and its components
C_{ij}	Plane strain/stress material stiffness matrix components
c^{tip}	Crack-tip enriched degrees of freedom
c_{ij}	Imaginary constants of anisotropic material
D_{mg}	Damage index
$\overline{D}_{Interface}$	Matrix of interface material properties
D_S^{ep}	Elastic-plastic constitutive matrix
D_{ij}	Imaginary compliance components of anisotropic material
d_i	Arm of loading on the test sample
E_{Green}	Green strain tensor

E_i	Elastic moduli in different directions
E_L	Linear part of Green strain tensor
$E_{longitudinal}$	Longitudinal Young's modulus of anisotropic material
E_{NL}	Non-linear part of Green strain tensor
$E_{transverse}$	Transverse Young's modulus of anisotropic material
$e_{\mathbf{n}}$	Unit normal vector of the crack alignment
e_s	Unit tangential vector of the crack alignment
e_z	Unit binormal vector of the crack alignment
F	Resisting force against the deformation of numerical model
F	Deformation gradient in the reference coordinate system
F^{enr}	Crack-tip enrichment functions
F_i	Second order strength tensors
F_{ij}	Fourth order strength tensors
$f_1(X,Y,Z)$	Arbitrary continuous function
$f_1^{'}(X,Y,Z)$	Arbitrary discontinuous function
f^b	Vector of body forces
f^t	Vector of external forces
G	Total energy release rate
G_I , G_{II} and G_{III}	Fracture energy toughness for different fracture modes I, II and III
G_{IC}	Mode I critical fracture energy toughness

G_{IIC}	Mode II critical fracture energy toughness
G_C	Total/general critical fracture energy release rate
$G_{C(ave)}$	Mean critical fracture energy release rate
$G_{C(std)}$	Standard deviation of critical fracture energy release rate
G_{CH}	Highest critical fracture energy release rate
G_{CL}	Lowest critical fracture energy release rate
G_S	Matrix of shape function derivatives
G_{ij}	Shear moduli in different directions
$g_i(\theta)$	Component of anisotropic crack-tip enrichment functions
F_{ext}	External load acting on a body
F_{int}	Internal force of a body
$H(\mathbf{x})$	Heaviside step function at point x
$I_{3\times3}$	Identity matrix
J	*J*-integral
$J_{Auxiliary}$	Auxiliary *J*-integral
$J_{Superimposed}$	Superimposed *J*-integral
K_0	Initial stiffness matrix
K_I, K_{II} and K_{III}	Stress intensity factors
K_{Coh}	Cohesive/contact portion of tangential stiffness matrix
K_{Geo}	Geometrical portion of tangential stiffness matrix

K_{Mat}	Material portion of tangential stiffness matrix
K_T	Tangential stiffness matrix
K_{Pen} and $\overline{K}_{ii}$	Penalty stiffness variable and its matrix form for three dimensional problems
K_{ij}	Stiffness matrix components for linear finite element method
K_I^{aux}, K_{II}^{aux} and K_{III}^{aux}	Auxiliary stress intensity factors
K_{node}^1 and K_{node}^2	Sets of nodes associated with crack-tip regions
L	Test sample length
$L(c)$ and $L_{ij}(c)$	Orthotropic material fracture properties constant
l_{ch}	Cohesive zone length
l_e	Finite element mesh size and element length
M and M_i	Interaction integral
M_{Local}	Local interaction integral
M_S	Re-arranged second Piola-Kirchhoff stress tensor
m_{Line}	Slope of ordinary least square technique line
m_{poly}	Number of sub-polygons in an element for numerical integration
m_{ij}	Direction cosines
$N(x)$	Conventional finite element method shape function
N^{all}	Finite element mesh nodes
N^{enr}	Normalized enriched shape function

N^f	Enriched nodes of the finite element mesh
N^g_{node}	Set of nodes corresponding to the crack face
n_i	Vector of outward normal direction
n_G	Gauss quadrature order
(n_1^t, n_2^t, n_3^t)	Unit vector of the crack edge
P and P_{ij}	Nominal stress tensor and its components
$P_{Contact}$	Vector of contact forces
P_{grip}	Loading on a the test sample (from the tensile machine crosshead)
p_i	Anisotropic material compliance constant depending on longitudinal material properties
q'	Smoothing function of contour integral
q_i	Anisotropic material compliance constant depending on transverse material properties
R_0	Right hand side vector of external forces
R_{COD}	Ratio of opening to sliding displacements
R_{SIF}	Ratio of dynamic stress intensity factors
$Rs(u^h)$	Residual forces
$Rand_i$	Randomly chosen number from a Weilbull distribution
(r, θ)	Local polar coordinate system at the crack-tip
S	Material compliance matrix

S_{ij}	Shear strengths in different material directions
T	Traction of interfacial material
$T_{\max}$	Maximum interfacial strength
T_{ij}	Interlaminar material strength in different directions
t_{Block}	Loading block thickness
t_{ck}	Test sample thickness
t_i	Surface traction vector
u^{enr}	Enriched degree of freedom
u^k	Displacement field of the integration domain
du^k	Displacement increment
u^h	General vector containing all the nodal parameters
u^{ord}	Ordinary degrees of freedom
$u^g(x)$	Displacement field at point x
u_i	Displacement field in different directions
$u_k^{Auxilairy}$	Auxiliary displacement field in different directions
u_x^{tip}, u_y^{tip} and u_z^{tip}	Displacement fields near the crack-tip in different directions
V_e	Element volume
V^*	Ratio of each sub-polygon volume to element volume
v_{ij}	Poisson's ratios in different directions
W	Strain energy density

W^{aux}	Auxiliary strain energy density
w	Test sample width
w^g	Gauss points weights
w^p	Modification factor for the weight of each sub-polygon
X_C	Compressive strength in fibers direction
X_i	Reference (Lagrangian) coordinates
X_T	Tensile strength in fibers' direction
X^*	Point on the crack surface
X'	Arbitrary point in finite element mesh
(X, Y, Z)	Reference coordinates
(X_1, Y_1, Z_1)	Arbitrary point 1 coordinates on the crack surface
(X_2, Y_2, Z_2)	Arbitrary point 2 coordinate on the crack edge
(X_1^*, Y_1^*, Z_1^*)	Nodal coordinates in the reference configuration
(x, y, z)	Current coordinates
Y_C	Compressive strength in perpendicular direction to fibers
Y_T	Tensile strength in perpendicular direction to fibers
YS_{normal}	Normalized failure threshold
Z_C	Compressive strength in perpendicular direction to fibers
Z_T	Tensile strength in perpendicular direction to fibers
α	Penalty stiffness scaling factor

α_1	Weibull distribution shape parameter
β_1	Weibull distribution scale parameter
Γ	Far-field surface path
Γ_c	Crack surface path
Γ_t	Traction surfaces
Γ_V	Body domain
Δ	Opening/Sliding displacement of the grip load
δ	Relative opening/sliding displacement
δ_0	Relative critical opening/sliding displacement
δ_{eff}	Effective separation displacement
δ_f	Relative failure opening/sliding displacement
δ_{fH}	Highest relative failure opening/sliding displacement
δ_{fL}	Lowest relative failure opening/sliding displacement
δ_n	Normal crack-tip opening displacement
δ_{n0}	Relative normal crack-tip opening displacement parameter
δ_t	Tangential crack-tip opening displacement
δ_{t0}	Relative tangential crack-tip opening displacement parameter
$\overline{\delta}$	Relative crack displacement in the global coordinate system
ε and ε_{kl}	Green strain tensor and its components

$\varepsilon_{ij}^{Auxilairy}$	Auxiliary strain tensor components
$\varepsilon_{f,ult}$	Fiber failure strain
$\varepsilon_{m,ult}$	Matrix failure strain
ε'_f	Fiber strain at matrix failure
ε'_m	Matrix strain at fiber failure
θ_0	Crack-tip angle
θ_i	Transformed angles in anisotropic material
μ_i, $\overline{\mu}_i$, μ_{xi} and μ_{yi}	Anisotropic material properties derived from material governing equation
ξ^*	Correction factor of relative crack displacements ratio
(ξ_1, ξ_2, ξ_3)	Local coordinates of finite element method
$\overline{\Pi}(u^k)$	Virtual work
σ and σ_{ij}	Second Piola Kirchhoff stress tensor and its components
σ_i	Re-arranged second Piola Kirchhoff stress tensor
σ_{eff}	Effective traction
$\sigma_{f,ult}$	Fiber failure stress
$\sigma_{m,ult}$	Matrix failure stress
σ'	Cauchy stress tensor
σ'_f	Fiber stress at matrix failure mode
σ'_m	Matrix stress at fiber failure mode

$\sigma_{ij}^{Auxilairy}$	Auxiliary stress tensor
$\phi(x)$	Conventional shape function
$\varphi(\delta_n, \delta_t)$	Traction-separation model potential function
φ_0	Material fracture energy
φ_1	Element nodal distance value from the crack face
Ψ , Ω	Orthotropic material parameters relating the stress intensity factors to crack opening/sliding
$\psi(x)$	General enrichment function
ψ_1	Element nodal distance from the edges of the crack plane
Ω_e	Element domain

Acknowledgements

I wish to thank Dr. Abbas S. Milani for his great supervision, mentorship, inspiration, help and constant encouragement during my PhD research and studies at the University of British Columbia. I would also like to acknowledge the valuable assistance of Drs. Martin Bureau, Francis Thibault, David Butcher, Hicham Mir, and Zohir Benrabah from the National Research Council of Canada – Industrial Materials Institute (NRC-IMI) for training and providing access to their lab facilities. Finally, financial support from the Natural Sciences and Engineering Research Council (NSERC) of Canada is greatly acknowledged.

Dedication

To my parents and family for their unconditional love and support.

1 Chapter: Introduction

Composites are generally defined as multiphase materials made by commingling two or more existing materials to achieve required mechanical, thermal or electrical properties. Fiber reinforced polymer (FRP) can be categorized as a composite material that is composed of a base polymer material called matrix and reinforced by rebars called fibers. A complete bonding between these two material phases can provide sufficient functionality toward application of composites. The effective mechanical properties of FRP composites are of great interest to aerospace and structural engineers and are directly related to the properties of individual components of each given FRP as reviewed below.

1.1 Fibers

Fibers are materials made into long filaments with 10μm diameter. The main duties of fibers in composites consist of carrying the external loads and providing the required stiffness, strength and thermal stability. Fibers should demonstrate the following characteristics to satisfy the desirable mechanical properties of FRP composites [1]:

1- High modulus of elasticity.

2- High ultimate strength.

3- Low variation of strength among their distributions.

4- High stability of their strength during handling.

5- High uniformity of diameter and surface dimension among bundles of fibers.

In the present industrial applications, there are mainly three dominating types of fibers: carbon, glass and aramid fibers. Carbon fibers have high elastic modulus and fatigue failure strength in comparison to the other two types of fibers; however, the economic aspects of their application should always be considered [2]. Glass fibers have demonstrated good mechanical strength relative to their low cost, which has increased their application as reinforcing agent in FRP composites in cost-sensitive industries such as construction [1]. In Table 1-1, a summary of mechanical properties of commonly used fibers is presented.

Table 1-1 Mechanical properties of fibers in commonly used FRPs [3]

Material	**Density** (kg/m^3)	**Longitudinal Modulus of Elasticity** (MPa)	**Longitudinal Strength** (MPa)	**Relative cost**
E-glass	2540	70000	3450	Low
S-glass	2500	86000	4500	Moderate
Graphite, high modulus	1900	400000	1800	High
Graphite, high strength	1700	240000	2600	High
Kevlar 29	1450	80000	2800	Moderate
Kevlar 49	1450	130000	2800	Moderate

1.2 Matrix

The matrix is the base material of a FRP composite which confines and bonds the fibers together. It is mainly composed of plastic ingredients that are less environmentally hazardous

and more corrosion resistant in comparison to fibers. The followings are the main duties and features of matrix materials in FRP composites [1]:

1- Transferring the external loads to the fibers while binding them together.

2- Protecting the fibers from environmental hazards and corrosion.

3- Providing the general shape of a given FRP structure.

4- Defining some effective mechanical properties of the composite (mainly perpendicular to the fiber directions) such as ductility, impact strength, etc.

In industrial applications, FRP composite materials are often manufactured with two types of matrices: thermosets and thermoplastics. Thermosets provide higher strength in comparison to thermoplastics; however, once cured, they cannot be reheated and reused or reformed. This is in contrast to thermoplastic matrices which can be re-employed for recycling through melting and solidification cycles. In Table 1-2, mechanical properties of common matrix materials are presented.

Table 1-2 Mechanical properties of matrices in commonly used FRP composites [3]

Material	Density (kg/m^3)	Tensile Modulus (MPa)	Tensile Strength (MPa)
Epoxy	1200-1400	2500-5000	50-110
Phenolic	1200-1400	2700-4100	35-60
Polyester	1100-1400	1600-4100	35-95
Nylon	1100	1300-3500	55-90
PEEK	1300-1350	3500-4400	100
PPS	1300-1400	3400	80
Polycarbonate	1200	2100-3500	55-70
Polyethylene	900-1000	700-1400	20-35
Teflon	2100-2300	-	10-35

1.3 Classification of FRP Composite

Numerous methods for classification of FRP composites exist in the literature. For instance, the classification can be based on the different matrices: thermosets and thermoplastics. Another approach for classifying the FRP composites is based on fiber material type: carbon, glass or aramid. Fiber length can also be applied to differentiate the FRP composites: short-fiber and long-fiber composites. Short-fiber reinforced composites consist of a dispersed phase of discontinuous fibers (fiber length is less than hundred times diameter) with random or preferred orientation of fibers. On the other hand, long-fiber reinforced composites contain continuous fibers bonded together by the matrix. They can be composed of a unidirectional

orientation of fibers or a bidirectional orientation of fibers (e.g., woven composites), or 3D textile preforms.

1.4 FRP Composite Materials Applications

Today fiber Reinforced Polymer (FRP) composite materials are widely used in high tech engineering applications including aeronautical, marine and automotive industries. These materials have high strength-to-weight ratios, good corrosion resistance, superior fracture toughness, and can be engineered based on required strength or performance objectives for a given structure. To give few examples, leading aircraft manufacturers such as Airbus and Boeing have increased the application of FRP composites in their products from 3% to 20% in Airbus A380 and over 50% in Boeing 787 [4]. Figure 1-1 depicts one of the largest aircraft wings, with a 42.4 meter span, made of carbon FRP composite assembled for the Airbus Military A400M transport aircraft. In construction industry, FRP composites have become a good alternative for innovative construction and their applications have already been extended to upgrading and retrofitting the existing structures as well as constructing various types of off-shore platforms, buildings and bridges. Pontresina Bridge (Figure 1-1-d), with a span length of 12.5 m, was constructed in 1997 across the Flanz River in Switzerland. The structural truss system of the bridge was made of FRP composite [5].

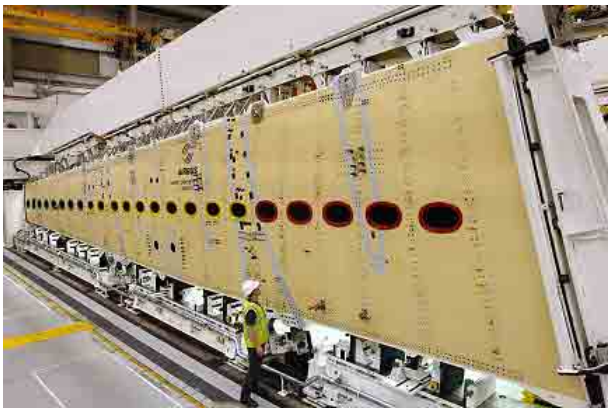

(a)

(b)

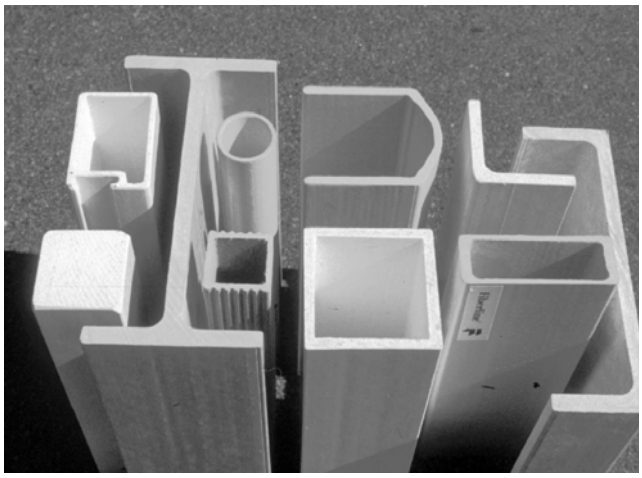

(c)

(d)

Figure 1-1 Sample applications of FRP composite materials in different industries: (a) & (b) Airbus Military A400M aircraft CFRP wing (Martin Chainey / Airbus Military)**, (c) Cross-sections of glass fiber reinforced polymer (GFRP) structural members used, and (d) Pontresina Bridge made of FRP** [5]

1.5 FRP Composite Materials Weaknesses and Application Limitations

Although FRP composite structures have proven to provide numerous advantages, initiation and propagation of cracks in these materials can affect their mechanical properties drastically. The most common FRP composite material failure modes are classified into fiber breakage, fiber-pull out, matrix cracking and interlaminar delamination (Figure 1-2). Fiber breakage

failure in FRP composites depends on the fibers strength distribution. This failure mode occurs when the subjected tensile stress in the FRP increases and leads to failure of low strength fibers in the laminate while the high strength fibers are still carrying the external load. For a better understanding of fiber breakage, distribution of the fibers strength in FRP has been investigated by several researchers and it was realized that the strength of glass fibers follows the Rayleigh distribution [6] while the strength of carbon fibers fits the Weibull and Gauss distributions [7]. In the cases where fiber strength is greater than the interface bond between the matrix and the fibers, the fibers can be pulled out of the matrix due to the tensile loading. In several cases, the fiber pull-out occurs at the fibers end, or at a fracture surface in the laminate. Another common failure mode in FRP composites attributed to the matrix material is called the matrix cracking. Since strength in the matrix is commonly lower than the fibers, normally the first stage of failure starts with matrix deterioration. Matrix cracking usually takes place before the entire FRP laminate matches its failure point, and it demonstrates a ductile failure in comparison to the brittle fiber failures. Among other failure modes, delamination is perhaps the most common failure mode and may occur because of a weak bonding between composite layers, existing cracks in the matrix material, broken fibers and fatigue or impact loadings. It can drastically reduce the structural stiffness and weaken the tensile or shear capacity of the FRP structures under service loads [8].

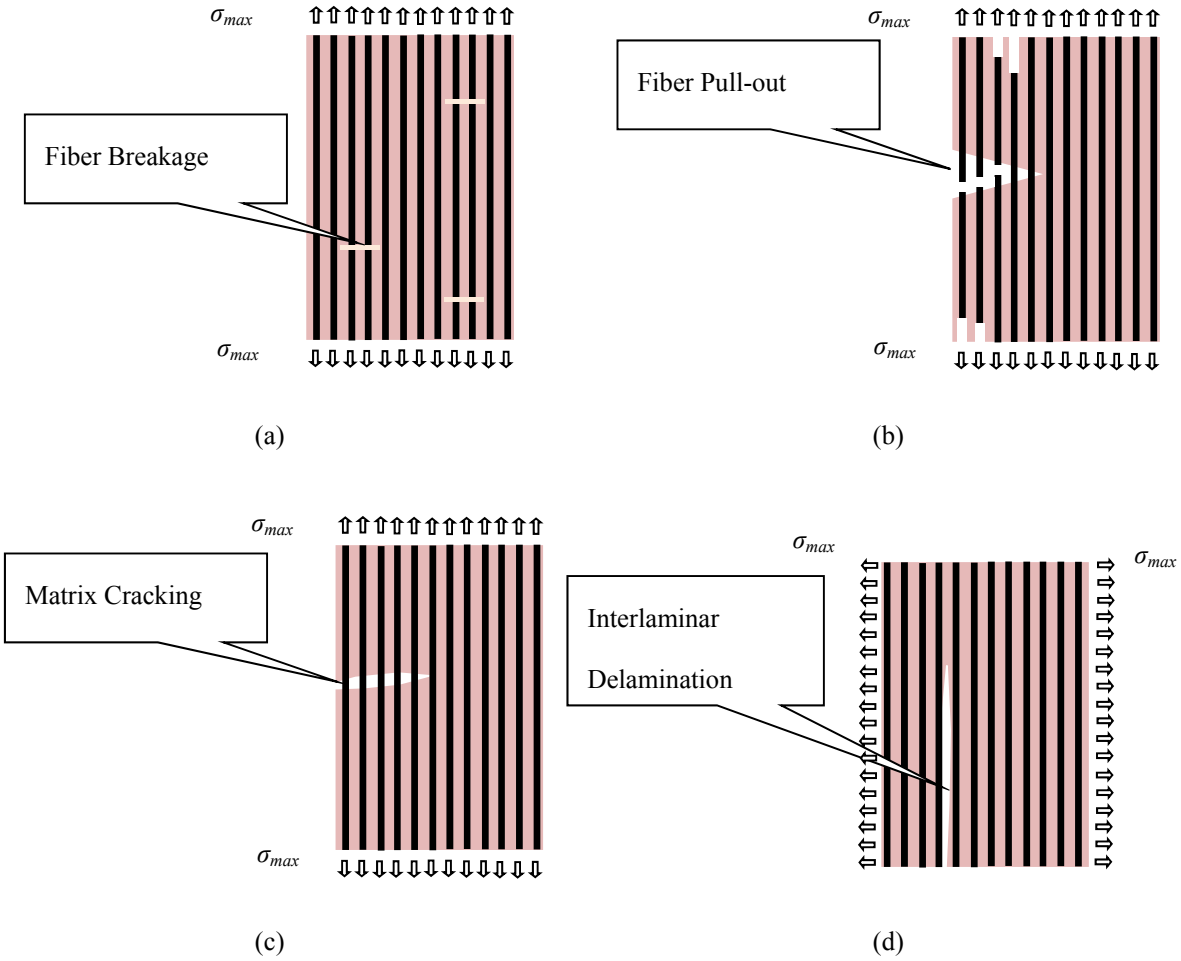

Figure 1-2 FRP composite materials common failure modes: (a) Fiber breakage, (b) Fiber pull-out, (c) Matrix cracking, and (d) Interlaminar delamination

Mechanical defects are not the only cumbersome issue affecting the FRP performance and applications. Another undesirable feature of FRP composite materials is the complex heterogeneous and often stochastic properties of these materials which result in randomness and uncertainty in their manufacturing processes and material compositions in final products. The deterministic approaches used in many investigations ignored the spatial variability that exists in such material behaviour, especially at the micro-level scale, and this effect can entail errors into larger scale simulations. Traditionally, a common modeling approach for FRP's is

the implementation of a homogenization technique [9] and relating a certain scale of material properties to the larger scale, mostly by averaging measured properties (Figure 1-3). Homogenization techniques can be categorized into micro-level, meso-level and macro-level, where the uncertainty and variability are assumed for different scales of material composition. At the micro scale, microstructure of the material composition is examined with methods such as the moving-window technique (MWT) [10]. This approach requires sophisticated experimental instruments and deals with the complexity of the FRP composite material conformation and may not be suitable for non-research purposes. Meanwhile, at the meso-level, study of FRP composites has received considerable attention over the past decades and proven to be one of the effective ways to harness uncertainty to homogenization processes [11, 12]. However, difficulties with boundary condition assumptions in modeling still exist in this technique and have made its application for large structures challenging [13]. The largest scale in material composition studies is the macro-scale. Such studies avoid the microscopic complexity of composite materials and the numerous random variables. In macro-level techniques, an existing material's behaviour and randomness are captured by coupon size test results while relying on continuum-mechanics based structural modeling formulations [14].

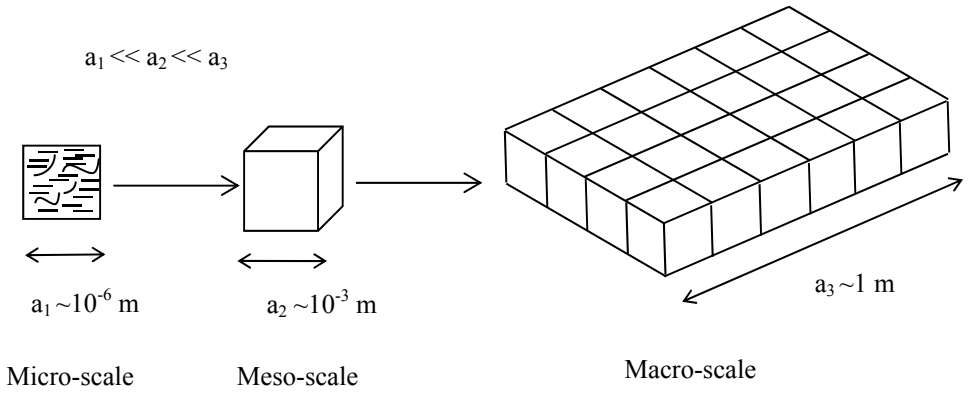

Figure 1-3 Different scales of material modeling during homogenization of material properties

1.6 Experimental and Numerical Modeling of FRP Fracture Properties

In order to improve mechanical performance of FRP composite materials in the presence of process-induced or loading-induced cracks, extensive studies on the fracture properties of FRP composites have been performed, both experimentally and numerically. Experimentally, Owen and Bishop [15] applied the double edge-notched tensile test to measure the mode I critical stress intensity factor for varying orientations of UD glass FRP composites (Figure 1-4). Gaggar and Broutman [16] utilized both single and double edge-notched tensile tests as well as a notched bend test to extract the critical stress intensity factors. Mower and Li [17] summarized the experimental results from previous investigations and concluded that the linear elastic fracture mechanics (LEFM) is not a valid approach for FRP composite materials with long fibers and a nonlinear material constitutive model is required to accurately characterize the fracture energy toughness of FRP composites. The fracture energy toughness of unidirectional FRP composite materials under a double cantilever beam (DCB) test can be calculated using the modified beam theory, compliance calibration and modified compliance calibration methods [18]. The modified beam theory approach is recommended by O'Brien

and Martin [19] and has shown the most repeated value for the critical fracture energy toughness. In order to measure the mode II fracture energy toughness of the FRP composites, the end-notched flexure (ENF) test was suggested and employed by Davies et al. [20]. The ENF test is today one of the most recognized testing methods for mode II study of FRP composite materials. However, due to the unstable nature of this test, only the crack initiation values can be extracted from the test results. Edge delamination phenomena is another failure mode in FRP composite laminates studied by Lee [21] using the edge crack torsion (ECT) test. This test can be applied to extract the mode III interlaminar fracture properties of specimens. The extensive investigation on the fracture phenomenon of test samples showed delamination problems mainly consist of mixed mode fracture mechanics characteristics. Subsequently, the mixed mode bending (MMB) test has been designed as one of the recent methods for mixed mode characterization (mode I and II interaction).

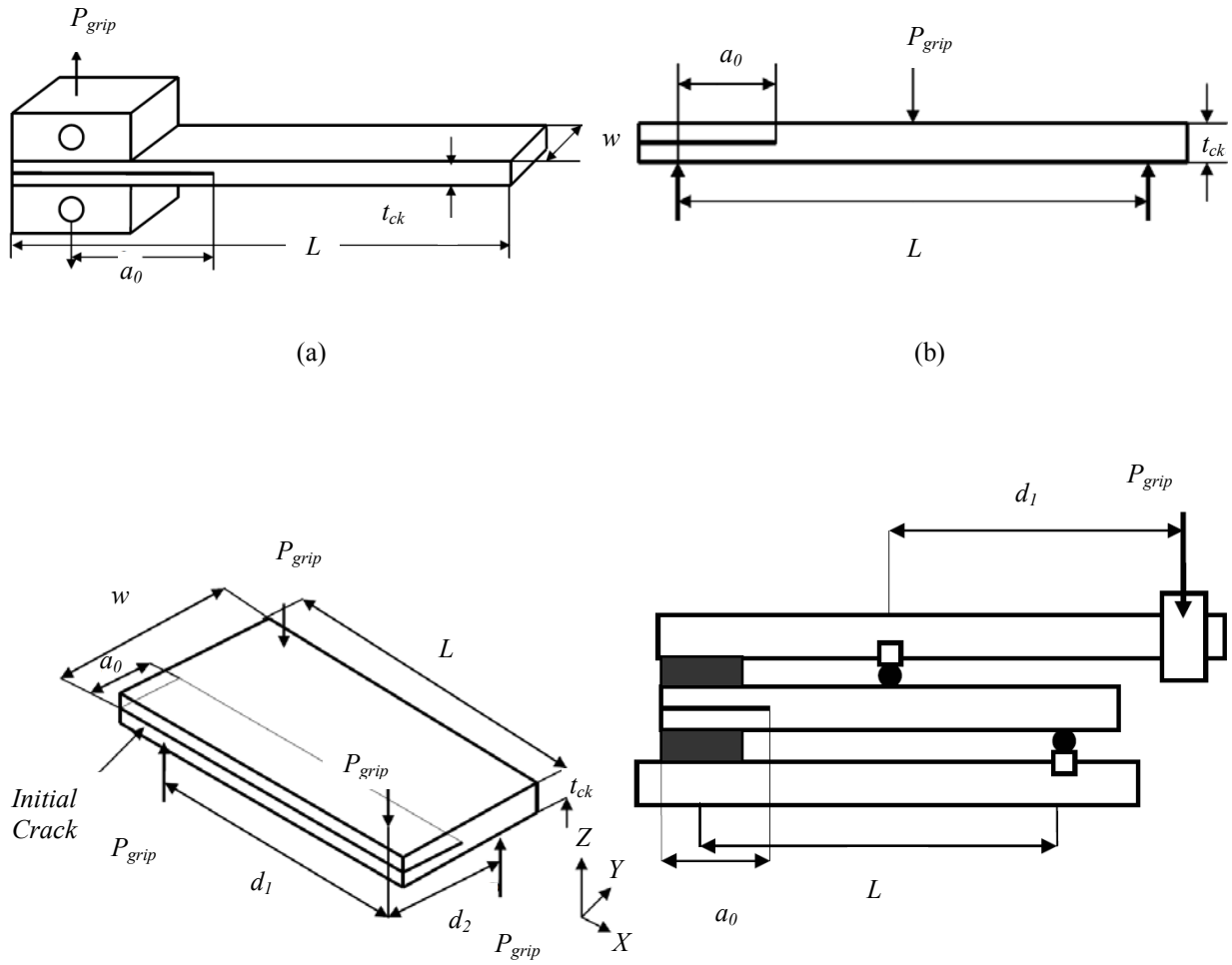

Figure 1-4 Fracture energy toughness measurement fixtures: (a) Double Cantilever Beam, (b) End-Notched Flexure, (c) Edge Crack Torsion, and (d) Mixed Mode Bending tests [8]

Regarding numerical modeling of FRP composites delamination, numerous investigations have been performed over the past few decades. Hillerborg et al. [22] introduced a combination of finite element method and an analytical solution to simulate the crack growth in concrete structures. This approach is often referred to as 'fictitious crack modeling', where a traction-separation law instead of the conventional stress-strain relationship is utilized in the

crack-tip zone to capture the degradation of the material properties due to damage. Later, Xu and Needleman [23] applied an energy potential function to implement the cohesive zone model (CZM) during the analysis of interface debonding. CZM application was extended to FRP composites by Camacho and Ortiz [24], Camanho et al. [25], Blackman et al. [26], Gao and Bower [27], Segurado and LLorca [28], Cox and Yang [29] and Nishikawa et al. [30] while they have improved the cohesive interface models. Based on these reports, CZM has proven to be capable of modeling the 'large process zones'—in the present case the FRP composite delamination. Despite its capability to model the progressive delamination, some severe disadvantages of applying large process zone have been noted and need to be tackled. These include numerical instability (elastic snap-back), reduction of stress intensity upon delamination initiation, and the fictitious softening of the original body in the process zone. In other investigations, a newly introduced feature of the finite element method, known as the extended finite element method (XFEM), has been more recently implemented for numerical modeling of progressive delamination in FRP composites. The original XFEM approach was first introduced by Belytschko and Black [31] and enhanced by Moës et al. [32]. They implemented the concept of a partition of unity method (PUM), introduced earlier by Melenk and Babuška [33], to develop a method to model material discontinuity. In the basic XFEM approach, a Heaviside step function is implemented to model the crack surface by adding extra degrees of freedom to each node of the so called 'enriched elements' [32]. They introduced a framework capable of considering cracks and frictional contact with the zero-thickness process zone in 2D problems. Xiao et al. [34] utilized this approach combined with a statically admissible stress recovery (SAR) technique in modeling cohesive cracks with a softening law composed of linear segments. Later, the approach was implemented by Unger

et al. [35] to model the cohesive crack in concrete specimens. The application of the 2D model was extended to composite materials by Benvenuti [36], who regularized XFEM for embedded cohesive interfaces. Sosa et al. [37] demonstrated the effectiveness of XFEM in 3D modeling of fiber metal laminate delaminations and compared their results with existing CZM results. XFEM and CZM concepts will be discussed in more detail in Chapters 4 and 5.

1.7 Randomness in FRP Fracture Properties

As addressed in Section 1.5, studying composite materials based on the assumption of Representative Volume Element (RVE) and the subsequent homogenization have been the basis of the work of several researchers. Kaw [38] used the RVE approach for unidirectional (UD) composites and Peng and Cao [39] developed a dual homogenization technique for woven fabrics. However, other investigations have shown that there can be considerable spatial non-uniformity both in UD composites [40] and woven fabrics [41, 42], which may hinder the full capability of RVE approach for fracture simulations [43]. There can be a variety of sources for such non-uniformity of material properties in composites. Examples include random distributions of fibers within samples, fiber penetration between layers, existence of voids within the matrix, human error in manufacturing process, uneven heating or cooling of samples during molding. Hence, there is a need for developing new models that can consider the heterogeneousness characteristics of FRP composites and include statistical distributions of their mechanical properties as well as the pre-existing defects in test specimens [44, 45]. Stochastic modeling of the mechanical behaviour of composites can be especially important in predicting critical loads and critical displacement values, as well as crack formation patterns in large structures [46, 47]. Among the most recent works on

stochastic modeling of FRP composites, Ashcroft et al. [48] emphasized the effect of material uncertainty and non-uniformity in predicting delamination phenomena.

1.8 Motivation and Objectives of the Work

Based on the above background review, a number of investigations have been performed to study the mechanical properties of FRP composites. In particular, fracture behaviour of these materials is an interesting topic where a variety of experimental tests and numerical procedures have been proposed by different research groups. The heterogeneous nature of FRP fracture properties has made the research in this area a challenging task. With respect to numerical simulations, different numerical methods have been applied to extract the correct behaviour of FRP composites and the results demonstrated the necessity for further investigation in this field for more realistic simulations. Among the various numerical methods employed to model the delamination in composite materials, the interface element method combined with a cohesive law has received great attention by numerous researchers to date. Espinosa et al. [49] implemented this method for modeling dynamic delamination of woven GFPR composite materials with an anisotropic visco-plastic material model in conjunction with a cohesive law. Cohesive zone model properties such as maximum interface strength, fracture parameters, penalty stiffness and cohesive zone length were studied by Turon et al. [50] and Harper and Hallett [51] to overcome the existing implementation obstacles of cohesive zone models in numerical simulations. A generalized framework for implementing the cohesive XFEM in modeling delamination was introduced by Benvenuti [36]. In that work, the fundamentals of XFEM with cohesive law characteristics were studied and examples of DCB test were modeled. In addition to FEM-based methods, a mesh-free

based method was utilized by Barbieri and Meo [52] to extensively simulate the mode I and II, DCB, ENF and end-loaded split (ELN), tests in 2D with the focus on nonlinear aspects of crack problems. Most of the above mentioned studies, however, are based on deterministic properties of composite materials, especially their fracture properties, while other experimental results demonstrated the variability of the composite fracture phenomenon [48]. Among recent stochastic works, Ashcroft et al. [48] introduced micro-structure randomness in the form of fracture properties of CFRP composite materials into the numerical simulation of DCB tests using interface cohesive elements in the FEM model. Non-uniformity and random distribution of material fracture properties were considered by means of uniform and Weibull distributions and results emphasized the need for further studies on including micro structural randomness for accurate predictions of fracture performance of composite laminates.

Therefore, the present thesis is primarily aimed at developing and examining an enhanced numerical approach for simulating the composite fracture tests considering both material and geometric nonlinearities along with stochastic fracture properties. A simplified approach is introduced to implement the cohesive zone model and hence to avoid the numerical softening due to existence of a large process zone. An ABAQUS user-element subroutine is developed and linked to MATLAB to implement the nonlinear XFEM for DCB test simulation (mode I fracture). The cohesive zone model is associated with enriched elements to consider a bilinear traction-separation law in the crack front using the XFEM contact model following the work of Khoei et al. [53]. The model is also implemented to investigate the ENF test for mode II fracture properties. Stochastic distributions are employed to the fracture properties of the material via the bilinear traction-separation law, and results are compared with both available data in the literature and a set of performed tests on Poly Phenylene Sulfide (PPS)/Glass UD

composites. Finally, a set of sensitivity analyses are performed to identify the effects of different model variables such as the mesh size, cohesive zone length and penalty stiffness.

1.8.1 Potential for Practical Applications and Expected Originality

As addressed before, composite materials are rapidly replacing metallic materials in different industries. Moulding process is an essential part of any composite manufacturing line that deals with forming structural components for vehicles, airplanes, boats, etc. A rising challenge for optimal implementation of FRP composites in forming processes, however, is to understand their behaviour and conformability against heat and pressure variations as well as different geometries of the mould. For instance, during moulding process of a thick FRP composite into a curved/bent part, it is possible that in the corner of the part, delamination between layers initiates and propagates and eventually be a reason for the rejection of the part (Figure 1-5) [54]. The same problem may happen during service under excessive loadings, even for a part that had been originally manufactured with no flaw. Therefore, it is required for leading industries to employ advanced simulation tools as part of their design and manufacturing processes to predict damage phenomena (in the present case, delamination) in FRP composite materials as accurately as possible, while not ignoring the unavoidable variation in material properties of composites (in the current case, the fracture properties).

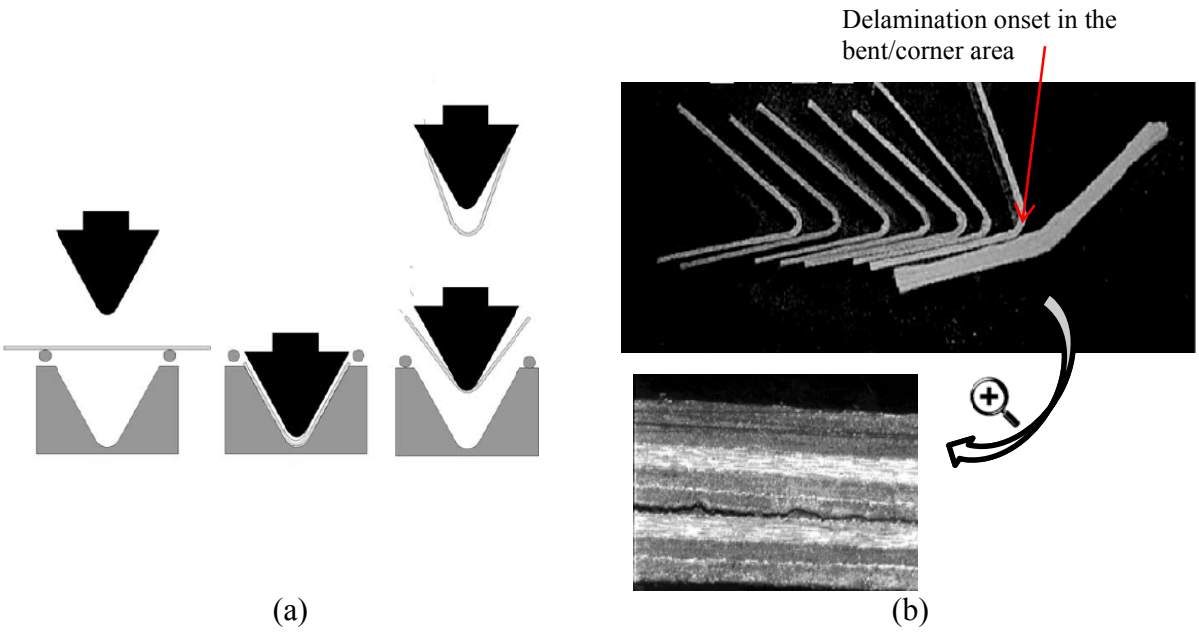

Figure 1-5 Forming process of a heated FRP composite laminate: (a) Initiation of the forming (Step 1), compression and cooling cycle (Step 2), removing the male die and possible dimensional distortion of the part (Step 3); and (b) Delamination spotted in the corner of a compression moulded component [54]

The expected originality of the present work within the context of application of advanced numerical modeling approaches for composite design and manufacturing can be summarized as follows.

- Performing mode I and II fracture tests for a PPS/Glass UD laminate used in aerospace and automotive industries.
- For the first time investigating the observed randomness (non-repeatability) in the material response from the above fracture tests.
- Enhancing the existing XFEM approach in the literature to model the composite fracture tests under uncertainty (combining XFEM with contact and cohesive

modeling capabilities under one framework, along with stochastic fracture properties), hence moving towards more reliable damage prediction tools.

- Implementing stochastic characteristics of the tested PPS/Glass UD composites in the XFM simulations and validating with experimental data.
- Studying the effect of different modeling factors (such as penalty stiffness) in the enhanced XFEM approach using a series of sensitivity analysis.

1.9 Thesis Outline

This thesis is organized into five chapters. The first chapter, presented above, focused on a general literature review on experimental and numerical modeling of the fracture mechanics of FRP composite materials and also the necessity for considering the variability in micro-structure of these materials. In Chapter 2, damage modeling and fracture properties of FRP composites are reviewed. Also in this chapter, the XFEM method and its applications are reviewed and discussed. In the final part of Chapter 2, cohesive zone and contact surface implementations of XFEM are described and finite element formulations are presented. In Chapter 3, results from XFEM simulations are compared to those extracted from other numerical methods and benchmark experimental tests in the literature. Modeling parameters such as penalty stiffness, mesh size and cohesive zone length are studied via a set of sensitivity analysis to examine the presented XFEM approach effectiveness in modeling fracture properties of UD composites. Chapter 4 presents the fabrication process and experimental procedures used to obtain elastic moduli and fracture properties of PPS/Glass samples. Following, stochastic features of the measured fracture properties are introduced to the XFEM model. Results are then compared with those from experiments using DCB and

ENF test set-ups. Finally, in Chapter 5, the undertaken numerical and experimental procedures as well as the main results are summarized. Future work recommendations are also included in Chapter 5.

2 Chapter: Background

In this chapter, elastic mechanical behaviour, damage properties and fracture mechanics of FRP composite materials along with different underlying modes of failure are first reviewed. Advantages of damage modeling and fracture mechanics will be compared in modeling the post-failure behaviour of FRP composite materials. Next, basic definition and properties of XFEM will be described and its application in modeling the LEFM and EPFM will be discussed. The implementation of damage mechanics through cohesive zone model (CZM) will also be presented and effective parameters in such a model will be summarized.

2.1 Elastic Mechanical Behaviour of FRP composite Materials

As mentioned in Chapter 1, in FRP the matrix provides the integrity of the composite by holding fibers together. It also has greater elongation characteristic than fibers which forces the fibers to carry the maximum load before the matrix fails. Fibers, on the other hand, provide high strength and stiffness to the material system. Such a material composition will lead to anisotropic material properties and entails an appropriate technique for extracting the global (macro-level) material behaviour. The conventional elastic constitutive relationship between stress σ_{ij} and strain ε_{kl} for a FRP composite material, similar to an orthotropic material, can be written as:

$$\begin{Bmatrix} \sigma_{11} \\ \sigma_{22} \\ \sigma_{33} \\ \sigma_{12} \\ \sigma_{13} \\ \sigma_{23} \end{Bmatrix} = \begin{bmatrix} C_{1111} & C_{1122} & C_{1133} & 0 & 0 & 0 \\ C_{1122} & C_{2222} & C_{2233} & 0 & 0 & 0 \\ C_{1133} & C_{2233} & C_{3333} & 0 & 0 & 0 \\ 0 & 0 & 0 & C_{1212} & 0 & 0 \\ 0 & 0 & 0 & 0 & C_{1313} & 0 \\ 0 & 0 & 0 & 0 & 0 & C_{1323} \end{bmatrix} \begin{Bmatrix} \varepsilon_{11} \\ \varepsilon_{22} \\ \varepsilon_{33} \\ 2\varepsilon_{12} \\ 2\varepsilon_{13} \\ 2\varepsilon_{23} \end{Bmatrix} \tag{2-1}$$

where C_{ijkl} (i,j,k,l = 1, 2, 3) are the stiffness matrix, **C**, components. For easier demonstration of the material parameters, especially for FEM implementation, the following vector-form compliance equation is used to describe the material constitutive behaviour:

$$\varepsilon = \mathbf{S}\sigma \quad \text{where} \quad \mathbf{S} = \mathbf{C}^{-1} \tag{2-2}$$

where the compliance matrix, **S**, is re-arranged as follows:

$$\mathbf{S} = \begin{bmatrix} \frac{1}{E_1} & -\frac{\nu_{21}}{E_2} & -\frac{\nu_{31}}{E_3} & 0 & 0 & 0 \\ -\frac{\nu_{12}}{E_1} & \frac{1}{E_2} & -\frac{\nu_{32}}{E_3} & 0 & 0 & 0 \\ -\frac{\nu_{13}}{E_1} & -\frac{\nu_{23}}{E_2} & \frac{1}{E_3} & 0 & 0 & 0 \\ 0 & 0 & 0 & \frac{1}{G_{12}} & 0 & 0 \\ 0 & 0 & 0 & 0 & \frac{1}{G_{13}} & 0 \\ 0 & 0 & 0 & 0 & 0 & \frac{1}{G_{23}} \end{bmatrix} \tag{2-3}$$

E_i is the elastic modulus in direction i, G_{ij} are the shear moduli and v_{ij} are the Poisson's ratios. Generally, the unidirectional composite materials have a transversely isotropic behaviour which yields a relationship between material properties as follows:

$$E_1 = E_2 \ , \ \nu_{12} = \nu_{13} \ , \ G_{12} = G_{13} \tag{2-4}$$

Subsequently, the compliance matrix can be redefined as:

$$\mathbf{S} = \begin{bmatrix} \frac{1}{E_1} & -\frac{\nu_{12}}{E_1} & -\frac{\nu_{12}}{E_3} & 0 & 0 & 0 \\ -\frac{\nu_{12}}{E_1} & \frac{1}{E_1} & -\frac{\nu_{32}}{E_3} & 0 & 0 & 0 \\ -\frac{\nu_{12}}{E_1} & -\frac{\nu_{23}}{E_1} & \frac{1}{E_3} & 0 & 0 & 0 \\ 0 & 0 & 0 & \frac{1}{G_{12}} & 0 & 0 \\ 0 & 0 & 0 & 0 & \frac{1}{G_{12}} & 0 \\ 0 & 0 & 0 & 0 & 0 & \frac{1}{G_{32}} \end{bmatrix} \quad (2\text{-}5)$$

The American Society for Testing and Materials (ASTM) standards [55-57] has proposed several experimental tests for extracting the material elastic constants at macro-scale.

2.2 Failure Modes of FRP Components

Most FRP composite materials demonstrate a brittle behaviour when imposed to in-plane loading. Typically, the response curve of such laminated FRP composites under tensile test starts from the origin and increases linearly up to the failure point. At this point, the material faces a form of irreversible damage (e.g., fiber breakage). After this point, it is most likely that the load-deformation curve drops to zero and the FRP composite loses its capacity to carry further load. The stress-strain relationships for several fiber materials are demonstrated in Figure 2-1.

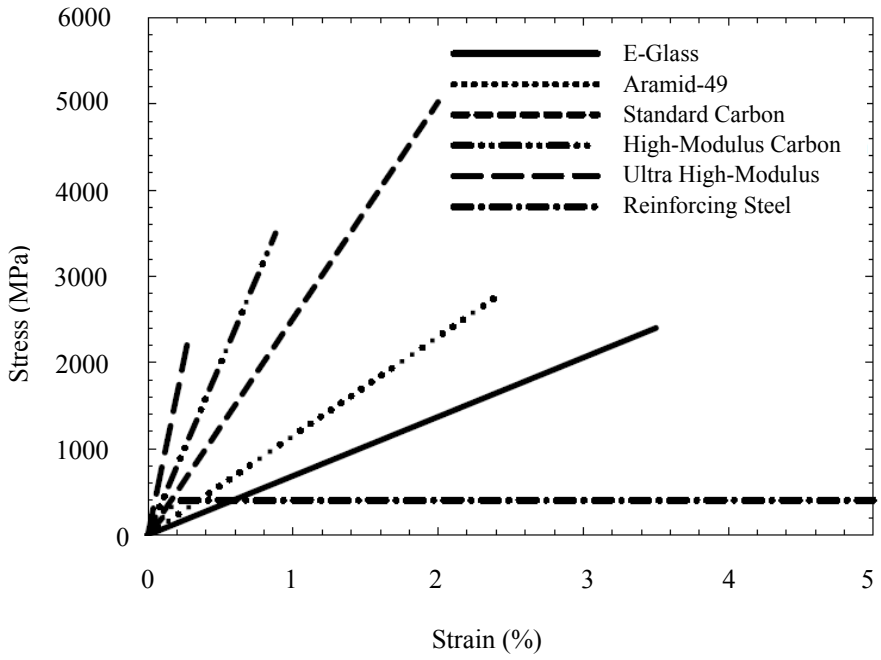

Figure 2-1 Comparison of tensile stress-strain curve of fiber materials [58]

Damage initiation in FRP composite materials has a direct relationship with matrix and the fiber material properties and the existing flaws in the structure. A difference between the elongation limit of the matrix and fibers is a dominant parameter in tensile failure of a laminated FRP composite. In the case where failure strain of fibers is larger than the matrix, the matrix cracking is expected to happen earlier. However, if the fiber ratio of the composite is large enough (greater than about 10%), fibers can continue carrying the load up to their rupture. On the other hand, if the fibers have lower elongation than the matrix, which is the most common case, it will force fibers to carry the maximum load according to their capacity and fail due to breakage. Both cases can theoretically be justified when no flaw exists in the FRP composite material (Figure 2-2). Incomplete bonding at the interface of the matrix and fibers, air entrapment, uneven distribution of fibers within the matrix, and premature cracks

between layers of laminate are several common manufacturing defects in FRP composites [58].

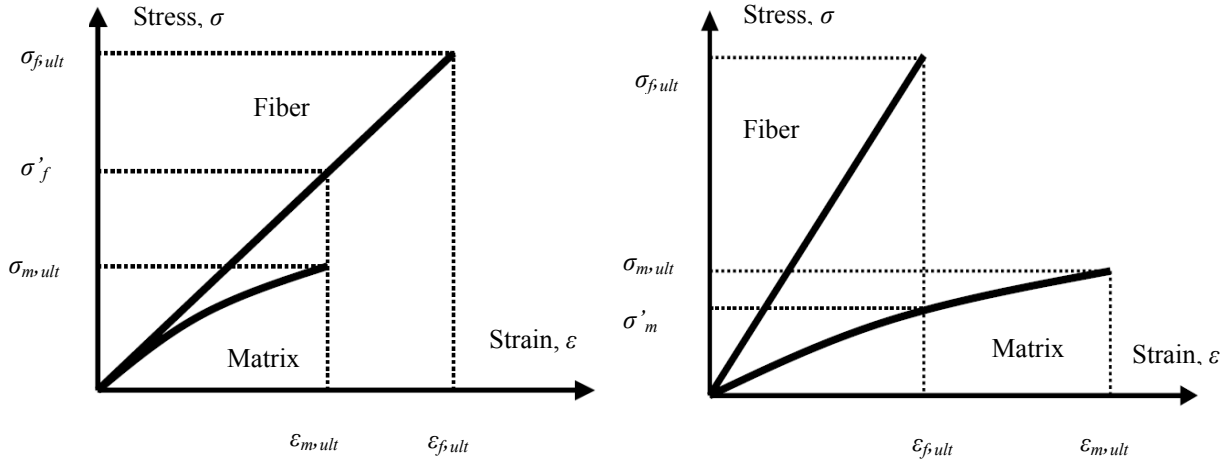

Figure 2-2 Stress-strain curves for the matrix and fiber materials: (a) Fibers have larger failure strain than that the matrix, and (b) The matrix has larger failure strain than fiber [58]

Depending on the matrix and fiber material properties and the above mentioned imperfections, matrix cracking, fiber pull-out, fiber breakage or delamination is expected to occur and cause a crack formation in a FRP structure due to the intrinsic brittleness of these materials under extensive loadings. These damage modes will reduce the structure's capacity to endure extra loadings; however, they may not lead to complete failure and collapse of the structure. Examining the initiation, stability and growth of defects are directly linked to the comprehensive study of fracture mechanics and the theory of plasticity.

2.3 Fracture Mechanics

Structural damage associated with the crack causes the local stresses and global deformations to increase for the body near the cracked area. Three independent modes are applied to define any coupled fracture deformation of a given structure (Figure 2-3) [59]:

1. Opening mode (mode I), when two faces of the crack are pulled away in the crack's plane.

2. Sliding (shearing) mode (mode II), when two faces of the crack are sliding over each other in the crack's plane.

3. Tearing mode (mode III), when two faces of the crack are taken apart out of the crack's plane.

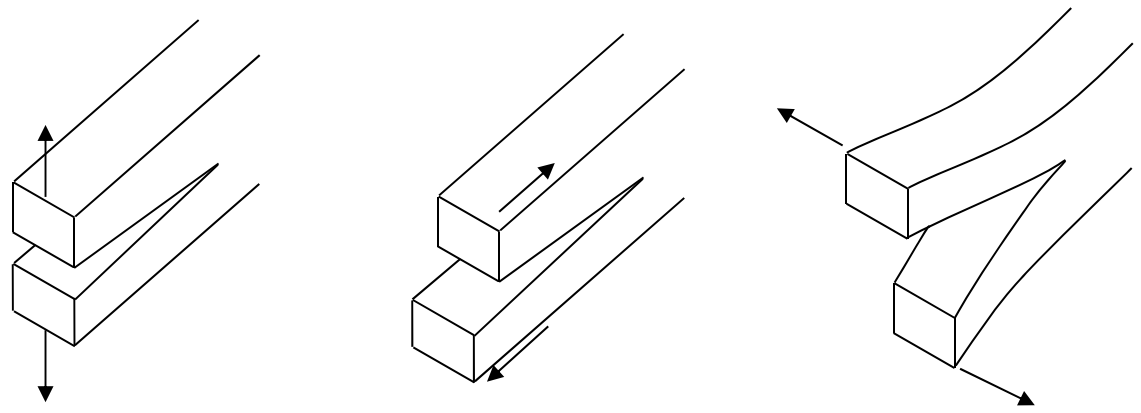

Figure 2-3 Dominant fracture modes of a cracked body: (a) Opening mode (mode I), (b) Sliding (shearing) mode (mode II), and (c) Tearing mode (mode III) [59]

Degradation and loss of the integrity of a structure can be drastically increased due to the crack formation (and propagation) which entails a careful scrutiny of different fracture modes with respect to the composite material composition and structural loadings. In this regard, the classical fracture mechanics can be categorized into linear elastic and elastic-plastic fracture depending on the type of material under study. Linear elastic fracture mechanics (LEFM) discusses deformation and stress fields around the crack-tip when a small plastified zone forms in the cracked region relative to the crack length. In such a case, singular stress fields emerge at the crack-tip. In LEFM, the stress intensity factors (SIFs) are applied to assess the stability of the crack by comparing it to critical SIFs extracted from experiments. The Westergaard [60] solution is a well-known approach in applying SIFs to estimate the displacement and stress fields near the crack-tip. Despite the capability of LEFM in estimating the fracture properties of brittle materials, with the extension of the plastic zone or the fracture process zone the singular stress fields vanish from the crack-tip region (e.g., crack propagation in steel structures). For such cases, elastic-plastic fracture mechanics (EPFM) proposes more accurate solutions and considers a plastic zone in front of the crack-tip region where extensive plastic deformation is expected to emerge. Wells [61] proposed the crack-tip opening displacement (CTOD) as a failure threshold for a structure. As an extension to the nonlinear analysis of such plastic zones, the J-integral was introduced by Rice [62] to accurately evaluate the energy release rate of materials when the Griffith theory is imprecise.

In general, fracture mechanics of a composite material is more challenging in comparison to other homogenous materials. The heterogeneous composition of FRP composite materials entail complex fracture phenomenon such as delamination. As mentioned before, delamination is one of the failure modes in FRP composite materials and can occur because of

a weak bonding between composite layers, an existing crack in the matrix material, broken fibers, fatigue, impact loadings, etc. In multi-layer laminated FRP composite structures, fibers in each layer are confided by adjacent layers on the top and bottom faces and the matrix acts as the bonding agent. When a crack forms in the matrix, the brittle nature of the matrix lets the LEFM accurately assess the crack stability and propagation pattern. On the other hand, in unidirectional laminated FRP composite structures, especially when formed using a moulding process with high compression pressure, fibers can penetrate into adjacent layers and the bonding between layers can be affected by fibers penetration (called fiber bridging). In this case, fibers onset an extra resisting force and prevent the crack from opening and the fracture behaviour of the structure demonstrates similar properties to those experienced during an elastic-plastic fracture. This aspect of FRP composites has increased the need for more advanced techniques of modeling their fracture phenomena and the governing failure modes.

2.4 Damage Mechanics Models

Several numerical investigations have been focused on the plasticity and damage modeling to consider defects in FRP composite structures. In these models, some failure criteria are pre-defined for the FRP composite and, based on the stress fields in the structure, failed elements are identified. Depending on the failure mode and numerical modeling technique, distorted elements may be eliminated from the model, or their stiffness would be degraded to simulate the material softening. Erdogan and Sih [63] introduced the maximum stress criterion which compares the principal stresses in each direction of an element with the material allowable stresses to evaluate the dominant failure mode. Hoffman [64] proposed that when the maximum strain criterion is similar to the maximum stress criteria, the principal strains in the

material directions are compared to the material strains capacity. Tsai [65] applied the Hill's yield surface and redefined the Tsai-Hill theory. The yield surface based on the Tsai-Hill criterion is defined as:

$$\left(\frac{\sigma_{11}}{T_{11}}\right)^2+\left(\frac{\sigma_{22}}{T_{22}}\right)^2+\left(\frac{\sigma_{33}}{T_{33}}\right)^2+\left(\frac{\sigma_{12}}{T_{12}}\right)^2+\left(\frac{\sigma_{23}}{T_{23}}\right)^2+\left(\frac{\sigma_{13}}{T_{13}}\right)^2 - \left(\frac{1}{T_{11}^2}+\frac{1}{T_{22}^2}+\frac{1}{T_{33}^2}\right)\left(\sigma_{11}\sigma_{22}+\sigma_{33}\sigma_{22}+\sigma_{11}\sigma_{33}\right)=YS_{normal} \tag{2-6}$$

where σ_{ij}, T_{ij} and YS_{normal} are the stresses in different material directions, material strengths and normalized failure threshold, respectively.

Tsai and Wu [66] also presented a failure theory based on the strengths criterion for anisotropic materials. The Tsai-Wu failure criterion could differentiate between material tensile and compressive strength and ignores the interaction between failure modes. Based on this criterion, the failure surface can be expressed as follows:

$$F_{ij}\sigma_i\sigma_j+F_i\sigma_i=YS_{normal} \tag{2-7}$$

where σ_i, F_i and F_{ij} are the re-arranged vector of stress tensor, second and fourth order strength tensors, respectively.

Specifically for unidirectional (UD) laminated composite materials, Hashin [67] introduced a set of failure modes based on the combination of fibers and matrix strengths. The failure criteria proposed by Hashin [67] can be summarized as follows:

1- Tensile fiber failure for $\sigma_{11}\geq 0$:

$$\left(\frac{\sigma_{11}}{X_T}\right)^2+\frac{\sigma_{12}^2+\sigma_{13}^2}{S_{12}^2}=\begin{cases}\geq 1 & Failure\\ <1 & No\ Failure\end{cases} \tag{2-8}$$

2- Compressive fiber failure for $\sigma_{11}<0$:

$$\left(\frac{\sigma_{11}}{X_C}\right)^2=\begin{cases}\geq 1 & Failure\\ <1 & No\ \ Failure\end{cases} \tag{2-9}$$

3- Tensile matrix failure for $\sigma_{22}+\sigma_{33}>0$:

$$\left(\frac{\sigma_{22}+\sigma_{33}}{Y_T}\right)^2+\frac{\sigma_{23}^2-\sigma_{22}\sigma_{33}}{S_{23}^2}+\frac{\sigma_{12}^2+\sigma_{13}^2}{S_{12}^2}=\begin{cases}\geq 1 & Failure\\ <1 & No\ Failure\end{cases} \tag{2-10}$$

4- Compressive matrix failure for $\sigma_{22}+\sigma_{33}<0$:

$$\left[\left(\frac{Y_C}{2S_{23}}\right)^2-1\right]\left(\frac{\sigma_{22}+\sigma_{33}}{Y_C}\right)+\frac{\left(\sigma_{22}+\sigma_{33}\right)^2}{4S_{23}^2}+$$
$$\frac{\sigma_{23}^2-\sigma_{22}\sigma_{33}}{S_{23}^2}+\frac{\sigma_{12}^2+\sigma_{13}^2}{S_{12}^2}=\begin{cases}\geq 1 & Failure\\ <1 & No\ Failure\end{cases} \tag{2-11}$$

5- Interlaminar tensile failure for $\sigma_{33}>0$:

$$\left(\frac{\sigma_{33}}{Z_T}\right)^2=\begin{cases}\geq 1 & Failure\\ <1 & No\ Failure\end{cases} \tag{2-12}$$

6- Interlaminar compression failure for $\sigma_{33}<0$:

$$\left(\frac{\sigma_{33}}{Z_C}\right)^2 = \begin{cases} \geq 1 & Failure \\ < 1 & No\ Failure \end{cases} \tag{2-13}$$

where X_T, Y_T, Z_T, X_C, Y_C, Z_C, S_{12}, S_{13} and S_{23} are the tensile, compressive and shear strengths in different material directions.

2.5 Comparison between Fracture Mechanics and Damage Mechanics

In general, fracture mechanics focuses on local discontinues where macro-cracks are present. It observes the singular stress and strain fields in front of the crack-tip, especially in brittle materials, and provides an accurate estimation of the damage evolution when a flaw exists in the structure. On the other hand, damage mechanics tends to evaluate the stress and strain state in the structure and assess whether the material faces degradation in each loading step. In addition, it can be applied to study the global behaviour of the structure and predict the failure initiation and expansion trend due to the material deterioration. Hence, depending on the problem encountered, an appropriate approach should be selected to accurately evaluate the structural behaviour of the composite. In the present work, the focus on the local damage modelling of FRP composite materials would prompt the implementation of fracture mechanics due to the local nature of delamination and brittle properties of such materials. However, the large process zone existing in the delamination front will require the implementation of elastic-plastic fracture mechanics to ensure the accurate evaluation of the structural deformation (this will be formulated in detail in Section 3.2).

2.6 Introduction of Extended Finite Element Method

Numerical modeling is an important part of most engineering applications. In many cases, a structure's dimensions and the test set-up configurations cause limitations when performing full-scale experimental studies, increasing the demand for undertaking more numerical analyses. A variety of numerical modeling techniques have been proposed in the past decades and can be categorized into mesh free methods such as Smoothed Particle Hydrodynamics (SPH), Element-Free Galerkin Method (EFGM), Finite Difference Method (FDM) and Meshless Methods as well as mesh-based methods such as Finite Element Method (FEM) and Boundary Element Method (BEM).

The FEM can be directly enhanced and used in modeling discontinuities by introducing the partition of unity method (PUM), proposed by Melenk and Babuška [33], to approximation functions. The basis of PUM is similar to regular finite element approximation where the summation of all shape functions at any Gauss point is equal to one. The new method is known as the extended finite element method (XFEM) [31-32]. The XFEM has demonstrated to be a more accurate and convenient solution where the conventional finite element produces rough or highly oscillatory results. In XFEM, similar to conventional FEM, the finite element mesh is generated regardless of discontinuities locations. Then, specific search algorithms such as the level-set or fast marching methods are utilized to identify the location of any discontinuity with respect to the existing mesh and distinguish the different types of required enrichments for the affected mesh elements. Next, additional auxiliary degrees of freedom are added to the conventional FEM approximation in selected nodes around the discontinuity. These degrees of freedom assist the model in capturing the displacement jumps caused by discontinuities.

Assume a discontinuity (a crack) within an arbitrary finite element mesh (Figure 2-4). The displacement field of point x, $u^g(x)$, inside the domain can be described in two parts; the conventional finite element approximation, and the XFEM enriched field defining the discontinuity [32]:

$$u^g(x) = \sum_{\substack{I \\ n_I \in N^{all}}} \phi_I(x) u_I^{ord} + \sum_{\substack{J \\ n_J \in N^f}} \phi_J(x) \psi(x) u_J^{enr} \tag{2-14}$$

where $\phi(x)$ is the conventional shape function (also often shown in the literature by $N(x)$), $\psi(x)$ is the general enrichment function, N^{all} is the finite element mesh nodes and N^f is the enriched nodes of the mesh, u^{ord} is the classic degrees of freedom at each node and u^{enr} is the additional enriched degree of freedom at the J^{th} enriched node.

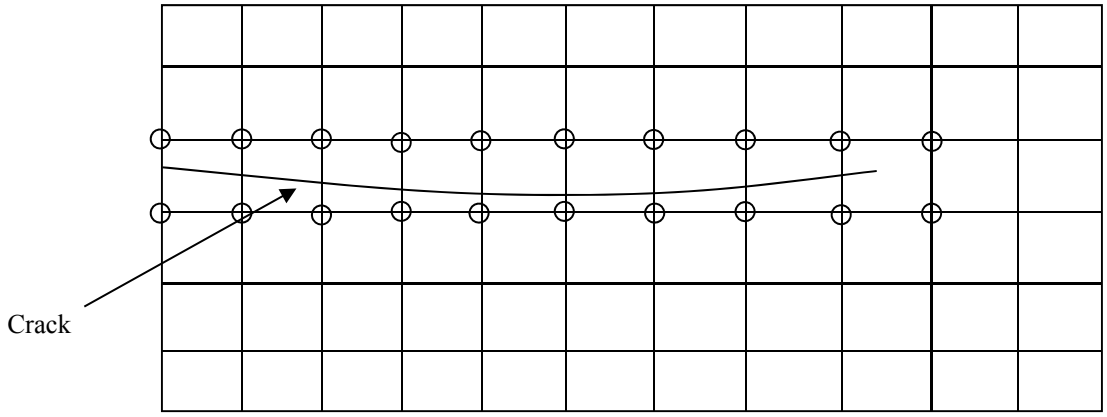

Figure 2-4 An arbitrary finite element mesh with a discontinuity (circles represent the enriched nodes of the mesh)

In order to choose the enrichment function, any discontinuous function in the problem domain can be employed to estimate the displacement field approximation in vicinity of the crack. A

function that satisfies such a requirement is the Heaviside step function ($H(\mathbf{x})$). It gains a '+1' value on one side of the crack and '-1' on the other side of the crack and can be utilized when the crack propagation is modeled by straight line segments. To find the Heaviside function value at each node of an element, tangential and normal vectors of the crack surface curve should be measured. If X^* is the nearest point of a crack to the point *X'*, Figure 2-5, and $e_{\mathbf{n}}$ is the unit normal vector of the crack alignment in which $e_s \times e_n = e_z$ (e_s is the unit tangential vector), then using a scalar product between the distance vector of the element's nodes and the normal vector of the crack surface, the Heaviside function value can be calculated.

$$H(\mathbf{x}) = \begin{cases} +1 & ;if\ (X' - X^*).e_n > 0 \\ -1 & ;otherwise \end{cases} \tag{2-15}$$

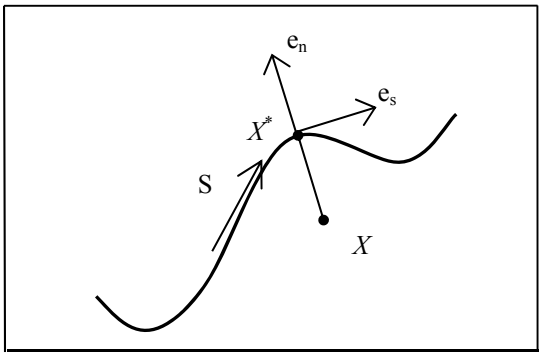

Figure 2-5 Unit tangential and normal vectors for the Heaviside function and nearest point to *X* on the crack surface; X^*

Another set of functions utilized in XFEM are those extracted from an analytical solution of the near crack-tip displacement fields in LEFM as follows [68]:

$$u_x^{tip} = \frac{1}{2G_{12}}\sqrt{\frac{r}{2\pi}}\left\{K_I \cos\frac{\theta}{2}\left(3-4v_{12}-\cos\theta\right)+K_{II}\sin\frac{\theta}{2}\left(3-4v_{12}+2+\cos\theta\right)\right\} \tag{2-16}$$

$$u_y^{tip} = \frac{1}{2G_{12}}\sqrt{\frac{r}{2\pi}}\left\{K_I \sin\frac{\theta}{2}\left(3-4v_{12}-\sin\theta\right)+K_{II}\cos\frac{\theta}{2}\left(3-4v_{12}-2+\cos\theta\right)\right\} \tag{2-17}$$

$$u_z^{tip} = \frac{2}{G_{12}}\sqrt{\frac{r}{2\pi}}K_{III}\sin\frac{\theta}{2} \tag{2-18}$$

where u_x^{tip}, u_y^{tip}, u_z^{tip}, K_I, K_{II} and K_{III} are the crack-tip displacement field and stress intensity factors (SIFs) in the three standard fracture modes, and (r, θ) are the local polar coordinate system at the crack-tip.

Subsequently, the extracted crack-tip enrichment functions were proposed by Moës et al. [32] as:

$$\left\{F^{enr}(r,\theta)\right\}_{i=1}^{4} = \left\{\sqrt{r}\sin\frac{\theta}{2}, \sqrt{r}\cos\frac{\theta}{2}, \sqrt{r}\sin\frac{\theta}{2}\sin\theta, \sqrt{r}\cos\frac{\theta}{2}\sin\theta\right\} \tag{2-19}$$

Among presented functions, $\sqrt{r}\sin\frac{\theta}{2}$ is the only discontinuous function and the remaining functions are continuous.

A more general set of enrichment functions can be achieved by studying the crack asymptotic displacement fields in anisotropic materials. For such a case, with general boundary conditions and the structure subjected to arbitrary forces, the following characteristic equation can be obtained using the equilibrium of forces and compatibility conditions [69]:

$$a_{11}\mu^4 - 2a_{16}\mu^3 + \left(2a_{12}+a_{66}\right)\mu^2 - 2a_{26}\mu + a_{22} = 0 \tag{2-20}$$

where a_{ij} is the material compliance matrix components.

Lekhnitskii [69] illustrated that the roots of Equation (2-20) are always complex or purely imaginary $\left(\mu_k = \mu_{kx} + i\mu_{ky},\ k = 1,\ 2\right)$ with the conjugate pairs as μ_1, $\overline{\mu}_1$ and μ_2, $\overline{\mu}_2$. Employing the above equations, the displacement fields in the vicinity of the crack-tip were elicited by Sih et al. [70] by means of analytical functions and complex variables as follows:

$$u_x^{tip} = K_I \sqrt{\frac{2r}{\pi}}\ \mathrm{Re}\left[\frac{1}{\mu_1 - \mu_2}\left\{\mu_1 p_2 \sqrt{\cos\theta + \mu_2 \sin\theta} - \mu_1 p_1 \sqrt{\cos\theta + \mu_1 \sin\theta}\right\}\right] \tag{2-21}$$

$$u_y^{tip} = K_I \sqrt{\frac{2r}{\pi}}\ \mathrm{Re}\left[\frac{1}{\mu_1 - \mu_2}\left\{\mu_1 q_2 \sqrt{\cos\theta + \mu_2 \sin\theta} - \mu_1 q_1 \sqrt{\cos\theta + \mu_1 \sin\theta}\right\}\right] \tag{2-22}$$

For pure mode II:

$$u_x^{tip} = K_{II} \sqrt{\frac{2r}{\pi}}\ \mathrm{Re}\left[\frac{1}{\mu_1 - \mu_2}\left\{p_2 \sqrt{\cos\theta + \mu_2 \sin\theta} - p_1 \sqrt{\cos\theta + \mu_1 \sin\theta}\right\}\right] \tag{2-23}$$

$$u_y^{tip} = K_{II} \sqrt{\frac{2r}{\pi}}\ \mathrm{Re}\left[\frac{1}{\mu_1 - \mu_2}\left\{q_2 \sqrt{\cos\theta + \mu_2 \sin\theta} - q_1 \sqrt{\cos\theta + \mu_1 \sin\theta}\right\}\right] \tag{2-24}$$

where Re denotes the real part of complex variable. p_k and q_k can also be defined [70]:

$$p_k = a_{11}\mu_k^2 + a_{12} - a_{16}\mu_k \tag{2-25}$$

$$q_k = a_{12}\mu_k + \frac{a_{22}}{\mu_k} - a_{26} \tag{2-26}$$

Using the above equations, the near crack-tip enrichment functions for the crack in an anisotropic material are expressed as [71]:

$$\left\{F^{enr}(r,\theta)\right\}_{i=1}^{4} = \left\{\sqrt{r}\cos\frac{\theta_1}{2}\sqrt{g_1(\theta)}, \sqrt{r}\cos\frac{\theta_2}{2}\sqrt{g_2(\theta)}, \sqrt{r}\sin\frac{\theta_1}{2}\sqrt{g_1(\theta)}, \sqrt{r}\sin\frac{\theta_2}{2}\sqrt{g_2(\theta)}\right\} \tag{2-27}$$

where $g_k(\theta)$ and θ_k, $(k = 1, 2)$ are defined as:

$$g_k(\theta) = \sqrt{\left(\cos\theta + \mu_{xy}\sin\theta\right)^2 + \left(\mu_{xy}\sin\theta\right)^2} \tag{2-28}$$

$$\theta_k = \arctan\left(\frac{\mu_{ky}\sin\theta}{\cos\theta + \mu_{kx}\sin\theta}\right) \tag{2-29}$$

Moës et al. [32] substituted the Heaviside and near crack-tip enrichment functions in the XFEM approximation and presented the following equation:

$$\begin{aligned} u^g(x) = & \sum_{\substack{I \\ n_I \in N^{all}}} \phi_I(x) u_I + \sum_{\substack{J \\ n_J \in N^g_{node}}} \phi_J(x) H(x) b_J^H + \sum_{\substack{k \\ k \in K^1_{node}}} \phi_k(x) \left(\sum_i \left(c_k^{tip}\right)_i^1 \left(F^{enr}(x)\right)_i^1 \right) \\ & + \sum_{\substack{l \\ l \in K^2_{node}}} \phi_l(x) \left(\sum_i \left(c_l^{tip}\right)_i^2 \left(F^{enr}(x)\right)_i^2 \right) \end{aligned} \tag{2-30}$$

where N^g_{node} is the set of nodes that have a crack face (but not a crack-tip) in their influence domain, b^H is the vector (in multi-dimensional problems) of additional degrees of freedom which are related to the modeling of crack faces (not crack-tips), c^{tip} is the vector of additional degrees of freedom for modeling crack-tips, $F^{enr}(x)$ is the crack-tip enrichment function and K^1_{node} and K^2_{node} are the sets of nodes associated with the crack-tip 1 and 2 in their influence domains, respectively. Figure 2-6 illustrates a finite element mesh for modeling the existing discontinuity in Figure 2-4. Nodes that need to be enriched with Heaviside and near crack-tip functions are distinguished by circles and rectangles, respectively. Other nodes that are not affected by the crack remain well within the classical finite element framework.

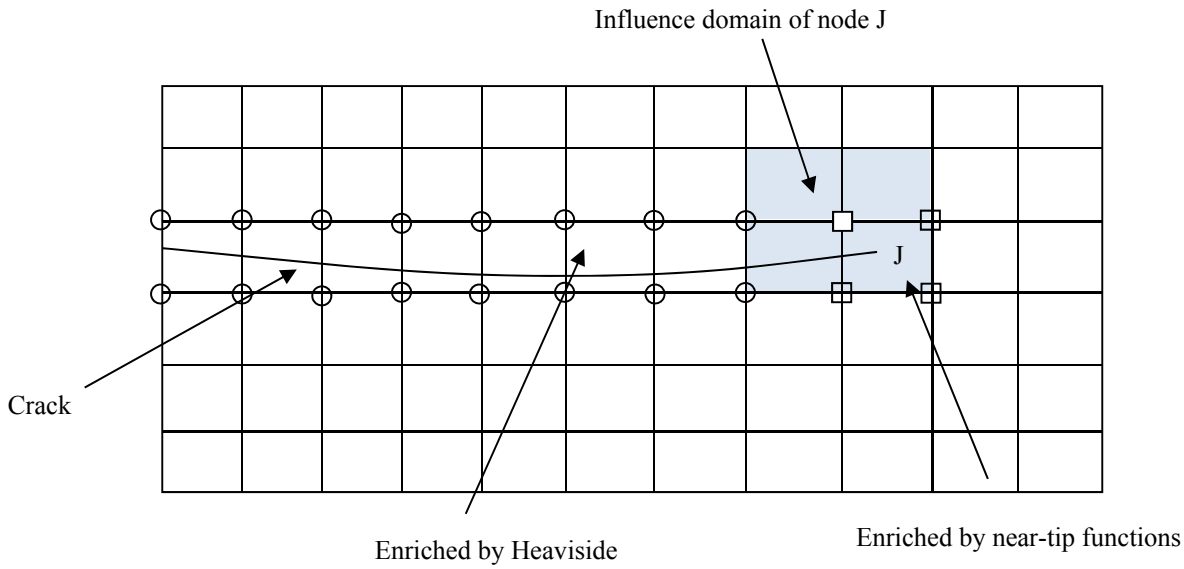

Figure 2-6 The influence domain of node J in an arbitrary finite element mesh

The XFEM displacement approximation in Equation (2-30) can be implemented in numerical modeling with LEFM to predict the displacement field in a cracked structure. Considering the total potential energy governing the problem, we can write:

$$\int_{\Gamma_V} \sigma_{ij} \cdot \delta \varepsilon_{ij} d\Gamma_V = \int_{\Gamma_V} f_i^b \cdot \delta u^k d\Gamma_V + \int_{\Gamma_t} f_i^t \cdot \delta u^k d\Gamma_t \tag{2-31}$$

where Γ_V, Γ_t, f_i^b, f_i^t and u^k denote the body domain, traction surfaces, body forces, external forces vectors and displacement field, respectively. Discretizing the Equation (2-31) and applying the variational formulation, the following linear algebraic equation can be written:

$$K^0 u^h = R^0 \tag{2-32}$$

Where K^0, R^0 and u^h denote the initial stiffness matrix, right hand side vector of external forces and general vector containing all the nodal parameters including the ordinary, crack face and the crack-tip enriched degrees of freedom vectors, respectively:

$$u^h = \left\{ u^{ord}, b^H, c^{tip} \right\}^{\mathbf{T}} \tag{2-33}$$

In Equation (2-32), the initial stiffness matrix and the right hand side vector of external forces are also defined as:

$$K^0 = \begin{bmatrix} K_{ij}^{u^{ord}u^{ord}} & K_{ij}^{u^{ord}b^H} & K_{ij}^{u^{ord}c^{tip}} \\ K_{ij}^{b^H u^{ord}} & K_{ij}^{b^H b^H} & K_{ij}^{b^H c^{tip}} \\ K_{ij}^{c^{tip}u^{ord}} & K_{ij}^{c^{tip}b^H} & K_{ij}^{c^{tip}c^{tip}} \end{bmatrix} \tag{2-34}$$

$$R^0 = \left\{ R^{0^{u^{ord}}}, R^{0^{b^H}}, R^{0^{c^{tip}}} \right\}^T \tag{2-35}$$

The stiffness arrays $K_{ij}^{rs}\,(r, s = u^{ord}, b^H, c^{tip})$ in Equation (2-34) include the classical, enriched and coupled components of XFEM approximation:

$$K_{ij}^{rs} = \int_{\Omega^{\mathbf{e}}} (B_i^r)^{\mathrm{T}} D B_j^s d\Omega \qquad \mathbf{(}r, s = u^{ord}, b^H, c^{tip}\mathbf{)} \tag{2-36}$$

where B is the matrix of derivatives of shape functions and is defined as:

$$B_i^{u^{ord}} = \begin{bmatrix} N_{i,X} & 0 & 0 \\ 0 & N_{i,Y} & 0 \\ 0 & 0 & N_{i,Z} \\ N_{i,Y} & N_{i,X} & 0 \\ 0 & N_{i,Z} & N_{i,Y} \\ N_{i,Z} & 0 & N_{i,X} \end{bmatrix} \tag{2-37}$$

$$B_i^{b^H} = \begin{bmatrix} (N_i H - H_i)_{,X} & 0 & 0 \\ 0 & (N_i H - H_i)_{,Y} & 0 \\ 0 & 0 & (N_i H - H_i)_{,Z} \\ (N_i H - H_i)_{,Y} & (N_i H - H_i)_{,X} & 0 \\ 0 & (N_i H - H_i)_{,Z} & (N_i H - H_i)_{,Y} \\ (N_i H - H_i)_{,Z} & 0 & (N_i H - H_i)_{,X} \end{bmatrix} \tag{2-38}$$

$$B_i^{c^{tip}} = \begin{bmatrix} \left(N_i F^{enr\,k} - F_i^{enr\,k}\right)_{,X} & 0 & 0 \\ 0 & \left(N_i F^{enr\,k} - F_i^{enr\,k}\right)_{,Y} & 0 \\ 0 & 0 & \left(N_i F^{enr\,k} - F_i^{enr\,k}\right)_{,Z} \\ \left(N_i F^{enr\,k} - F_i^{enr\,k}\right)_{,Y} & \left(N_i F^{enr\,k} - F_i^{enr\,k}\right)_{,X} & 0 \\ 0 & \left(N_i F^{enr\,k} - F_i^{enr\,k}\right)_{,Z} & \left(N_i F^{enr\,k} - F_i^{enr\,k}\right)_{,Y} \\ \left(N_i F^{enr\,k} - F_i^{enr\,k}\right)_{,Z} & 0 & \left(N_i F^{enr\,k} - F_i^{enr\,k}\right)_{,X} \end{bmatrix} \tag{2-39}$$

where H_i and F_i^{enr} are the Heaviside and crack-tip enrichment functions at element nodes. Normalizing the enrichment functions by mean of deducting the enrichment functions at element nodes will readily satisfy the PUM fundamental (i.e., the summation of normalized enrichment functions for a given node will be the unity). Also, the *k* index is used to differentiate between different enrichment functions, respectively.

2.7 Application of XFEM in Linear Elastic Fracture Mechanics

As addressed earlier, the linear elastic fracture mechanics (LEFM) is a suitable tool for the analysis of many materials with a small plastic or process zone in front of the crack-tip. The SIFs are the only required variables for assessing the stress and displacement fields around the crack-tip under different loading and subsequently, measuring the stability of the crack by

comparing SIFs to their critical values extracted from the experiments. In terms of numerical modeling of LEFM problems, XFEM provides an accurate estimation of the stress and displacement fields around the crack-tip using the Heaviside and crack-tip enrichment functions. To further the application of XEFM in LEFM, it is also required to introduce a post-processing procedure to evaluate the SIFs. For this purpose, the interaction integral, known as M-integral, was proposed by Moës et al. [32] and Dolbow et al. [72] for isotropic materials and extended to orthotropic materials by Kim and Paulino [73]. The interaction integral is essentially derived from the J-integral introduced by Rice [72] as in Equation (2-40).

$$J_k = \int_{\Gamma+\Gamma_c} \left(W n_k - t_i \frac{\partial u_j}{\partial X_k} \right) d\Gamma \tag{2-40}$$

where $W = (1/2)\sigma_{ij}\varepsilon_{ij}$ is the strain energy density, X_i, t_i and n_k represent Lagrangian coordinates, vectors of surface traction and vectors of outward normal direction, respectively, and the integral paths Γ and Γ_c denote far-field and crack surface paths, respectively, as shown in Figure 2-7.

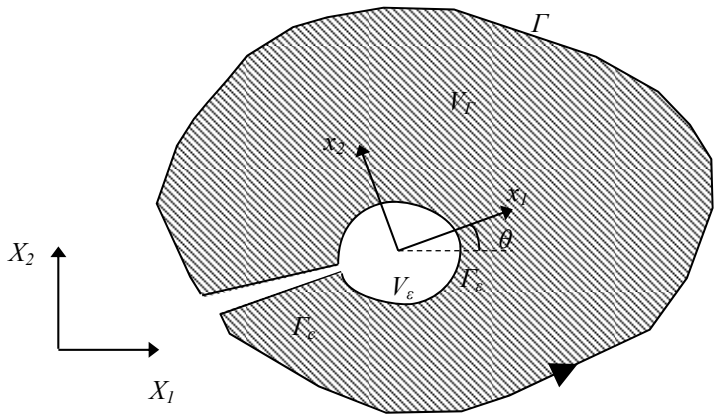

Figure 2-7 Local crack-tip coordinates and the contour Γ and its interior area, V_Γ

The form of equation (2-40) is not perfectly suited for FEM implementations and an equivalent form can be obtained by applying the divergence theorem and several additional assumptions, as discussed by Kim and Paulino [73]:

$$J_k = \int_{V_\Gamma} \left(\sigma_{ij} \frac{\partial u_j}{\partial X_k} - W \right) q'_{,k} \, dV_\Gamma + \int_{V_\Gamma} \left\{ \sigma_{ij} \left(\frac{\partial^2 u_j}{\partial X_j \partial X_k} - \frac{\partial \varepsilon_{ij}}{\partial X_k} \right) - \frac{1}{2} \frac{\partial C_{ijlm}}{\partial X_k} \varepsilon_{lm} \varepsilon_{ij} \right\} q' dV_\Gamma \qquad (2\text{-}41)$$

where q' is a function smoothly changing from $q'=0$ at the exterior boundary Γ to $q'=1$ near the crack-tip. In the present study, q' is assumed to be varying linearly from 1 to 0. Noting that the value of q is constant near the crack-tip area, distinguished by shaded unaffected elements in Figure 2-7, the gradient of q' vanishes in Equation (2-41). By adopting auxiliary displacement, stress and strain fields ($u_k^{Auxilairy}$, $\sigma_{ij}^{Auxilairy}$, $\varepsilon_{ij}^{Auxilairy}$) and superimposing them to displacement, stress and strain fields (u_k, σ_{ij}, ε_{ij}), the superimposed J-integral will contain the following parts:

$$J_{Superimposed} = J + J_{Auxiliary} + M \tag{2-42}$$

where M is the interaction integral in the local crack-tip 2D Polar coordinate and consists of terms involving products of actual and auxiliary fields. The Cartesian coordinate definition of M-integral is then as follows:

$$\begin{aligned} M_k = & \int_{V_\Gamma} \left\{ \sigma_{ij} \frac{\partial u_i^{aux}}{\partial X_k} + \sigma_{ij}^{aux} \frac{\partial u_i}{\partial X_k} - \left(W + W^{aux} \right) \right\} q'_{,k} \, dV_\Gamma \\ & + \int_{V_\Gamma} \left\{ \sigma_{ij} \left(\frac{\partial^2 u_i^{aux}}{\partial X_j \partial X_k} - \frac{\partial \varepsilon_{ij}^{aux}}{\partial X_k} \right) - \frac{\partial C_{ijlm}}{\partial X_k} \varepsilon_{ij} \varepsilon_{lm}^{aux} \right\} q' \, dV_\Gamma \qquad (i, j, k = 1, 2, 3) \end{aligned} \tag{2-43}$$

To extract the M-integral in local crack-tip Polar coordinates, a simple transformation can be employed:

$$M_{Local} = M_1 \cos\theta + M_2 \sin\theta \tag{2-44}$$

Now, if one wants to relate the superimposed J-integral to the energy release rate, G, of the two actual and auxiliary fields, the following relationship between SIFs and M-integral can be derived:

$$J = G = G_I + G_{II} = c_{11} K_I^2 + c_{12} K_I K_{II} + c_{22} K_{II}^2 \tag{2-45}$$

$$J_{Superimposed} = c_{11} \left(K_I + K_I^{aux} \right)^2 + c_{12} \left(K_I + K_I^{aux} \right) \left(K_{II} + K_{II}^{aux} \right) + c_{22} \left(K_{II} + K_{II}^{aux} \right)^2 \tag{2-46}$$

$$J_{Auxiliary} = c_{11} \left(K_I^{aux} \right)^2 + c_{12} K_I^{aux} K_{II}^{aux} + c_{22} \left(K_{II}^{aux} \right)^2 \tag{2-47}$$

$$M_{Local} = 2c_{11} K_I K_I^{aux} + c_{12} \left(K_I^{aux} K_{II} + K_I K_{II}^{aux} \right) + 2c_{22} K_{II} K_{II}^{aux} \tag{2-48}$$

where c_{11}, c_{12} and c_{22} are defined as follows:

$$c_{11} = -\frac{a_{22}}{2}\,\mathrm{Im}\left(\frac{\mu_1+\mu_2}{\mu_1\mu_2}\right) \tag{2-49}$$

$$c_{12} = -\frac{a_{22}}{2}\,\mathrm{Im}\left(\frac{1}{\mu_1\mu_2}\right) + \frac{a_{11}}{2}\,\mathrm{Im}\left(\mu_1\mu_2\right) \tag{2-50}$$

$$c_{22} = \frac{a_{11}}{2}\,\mathrm{Im}\left(\mu_1+\mu_2\right) \tag{2-51}$$

Finally, by solving the following algebraic equations for the auxiliary field for mode I and II, SIFs can be extracted:

$$M_{Local} = 2c_{11}K_I + c_{12}K_{II} \quad for\ K_I^{aux} = 1.0\ and\ K_{II}^{aux} = 0.0 \tag{2-52}$$

$$M_{Local} = 2c_{11}K_I + c_{12}K_{II} \quad for\ K_I^{aux} = 1.0\ and\ K_{II}^{aux} = 0.0 \tag{2-53}$$

2.8 Application of XFEM in Elasto-Plastic Fracture Mechanics

In contrast to LEFM, EPFM deals with ductile materials with a relatively large plastic or process zone in front of the crack-tip. Irwin [74] proposed a simple plastic zone correction to SIFs in order to consider the plastification effects. Alternative solutions were also introduced by Dugdale [75] and Barenblatt [76] to correct plastic zone characteristics. Wells [61] offered crack-tip opening displacement (CTOD) as an independent variable to measure the fracture energy toughness of materials. This approach covered not only the LEFM but also established a way to investigate the EPFM in materials. Later, Rice [62] introduced a path independent contour integral, the J-integral, to describe the stress and strain distribution near the crack-tip. It is worth mentioning that the J-integral was earlier extracted by Eshelby [77], however; the application of this method in studying LEFM and EPFM was proposed by Rice [62].

As mentioned in Section 4.2, the interaction integral method has been frequently adopted in LEFM crack analyses to evaluate mixed mode SIFs. One disadvantage of this method is related to the dependency of the method on the auxiliary field exact solution. In terms of EPFM, XFEM potential has left behind such limitations and provided a convenient solution. Motamedi and Mohammadi [78 - 79] implemented dynamic J-integral and CTODs to assess the SIFs in orthotropic materials. Definition of Equation (2-41) can be applied to measure the tangential component of the J-integral which corresponds to the rate of changes in the potential energy per unit crack extension, namely, the energy release rate (G):

$$G = J_1 \cos\theta_0 + J_2 \sin\theta_0 \tag{2-54}$$

where θ_0 is the crack angle. In order to accurately evaluate the stress and displacement fields around the crack-tip, the component separation method, proposed by Aliabadi and Sollero [80], was employed. They discussed that the following relationship between the stress intensity factors and the CTODs of the crack faces can be obtained:

$$\begin{Bmatrix} \delta_n \\ \delta_t \end{Bmatrix} = \sqrt{\left(\frac{8r}{\pi}\right)} \begin{bmatrix} D_{11} & D_{12} \\ D_{21} & D_{22} \end{bmatrix} \begin{Bmatrix} K_I \\ K_{II} \end{Bmatrix} \tag{2-55}$$

with

$$\begin{aligned} D_{11} &= Im\left(\frac{\mu_2 p_1 - \mu_1 p_2}{\mu_1 - \mu_2}\right), D_{12} = Im\left(\frac{p_1 - p_2}{\mu_1 - \mu_2}\right) \\ D_{21} &= Im\left(\frac{\mu_2 q_1 - \mu_1 q_2}{\mu_1 - \mu_2}\right), D_{22} = Im\left(\frac{q_1 - q_2}{\mu_1 - \mu_2}\right) \end{aligned} \tag{2-56}$$

Where p_1, p_2, q_1 and q_2 are defined as follows:

$$p_1 = a_{11}\left(1+\mu_1^2\right)+a_{12} \tag{2-57}$$

$$p_2 = a_{11}\left(1+\mu_2^2\right)+a_{12} \tag{2-58}$$

$$q_1 = \frac{a_{12}\left(1+\mu_1^2\right)+a_{22}}{\mu_1} \tag{2-59}$$

$$q_2 = \frac{a_{12}\left(1+\mu_1^2\right)+a_{22}}{\mu_2} \tag{2-60}$$

Another set of relationships between the energy release rate and the SIFs was proposed by Wu [81]:

$$G = (1/2)K^T L(c)^{-1} K \tag{2-61}$$

where $L(c)$ was defined by Dongye and Ting [82] for orthotropic materials with the symmetry planes coinciding with the coordinate planes. The non-zero components of $L(c)$ are:

$$L_{33} = \sqrt{C_{55}C_{44}} \tag{2-62}$$

$$\sqrt{C_{66}C_{22}}\,L_{11} = \sqrt{C_{11}C_{66}}\,L_{22} = \Omega\Psi^{-\frac{1}{2}} \tag{2-63}$$

where C_{ij} is the constitutive/stiffness coefficients and

$$\Omega = (C_{11}C_{22} - C_{12}^2)\sqrt{C_{66}C_{66}} \tag{2-64}$$

$$\Psi = (C_{66} + \sqrt{C_{11}C_{22}})^2 - (C_{12} + C_{66})^2 \tag{2-65}$$

Therefore, the ratio of opening to sliding displacements, R_{COD}, can be written as:

$$R_{COD} = \frac{\delta_2}{\delta_1} = \frac{D_{21}K_I + D_{22}K_{II}}{D_{11}K_I + D_{12}K_{II}} \tag{2-66}$$

And the ratio of dynamic stress intensity factors, R_{SIF}, can be obtained as:

$$R_{SIF} = \frac{K_I}{K_{II}} = \frac{R_{COD}D_{21} - D_{22}}{D_{21} + R_{COD}D_{11}} \tag{2-67}$$

Substitution for K_I from Equation (2-61) into Equation (2-67) leads to the following relationship for K_{II}:

$$K_{II} = \sqrt{\frac{2G}{L_{11}(c)R_{SIF}^2 + L_{22}(c)}} \tag{2-68}$$

And for K_I, by definition we have:

$$K_I = K_{II}R_{SIF} \tag{2-69}$$

2.9 Application of Cohesive Interface in Fracture Mechanics

In several cases where the crack front experiences a large scale processing zone (e.g., large blunting with large scale plasticity, fibrous rupture or ductile rupture), the stress singularity disappears from the crack-tip and traction forces emerge on the surface of the crack to resist the extensive increase of CTOD. This failure behaviour is common in FRP composites, especially when two adjacent layers have a bridged fiber orientation. When premature crack initiates the growth, a damage zone appears in front of the crack tip and dissipates the high stress intensity expected in LEFM. This damage zone occurs in form of a cohesive zone (e.g., fiber bridging) and hinders the identification of the crack-tip using conventional methods. In

such problems, a complimentary approach to EPFM based on damage mechanics is required to provide accurate results.

2.9.1 Cohesive Zone Model

One of the advance methods for simulating the large process zone with traction forces is the cohesive zone model (CZM). The basis of this model is depicted in the work of Dugdale [75] and Barenblatt [76], where they improved the LEFM by correcting the plastic zone in front of the crack-tip to include the defect process zone and de-cohesion. Dugdale [75] assumed a finite stress equal to the yield stress of the material, which was contradictory to the crack-opening stress in brittle materials. Barenblatt [76] further investigated the traction existing on the crack surface and linked the traction magnitude to the distance from the crack-tip. Needleman [83] implemented a potential function to characterize the traction-separation model on the crack surface by considering a cohesive zone for ductile interfaces in metals. The potential function was defined as follows:

$$\varphi(\delta_n,\delta_t)=\varphi_0\left[1-\left(1+\frac{\delta_n}{\delta_{n0}}\right)\exp\left(\frac{-\delta_n}{\delta_{n0}}\right)\exp\left(\frac{-\delta_t^2}{\delta_{t0}^2}\right)\right] \tag{2-70}$$

where φ_0, δ_n, δ_t, δ_{n0} and δ_{t0} are the material fracture energy, normal and tangential crack opening displacements, normal and tangential parameter relative to the model. Based on this potential function, with cohesive tractions on the crack surface, normal and shear tractions (σ_n and σ_t) are functions of crack opening/sliding displacements. The cohesive normal and tangential tractions can be extracted by finding the derivative of the potential function over the crack opening/sliding displacements as follows:

$$\sigma_n = \frac{\partial \varphi(\delta_n, \delta_t)}{\partial \delta_n} \tag{2-71}$$

$$\sigma_t = \frac{\partial \varphi(\delta_n, \delta_t)}{\partial \delta_t} \tag{2-72}$$

Tvergaard and Hutchinson [84] have extended Needleman's work [83] on CZM to elastic-plastic materials, while Cui and Wisnom [85] presented the application of this model for materials with perfectly plastic behavior. Later, Xu and Needleman [23] applied their CZM into the finite element analysis for the first time to simulate the dynamic fracture analysis. Camacho and Ortiz [24] utilized a linear degradable CZM to study the impact damage in brittle materials. Although presented models have been utilized in earlier researches to extract the behaviour of material interface layers, they have had disadvantages such as introducing softening and numerical instability to finite element models, especially during the crack propagation steps. To overcome these problems, a rigid cohesive model was proposed by Geubelle and Baylor [86]. In their method, a high initial stiffness, known as penalty stiffness, was applied to the interface elements for an undamaged region of the material. Material behaviour and the material degradation were assessed by damage indices to reduce the initial stiffness. A bilinear traction-separation law was also employed to model the initiation and propagation of delamination in composite plates. Despite reliable results acquired by this approach, the convergence became dependent on the penalty stiffness. Considering inappropriate penalty stiffness would result in numerical instabilities, especially when the material degradation is commenced in the elements of the front region. It is also worth adding that the above mentioned models are accurate for modeling the pure fracture modes, such as mode I, mode II and mode III, however, for the mixed-mode problems such as mode I/II, some contradictory issues are raised against the fundamental basis of CZM. For instance,

because of a large process zone at the crack front for mode I (normal opening), it is not expected to observe any stress singularity. This assumption may be opposed by the mode II (tangential sliding) acting on a same plane as mode I and causes a stress concentration due to the lack of cohesive tractions on the crack surface. To overcome such a difficulty, Ortiz and Pandolfi [87] employed the concept of effective separation, δ_{eff}, and effective traction, σ_{eff}, as follows:

$$\delta_{eff} = \sqrt{\delta_n^2 + \xi^{*2}\delta_t^2} \tag{2-73}$$

$$\sigma_{eff} = \sqrt{\sigma_n^2 + \xi^{*2}\sigma_t^2} \tag{2-74}$$

where ξ^* is a dimensionless correction factor relating the crack sliding to the crack opening. These two parameters can be simply related by employing a cohesive potential function as presented in Equation (2-70). Mi et al. [88] and Alfano and Crisfield [89] improved the mixed-mode failure model's capabilities by developing a damage parameter relating the interfacial material strength to the crack relative displacements. The following damage index formulation in modeling materials degradation, progressive delamination and various other applications are presented by several researchers [25, 51, 90 and 52]:

$$\begin{cases} T = K_{Pen}\delta & \delta \le \delta_0 \quad (elastic\ part) \\ T = (1 - D_{mg})K_{Pen}\delta & \delta_0 < \delta \le \delta_f \quad (softening\ part) \\ T = 0 & \delta_f < \delta \quad (decohision\ part) \end{cases} \tag{2-75}$$

where T, D_{mg}, δ, δ_0 and δ_f are, respectively, the current effective traction/strength of interfacial material ($T = \sigma_{eff}$), the damage index, relative opening/sliding displacement, relative critical opening/sliding displacement and relative failure opening/sliding

displacement of the crack faces. The damage index for each individual failure mode can be defined as follows:

$$D_{mg} = \frac{\delta_f}{\delta}\left(\frac{\delta - \delta_0}{\delta_f - \delta_0}\right) \tag{2-76}$$

The above model assumes the element degradation happens when the crack relative displacement exceeds the critical value, δ_0, defined in terms of the penalty stiffness, K_{Pen}, and maximum interfacial strength, $T_{\max}$, as:

$$\delta_0 = \frac{T_{\max}}{K_{Pen}} \tag{2-77}$$

According to Equation (2-77), selecting an appropriate value for K_{Pen} becomes important to establish a stable rigid cohesive model. While choosing a large value for K_{Pen} may help with true estimation of the elements stiffness before the crack initiation, it will reduce the required critical relative displacement value for the crack initiation and may cause numerical instability upon the crack initiation, known as the elastic-snap back [50]. Earlier research have been undertaken to formulate the K_{Pen} based on different types of material properties. Turon et al. [50] proposed a simple relationship between the transverse modulus of elasticity, $E_{transverse}$, specimen thickness, t_{ck}, and penalty stiffness, K_{Pen}:

$$K_{Pen} = \frac{\alpha E_{transverse}}{t_{ck}} \tag{2-78}$$

where α was proposed to be equal to 50 to prevent the stiffness loss. A wide range of penalty stiffness values have been considered by other researchers for different traction-separation

laws, material properties and numerical simulation purposes. In essence, a comparison between numerical analysis and experimental result would be required to identify an optimum value for penalty stiffness in each given application.

In addition to the penalty stiffness, the length of cohesive zone is another critical factor of the CZM. As opening or sliding displacements initially increase, elements in the cohesive zone gradually reach the maximum interfacial strength. Upon this point, the element's stiffness moves into the softening region of traction-separation law and experiences irreversible degradation. The maximum length of cohesive zone occurs when the crack-tip elements are debonded completely (Figure 2-8).

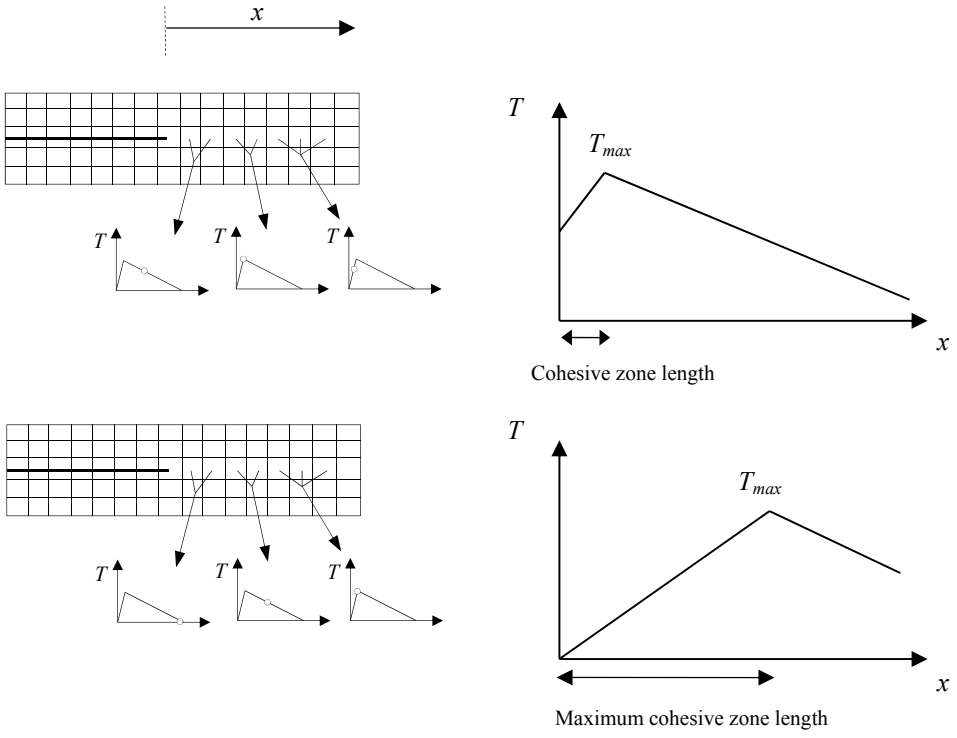

Figure 2-8 Schematic of the cohesive zone in front of crack in a given step of numerical simulation

Accordingly, choosing the correct value for the length of cohesive zone is essential in numerical modeling of delamination to prevent numerical difficulties; such as a softening problem due to the implementation of the traction-separation law instead of a conventional constitutive relationship. Earlier works have studied this topic extensively. Hillerborg et al. [22] proposed a characteristic length parameter for isotropic materials as follows:

$$l_{ch} = E_{longitudinal} \frac{G_{IC}}{T_{\max}^2} \tag{2-79}$$

where l_{ch}, G_{IC}, $E_{longitudinal}$ are the cohesive zone length, the critical energy release rate and the longitudinal Young modulus of the material, respectively. For various traction-separation laws, Planas and Elices [91] introduced a different equation for isotropic materials. However, in orthotropic materials, like FRP composite laminates, Jin and Sun [92], and Yang et al. [93] demonstrated the effect of longitudinal, transverse and shearing moduli as well as laminate thickness on the cohesive zone length. They suggested a modified formulation for measuring the cohesive zone length in the slender composite laminates as follows:

$$l_{ch} = \left(E_{transverse} \frac{G_{IC}}{T_{\max}^2} \right)^{1/4} t_{ck}^{3/4} \tag{2-80}$$

It is necessary to mention that the number of elements within the cohesive zone model is directly related to the cohesive zone length, and for realistic simulations, it is required to have a sufficient number of elements within this region. A range of different values has been proposed in earlier works [25 and 94], and it is clear that it is difficult to estimate an exact value that could work for all simulations.

2.10 Summary

In this chapter, elastic mechanical behaviour formulation of FRP composite materials was briefly described. Next, the expected failure modes for different FRP composite compositions were illustrated. General history of the fracture mechanics and damage mechanics were presented for a better understanding of subsequent steps in advanced failure modeling of FRP composite materials. Fundamentals of XFEM were introduced and its application and implementation in modeling LEFM and EPFM problems were presented. Also, CZM modeling of delamination interface was introduced and effective parameters in modeling the failure surface using this method were outlined. The following chapter will focus on implementation of principals of hybrid XFEM and CZM. It will be shown that this hybrid method will notably assist conventional FEM with numerical modeling of different fracture modes in composites.

3 Chapter: Extended Finite Element Method Implementation and Validation

In today's modern industries, numerical tools demonstrate a great capability to handle stress analysis problems with cumbersome structural shapes and material nonlinearity. Among different computational methods, FEM has gained a significant attention and is promoted with current technological and industrial needs. Numerous commercial FEM packages are available for performing advanced stress analysis for a wide range of linear and nonlinear materials. In the present research, the ABAQUS package has been implemented as it provides a large elements library as well as different material properties options for different types of analyses. It also contains different options for modeling contact surfaces and adaptive mesh analysis of structures. More importantly, a major interest of employing ABAQUS for modeling the delamination problem with XFEM was its flexibility for linking the user-element subroutines to the FEM solver [95].

In the present work, a new user-defined 3D element has been developed using Lagrangian formulation. Large deformation XFEM has been introduced to the element formulation with extended functionality to model the cohesive zone element properties (e.g., traction-separation law) and interface contact (the code has been included in the Appendix).

In the next sections, the underlying nonlinear FEM formulation and the extension of its application to XFEM modeling of CZM and interface contact in FRP composites will be discussed. The validation of the code using data updated in the literature will be presented.

Finally a set of sensitivity analysis on XFEM model parameters will be introduced for the first time.

3.1 Large Deformation Formulation

During FEM simulations, the reliability of results decreases when higher terms of deformation are neglected. Therefore, it is necessary to apply large deformation formulation in the present analysis especially as it is intended to evaluate the geometrical and constitutive material nonlinearities of FRP composites under excessive loadings.

Regardless of the state of deformation, the equilibrium between the internal forces and external forces is always established [53]:

$$\frac{\partial P_{ij}}{\partial X_i} + f_j^b = 0 \tag{3-1}$$

where P_{ij} is the nominal stress components. The above differential equation is written in the reference configuration for the Lagrangian description. Based on the above equation, one needs to apply a small or large deformation formulation via the second Piola-Kirchhoff stress and Green strain, E_{Green}, tensors, and consequently use the constitutive material properties to formulate the normal stresses. In small displacement theory, only the linear term of Green strain tensor is being utilized to calculate the second Piola-Kirchhoff tensor via appropriate constitutive relations. However, in the large displacement theory, the nonlinear portion of Green strain tensor is considered in stress calculations. The Green strain tensor can be written as follows [53]:

$$E_{Green} = E_L + E_{NL} \tag{3-2}$$

where the linear part, E_L, and the nonlinear part, E_{NL}, are defined as:

$$E_L = \begin{Bmatrix} \frac{\partial u_1}{\partial X} \\ \frac{\partial u_2}{\partial Y} \\ \frac{\partial u_3}{\partial Z} \\ \frac{\partial u_2}{\partial X} + \frac{\partial u_1}{\partial Y} \\ \frac{\partial u_3}{\partial Y} + \frac{\partial u_2}{\partial Z} \\ \frac{\partial u_1}{\partial Z} + \frac{\partial u_3}{\partial X} \end{Bmatrix} \tag{3-3}$$

$$E_{NL} = \begin{Bmatrix} \frac{1}{2}\left(\frac{\partial u_1}{\partial X}\right)^2 + \frac{1}{2}\left(\frac{\partial u_2}{\partial X}\right)^2 + \frac{1}{2}\left(\frac{\partial u_3}{\partial X}\right)^2 \\ \frac{1}{2}\left(\frac{\partial u_1}{\partial Y}\right)^2 + \frac{1}{2}\left(\frac{\partial u_2}{\partial Y}\right)^2 + \frac{1}{2}\left(\frac{\partial u_3}{\partial Y}\right)^2 \\ \frac{1}{2}\left(\frac{\partial u_1}{\partial Z}\right)^2 + \frac{1}{2}\left(\frac{\partial u_2}{\partial Z}\right)^2 + \frac{1}{2}\left(\frac{\partial u_3}{\partial Z}\right)^2 \\ \frac{\partial u_1}{\partial X}\frac{\partial u_1}{\partial Y} + \frac{\partial u_2}{\partial X}\frac{\partial u_2}{\partial Y} + \frac{\partial u_3}{\partial X}\frac{\partial u_3}{\partial Y} \\ \frac{\partial u_1}{\partial Y}\frac{\partial u_1}{\partial Z} + \frac{\partial u_2}{\partial Y}\frac{\partial u_2}{\partial Z} + \frac{\partial u_3}{\partial Y}\frac{\partial u_3}{\partial Z} \\ \frac{\partial u_1}{\partial Z}\frac{\partial u_1}{\partial X} + \frac{\partial u_2}{\partial Z}\frac{\partial u_2}{\partial X} + \frac{\partial u_3}{\partial Z}\frac{\partial u_3}{\partial X} \end{Bmatrix} \tag{3-4}$$

To implement the above equations into FEM formulation, it is required to expand the equilibrium equation using the conventional FEM weak form approach. The obtained equilibrium can be written as [53]:

$$\int_{\Gamma_V} \delta F^T P \, d\Gamma_V - \int_{\Gamma_V} \delta\left(u^k\right)^T f^b \, d\Gamma_V - \int_{\Gamma_t} \delta\left(u^k\right)^T f^t \, d\Gamma_t = 0 \tag{3-5}$$

where P and F are the nominal stress tensor and the deformation gradient respectively. Applying the standard FEM Galerkin discretization process and rewriting Equation (3-5) in terms of nodal variables and FEM shape function leads to the following equation:

$$\int_{\Gamma_V} B^T P \, d\Gamma_V - \int_{\Gamma_V} N^T f^b \, d\Gamma_V - \int_{\Gamma_t} N^T f^t \, d\Gamma_t = 0 \tag{3-6}$$

where B contains the Cartesian derivatives of the shape functions, $B_{ij} = \dfrac{\partial N_j}{\partial X_i}$.

In order to maintain the virtual work principal and to preserve the constitutive material stress-strain relationship, we need to rewrite the above equation using the second order Piola-Kirchhoff stress tensor, which is a symmetric stress tensor in contrast to the nominal stress tensor. The transformed form of Equation (3-6) can be expressed as follows [53]:

$$\overline{\Pi}(u^k) = \int_{\Gamma_V} \overline{B}^T \sigma \, d\Gamma_V - \int_{\Gamma_V} N^T f^b \, d\Gamma_V - \int_{\Gamma_t} N^T f^t \, d\Gamma_t = 0 \tag{3-7}$$

where $\overline{B}$ can be defined using the deformation gradient vector, F, as:

$$F = \begin{bmatrix} \dfrac{\partial x}{\partial X} & \dfrac{\partial y}{\partial X} & \dfrac{\partial z}{\partial X} & \dfrac{\partial x}{\partial Y} & \dfrac{\partial y}{\partial Y} & \dfrac{\partial z}{\partial Y} & \dfrac{\partial x}{\partial Z} & \dfrac{\partial y}{\partial Z} & \dfrac{\partial z}{\partial Z} \end{bmatrix} \tag{3-8}$$

$$\overline{B} = F\,B = \begin{bmatrix} \dfrac{\partial N_i}{\partial X}\dfrac{\partial x}{\partial X} & \dfrac{\partial N_i}{\partial X}\dfrac{\partial y}{\partial X} & \dfrac{\partial N_i}{\partial X}\dfrac{\partial z}{\partial X} \\ \dfrac{\partial N_i}{\partial Y}\dfrac{\partial x}{\partial Y} & \dfrac{\partial N_i}{\partial Y}\dfrac{\partial y}{\partial Y} & \dfrac{\partial N_i}{\partial Y}\dfrac{\partial z}{\partial Y} \\ \dfrac{\partial N_i}{\partial Z}\dfrac{\partial x}{\partial Z} & \dfrac{\partial N_i}{\partial Z}\dfrac{\partial y}{\partial Z} & \dfrac{\partial N_i}{\partial Z}\dfrac{\partial z}{\partial Z} \\ \dfrac{\partial N_i}{\partial Y}\dfrac{\partial x}{\partial X} + \dfrac{\partial N_i}{\partial X}\dfrac{\partial x}{\partial Y} & \dfrac{\partial N_i}{\partial Y}\dfrac{\partial y}{\partial X} + \dfrac{\partial N_i}{\partial X}\dfrac{\partial y}{\partial Y} & \dfrac{\partial N_i}{\partial Y}\dfrac{\partial z}{\partial X} + \dfrac{\partial N_i}{\partial X}\dfrac{\partial z}{\partial Y} \\ \dfrac{\partial N_i}{\partial Z}\dfrac{\partial x}{\partial Y} + \dfrac{\partial N_i}{\partial Y}\dfrac{\partial x}{\partial Z} & \dfrac{\partial N_i}{\partial Z}\dfrac{\partial y}{\partial Y} + \dfrac{\partial N_i}{\partial Y}\dfrac{\partial y}{\partial Z} & \dfrac{\partial N_i}{\partial Z}\dfrac{\partial z}{\partial Y} + \dfrac{\partial N_i}{\partial Y}\dfrac{\partial z}{\partial Z} \\ \dfrac{\partial N_i}{\partial Z}\dfrac{\partial x}{\partial X} + \dfrac{\partial N_i}{\partial X}\dfrac{\partial x}{\partial Z} & \dfrac{\partial N_i}{\partial Z}\dfrac{\partial y}{\partial X} + \dfrac{\partial N_i}{\partial X}\dfrac{\partial y}{\partial Z} & \dfrac{\partial N_i}{\partial Z}\dfrac{\partial z}{\partial X} + \dfrac{\partial N_i}{\partial X}\dfrac{\partial z}{\partial Z} \end{bmatrix} \tag{3-9}$$

The variation of the discretized FEM Galerkin method with respect to du^h is:

$$d\overline{\Pi}(u) = \int_{\Gamma_V} \overline{B}^T d\sigma \, d\Gamma_V + \int_{\Gamma_V} B^T dF \, \sigma \, d\Gamma_V = K_T \, du^h \tag{3-10}$$

where K_T is the tangential stiffness matrix. If the nodal vectors are substituted into the above equation, the tangential stiffness matrix can be formed as [53]:

$$K_T = K_{Mat} + K_{Geo} = \int_{\Gamma_V} \overline{B}^T \mathbf{C} \overline{B} \, d\Gamma_V + \int_{\Gamma_V} G_s{}^T M_s G_s \, d\Gamma_V \tag{3-11}$$

where K_{Mat}, K_{Geo}, G_S and M_S are the material and geometrical portion of tangential stiffness, shape function derivatives matrix and re-arranged second Piola-Kirchhoff stress tensor, respectively. More specifically G_S, and M_S are defined as follows.

$$G_S = \begin{bmatrix} \frac{\partial N_i}{\partial X} & 0 & 0 \\ 0 & \frac{\partial N_i}{\partial X} & 0 \\ 0 & 0 & \frac{\partial N_i}{\partial X} \\ \frac{\partial N_i}{\partial Y} & 0 & 0 \\ 0 & \frac{\partial N_i}{\partial Y} & 0 \\ 0 & 0 & \frac{\partial N_i}{\partial Y} \\ \frac{\partial N_i}{\partial Z} & 0 & 0 \\ 0 & \frac{\partial N_i}{\partial Z} & 0 \\ 0 & 0 & \frac{\partial N_i}{\partial Z} \end{bmatrix} \tag{3-12}$$

$$M_S = \begin{bmatrix} \sigma_{11} I_{3\times3} & \sigma_{12} I_{3\times3} & \sigma_{13} I_{3\times3} \\ & \sigma_{22} I_{3\times3} & \sigma_{23} I_{3\times3} \\ sym. & & \sigma_{33} I_{3\times3} \end{bmatrix} \tag{3-13}$$

where $I_{3\times3}$ is the unity matrix in the three dimensional domain.

In the final loading step, based on the total nodal displacement, the Cauchy stress tensor, σ', is calculated by transforming the second order Piola-Kirchhoff stress tensor [53]:

$$\sigma' = \frac{F\sigma F^T}{\det(F)} \tag{3-14}$$

3.2 Nonlinear Solvers

The nonlinear analysis of structures normally requires an iterative solver to find nodal variables under the equilibrium condition in each step. In nonlinear FEM, purely incremental, known as explicit, and predictive/corrective, known as implicit, solvers have frequently been employed in the literature [96]. The first assumption in both solvers is the equilibrium of acting forces on the body. Thus, one can write the equilibrium of the body according to the internal forces, F_{int}, and the external loads, F_{ext}:

$$F_{\text{int}} - F_{ext} = 0 \tag{3-15}$$

In a case where the structure's response is nonlinear, simply solving the first order linear equation will not satisfy Equation (3-15). The difference appearing in a nonlinear FEM between external loads and internal forces called residual forces, Rs_i, in the i^{th} loading step. Accordingly, Equation (3-15) is rewritten in the following format:

$$F_{ext} - F_{\text{int}} = Rs_i \tag{3-16}$$

In Figure 3-1, the relationship between internal forces, external forces and residual forces are depicted.

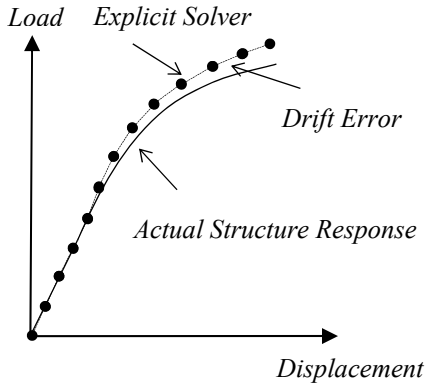

Figure 3-1 Explicit solver approach and possible drift error in nonlinear problems (dots show numerical solution steps) [96]

These residual forces correspond to the new structural configuration after experiencing the external load. In purely incremental/explicit solvers, no corrective procedure is applied to diminish the residuals. Hence, in such methods, small increments of external loading should be imposed to the structure to ensure the residual forces in each numerical step remain within an acceptance tolerance [96].

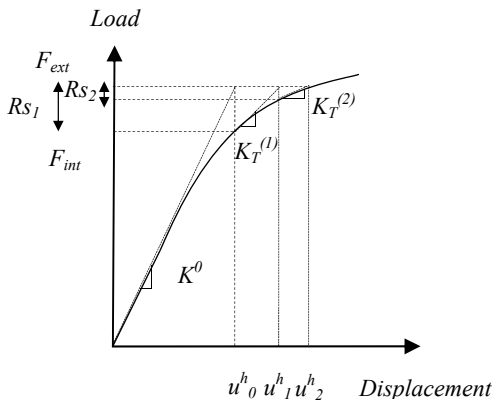

Figure 3-2 Newton-Raphson iterative solver approach in nonlinear FEM problems [96]

On the other hand, in corrective/implicit solvers, the residual forces are moderated with an iterative correction method such as the Newton-Raphson or Quasi Newton-Raphson methods. In such solvers, the structure's tangent stiffness, K_T, needs to be evaluated in each iteration to extract the displacement correction due to residual forces, which can be derived from the Taylor series as follows:

$$Rs_{i+1}(u^h_{i+1}) = Rs_i(u^h_i) + \frac{\partial Rs_i(u^h_i)}{\partial u^h}(u^h_{i+1} - u^h_i) \tag{3-17}$$

$\frac{\partial Rs_i(u^h_{i+1})}{\partial u^h}$ is the Jacobian Matrix presuming that:

$$K_T = \frac{\partial Rs_i}{\partial u^h} = \frac{\partial(F_{ext} - F_{\text{int}})}{\partial u^h} \tag{3-18}$$

Using Equation (3-17), displacement correction can be implemented by solving the following equation in each iteration.

$$K_T^{(i)} \Delta u^h_i = Rs_i \tag{3-19}$$

After the i^{th} iteration, the total displacement is the summation of previous iterations and the new residual forces. Tangent stiffness should be evaluated using the updated displacement (Figure 3-2).

$$u_i^h = u_{i-1}^h + \Delta u_i^h \tag{3-20}$$

In terms of convergence criteria, the iterative solver in ABAQUS stops the iteration steps based on two criteria. In the first one, if the residual forces can be negligible at every single degree of freedom in comparison to an overall residual force tolerance, external loads and internal forces are considered to be in equilibrium. The overall tolerance value can be set depending on the user's demand, and if it remains intact, ABAQUS assumes 0.5% of the average force in the entire structure at the given time step. Another threshold for accepting the solution is based on the last displacement correction. The last correction should be relatively smaller than the fraction of the total incremental displacement (1% by default); otherwise, ABAQUS performs another iteration step [96].

3.3 Modeling Contact on Material Interfaces Using XFEM

In recent investigations, Khoei et al. [53] introduced a new modeling technique to simulate nonlinear 3D contact problems using the large deformation formula and XFEM. The proposed tangential stiffness matrix (merely for the interface material) based on nonlinear XFEM was defined as:

$$K_T = K_{Mat} + K_{Geo} = \int_{\Gamma_V} \overline{B}^T D_S^{ep} \overline{B}\ d\Gamma_V + \int_{\Gamma_V} {G_s}^T M_S G_s\ d\Gamma_V \tag{3-21}$$

where $\overline{B}$ and G_s have an enriched part added to the conventional FEM part of nodal vectors and D_S^{ep} is the elastic-plastic constitutive matrix. These matrices can be redefined as follows:

$$\overline{B} = \left[\overline{B}^{u^{ord}} \;\; \overline{B}^{b^H} \right] \tag{3-22}$$

$$G_s = \left[G_s^{u^{ord}} \;\; G_s^{b^H} \right] \tag{3-23}$$

where $\overline{B}^{b^H}$ and $G_s^{b^H}$ are defined as (H is the Heaviside function):

$$\overline{B}^{b^H} = \begin{bmatrix} \frac{\partial(N_i H)}{\partial X}\frac{\partial x}{\partial X} & \frac{\partial(N_i H)}{\partial X}\frac{\partial y}{\partial X} & \frac{\partial(N_i H)}{\partial X}\frac{\partial z}{\partial X} \\ \frac{\partial(N_i H)}{\partial Y}\frac{\partial x}{\partial Y} & \frac{\partial(N_i H)}{\partial Y}\frac{\partial y}{\partial Y} & \frac{\partial(N_i H)}{\partial Y}\frac{\partial z}{\partial Y} \\ \frac{\partial(N_i H)}{\partial Z}\frac{\partial x}{\partial Z} & \frac{\partial(N_i H)}{\partial Z}\frac{\partial y}{\partial Z} & \frac{\partial(N_i H)}{\partial Z}\frac{\partial z}{\partial Z} \\ \frac{\partial(N_i H)}{\partial Y}\frac{\partial x}{\partial X} + \frac{\partial(N_i H)}{\partial X}\frac{\partial x}{\partial Y} & \frac{\partial(N_i H)}{\partial Y}\frac{\partial y}{\partial X} + \frac{\partial(N_i H)}{\partial X}\frac{\partial y}{\partial Y} & \frac{\partial(N_i H)}{\partial Y}\frac{\partial z}{\partial X} + \frac{\partial(N_i H)}{\partial X}\frac{\partial z}{\partial Y} \\ \frac{\partial(N_i H)}{\partial Z}\frac{\partial x}{\partial Y} + \frac{\partial(N_i H)}{\partial Y}\frac{\partial x}{\partial Z} & \frac{\partial(N_i H)}{\partial Z}\frac{\partial y}{\partial Y} + \frac{\partial(N_i H)}{\partial Y}\frac{\partial y}{\partial Z} & \frac{\partial(N_i H)}{\partial Z}\frac{\partial z}{\partial Y} + \frac{\partial(N_i H)}{\partial Y}\frac{\partial z}{\partial Z} \\ \frac{\partial(N_i H)}{\partial Z}\frac{\partial x}{\partial X} + \frac{\partial(N_i H)}{\partial X}\frac{\partial x}{\partial Z} & \frac{\partial(N_i H)}{\partial Z}\frac{\partial y}{\partial X} + \frac{\partial(N_i H)}{\partial X}\frac{\partial y}{\partial Z} & \frac{\partial(N_i H)}{\partial Z}\frac{\partial z}{\partial X} + \frac{\partial(N_i H)}{\partial X}\frac{\partial z}{\partial Z} \end{bmatrix} \tag{3-24}$$

$$G_s^{b^H} = \begin{bmatrix} \frac{\partial(N_i H)}{\partial X} & 0 & 0 \\ 0 & \frac{\partial(N_i H)}{\partial X} & 0 \\ 0 & 0 & \frac{\partial(N_i H)}{\partial X} \\ \frac{\partial(N_i H)}{\partial Y} & 0 & 0 \\ 0 & \frac{\partial(N_i H)}{\partial Y} & 0 \\ 0 & 0 & \frac{\partial(N_i H)}{\partial Y} \\ \frac{\partial(N_i H)}{\partial Z} & 0 & 0 \\ 0 & \frac{\partial(N_i H)}{\partial Z} & 0 \\ 0 & 0 & \frac{\partial(N_i H)}{\partial Z} \end{bmatrix} \tag{3-25}$$

As mentioned before, to satisfy the PUM fundamentals, the Heaviside function should be deducted by Heaviside value at each element's node. The elastic-plastic constitutive matrix is defined as:

$$D_S^{ep} = \begin{bmatrix} \overline{K}_{11} & 0 & 0 \\ 0 & \overline{K}_{22} & 0 \\ 0 & 0 & \overline{K}_{33} \end{bmatrix} \tag{3-26}$$

where $\overline{K}_{ii}$ is the penalty (contact) stiffness assigned to the local coordinates of the contact surface. $\overline{K}_{11}$ provides the impenetrable characteristic to the normal direction of the contact plane which follows the Kuhn-Tucker thresholds [73]:

$$\delta_n \geq 0,\ P_{Contact} \leq 0,\ (\delta_n) \times (P_{Contact}) = 0 \tag{3-27}$$

where $P_{Contact}$ contains the vector of contact forces, respectively.

The remaining terms in the elastic-plastic constitutive matrix, $\overline{K}_{22}$ and $\overline{K}_{33}$, create the friction forces and prevent the contact surfaces from abrupt sliding. For these terms, standard static and dynamic friction laws can be applied to perform the analysis [53].

3.4 Implementation of the Cohesive Zone Model

As described in Section 2.9, depending on the FRP composite material lay-up, we may expect to observe a large processing zone during decohesion. Hence, it is required to apply the cohesive crack modeling into the XFEM analysis. For this purpose, a bilinear traction-separation law is utilized instead of the conventional constitutive relationship for the interface material to embed cohesive behaviour into the crack-tip region by means of re-arranging the nodal displacement components [35]. They also implemented a cohesive/contact transformation matrix ($\overline{B}_{Coh}$) to re-arrange the nodal degrees of freedom and rewrote crack opening and sliding displacements and tractions on crack faces as follows:

$$\delta = \overline{B}_{Coh}\, u^{k} \tag{3-28}$$

$$T = \overline{D}_{Interface}\, \delta \tag{3-29}$$

where $\overline{D}_{Interface}$ includes the cohesive interface material properties as described in Equation (2-74). As proposed by Geubelle and Baylor [86], a rigid cohesive zone model is implemented to simulate the crack initiation. This model applies an initial rigid stiffness in enriched elements before damage initiation and provides a good interpretation of material deterioration while the relative crack displacement reaches the failure limit. Also, the application of this model with XFEM improves numerical simulations consistency and

reduces difficulties such as snap-back and results fluctuation which are mostly caused by the reduction of stiffness in fully damaged elements to zero [28].

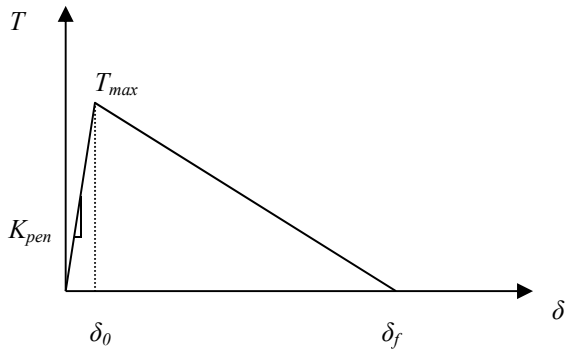

Figure 3-3 Bilinear traction-separation law for modeling the material degradation

The cohesive/contact transformation matrix can be extracted by finding the displacement in an enriched element. The displacement vector of any point in the enriched element, $u^g(x)$, is:

$$u^g(x) = \sum_i \left(N_i u_i^{ord}\right) + \sum_j \left(N_j \left(\sum_k N_k H_k - H_j \right) b_j^H \right) = \begin{bmatrix} N & 0 \\ 0 & N^{enr} \end{bmatrix} \begin{bmatrix} u^{ord} \\ b^H \end{bmatrix} \tag{3-30}$$

where,

$$N_j^{enr} = N_j \left(\sum_k N_k H_k - H_j \right) \tag{3-31}$$

The conventional FE shape function's value remains constant for different points in the enriched element while the enriched shape function's value demonstrates an odd function property with respect to the interface position:

$$N^{enr}(bottom) = -N^{enr}(top) \tag{3-32}$$

Thus, the global relative crack displacement, $\overline{\delta}$, can be described in the form of the displacement difference between two points above and beneath the crack surface.

$$\overline{\delta} = u^k(top) - u^k(bottom) = \begin{bmatrix} N & N^{enr} \end{bmatrix} \begin{bmatrix} u^{ord} \\ b^H \end{bmatrix} - \begin{bmatrix} N & -N^{enr} \end{bmatrix} \begin{bmatrix} u^{ord} \\ b^H \end{bmatrix} \tag{3-33}$$

$$\overline{\delta} = 2 \begin{bmatrix} 0 & N^{enr} \end{bmatrix} \begin{bmatrix} u^{ord} \\ b^H \end{bmatrix} \tag{3-34}$$

In order to find the relative crack displacements in a global coordinate system, a simple transformation based on the normal and tangential directions, m_{ij}, of the crack plane with respect to the global coordinate can be employed:

$$\delta = \begin{bmatrix} m_{11} & m_{12} & m_{13} \\ m_{21} & m_{22} & m_{23} \\ m_{31} & m_{32} & m_{33} \end{bmatrix} \begin{bmatrix} \overline{\delta}_X \\ \overline{\delta}_Y \\ \overline{\delta}_Z \end{bmatrix} = 2 \begin{bmatrix} m_{11} & m_{12} & m_{13} \\ m_{21} & m_{22} & m_{23} \\ m_{31} & m_{32} & m_{33} \end{bmatrix} \begin{bmatrix} 0 & N^{enr} \end{bmatrix} \begin{bmatrix} u^{ord} \\ b^H \end{bmatrix} = \overline{B}_{Coh} u^k \tag{3-35}$$

Consequently, Equation (3-35) can be substituted into Equation (3-29) and used in the tangential stiffness formulation to introduce process zone properties within enriched elements (also compare to Equation 3-21):

$$\begin{aligned} K_T &= K_{Mat} + K_{Geo} + K_{Coh} = \int_{\Gamma_V} \overline{B}^T D_S^{ep} \overline{B} \, d\Gamma_V + \int_{\Gamma_V} G^T M_S G \, d\Gamma_V \\ &+ \int_{\Gamma_c} (\overline{B}_{Coh})^T \overline{D}_{Interface} \overline{B}_{Coh} \, d\Gamma_c \end{aligned} \tag{3-36}$$

Finally, in order to evaluate the internal forces, one can simply employ the Equation (3-37) as follows:

$$F_{\text{int}} = \int_{\Gamma_V} \overline{B}^T \sigma \, d\Gamma_V + \int_{\Gamma_C} N^{enr^T} f^t \, d\Gamma_C \tag{3-37}$$

3.5 Other Numerical Implementation Details

The numerical implementation of the presented approach not only requires good understanding of the conventional FEM, but also entails the nodal selection for the enriched, enhanced approach for numerical integration over a discontinuous field and contact bound approximation which will be described in the next sub-sections.

3.5.1 Node Selection for Enrichment

In order to differentiate between ordinary and enriched nodes, all elements have to undergo selection criteria known as the level-set technique. In the first step, the distance of each node from the crack face should be determined. Then, in each element, nodal distance values should be compared. Any cracked element would contain a node with a positive distance value and a negative one. The following relationship interprets the first selection criterion for the cracked elements:

$$\varphi_{1\max}(element) \times \varphi_{1\min}(element) < 0 \tag{3-38}$$

where φ_1 is the element nodal distance value from the crack face and is defined as:

$$\varphi_1(X^*) = \left(X_1^* - X_1\right)n_1 + \left(Y_1^* - Y_1\right)n_2 + \left(Z_1^* - Z_1\right)n_3 \tag{3-39}$$

In Equation (3-39), (X_1^*, Y_1^*, Z_1^*) and (X_1, Y_1, Z_1) are the element's node coordinates and arbitrary point coordinates on the crack surface. In the second step, the boundary of the cracked element should be identified using another level-set technique. Instead of the crack surface, the nodal distance from the edges of the crack plane is calculated and nodes enclosed by all edges are considered. The selection criterion can be demonstrated as follows:

$$\psi_{1\min}(element) < 0 \tag{3-40}$$

where ψ_1 is equal to the element nodal distance from the edges of the crack plane defined as:

$$\psi_1(X^*) = \left(X_1^* - X_2\right)(n_2^t n_3 - n_3^t n_2) + \left(Y_1^* - Y_2\right)(n_3^t n_1 - n_1^t n_3) + \left(Z_1^* - Z_2\right)(n_2^t n_1 - n_1^t n_2) \tag{3-41}$$

In Equation (3-41), (X_1, Y_1, Z_1) is an arbitrary point coordinate on the crack edge and (n_1^t, n_2^t, n_3^t) is the unit vector of the crack edge. As an example, in Figures 3-4 and 3-5, a meshed object was analyzed using the above mentioned level-set techniques with a crack plane situated in the middle layer of the mesh. These figures depict the level-set variables φ_1 and ψ_1, and the resulting enriched nodes as shown in Figure 3-6.

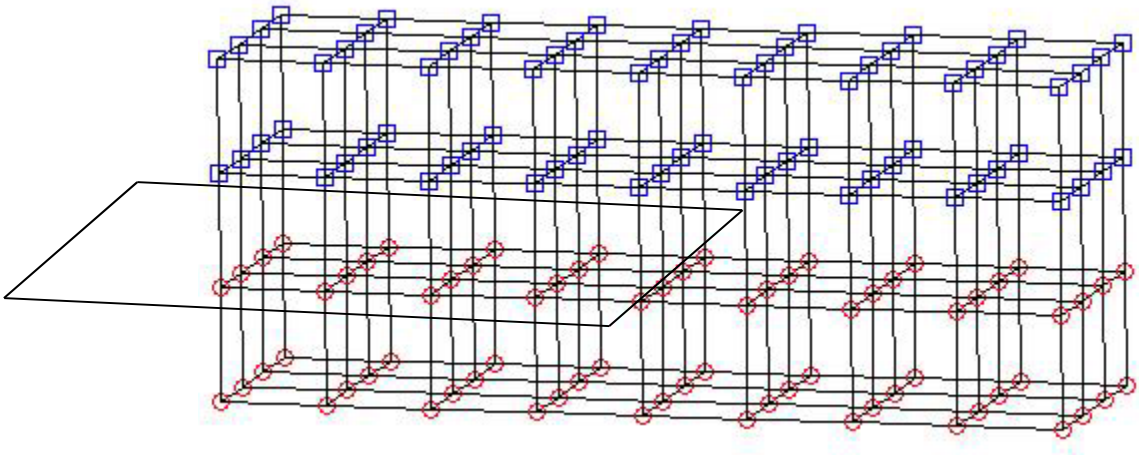

Figure 3-4 Variation of φ_1 values in an example meshed object (square represents the positive value and circle denotes the negative value; the rectangle shows the crack plane)

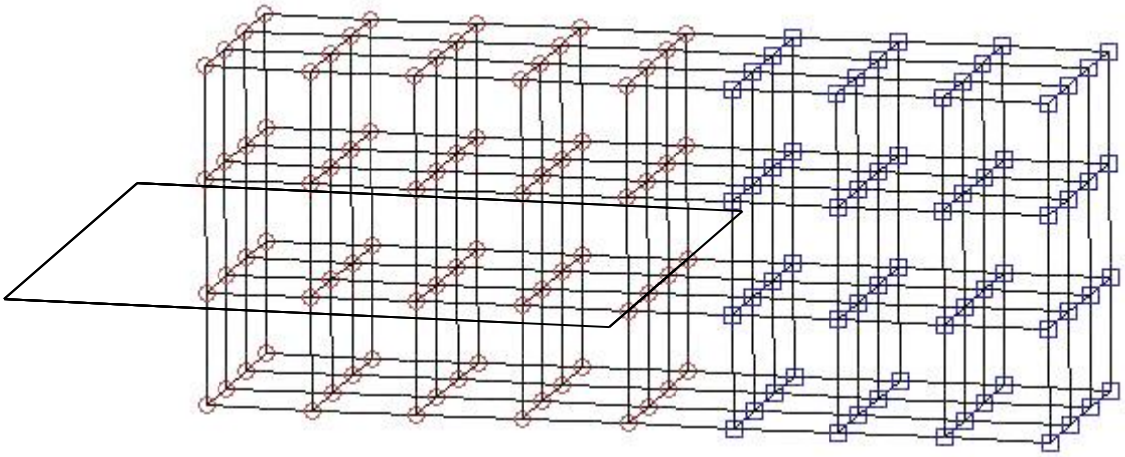

Figure 3-5 Variation of ψ_1 values for the front edge of the crack plane in the example meshed object (square represents the positive value and circle denotes the negative value)

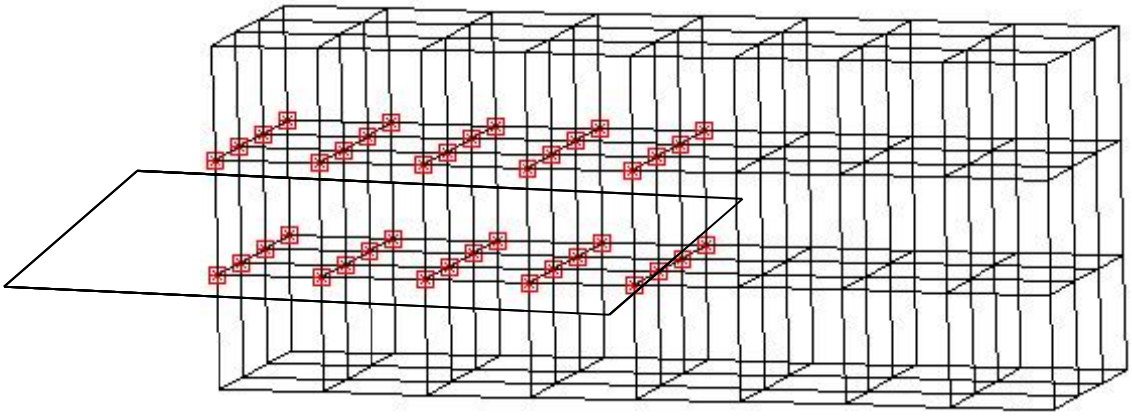

Figure 3-6 Accepted nodes in the example meshed object based on Equations (3-39) and (3-41) of level-set criteria

3.5.2 Numerical Integration of Discontinuous Fields

In order to obtain a weak form integration formulation (for FEM) for the stiffness and force matrices, numerical integration should be performed on discretized elements. Methods such

as Gauss quadrature and Simpson's rule are well-known for their applications in numerical computations and provide accurate results in continuous fields. On the other hand, employing such numerical integration methods on discontinuous fields will not suffice and lead to pivot points in the corresponding equations' system. Therefore, to prevent such problems from being introduced into fracture problems through cracked elements, auxiliary sub-triangles should be employed to discretize discontinuous material domains. Then, a numerical integration scheme can be utilized to evaluate the integration over each sub-triangle and consequently over the cracked element (Figure 3-7). For 3D models, a similar approach can be applied and sub-tetrahedral elements replace the sub-triangles in order to deliver sufficient integration points in discontinuous fields (Figure 3-8).

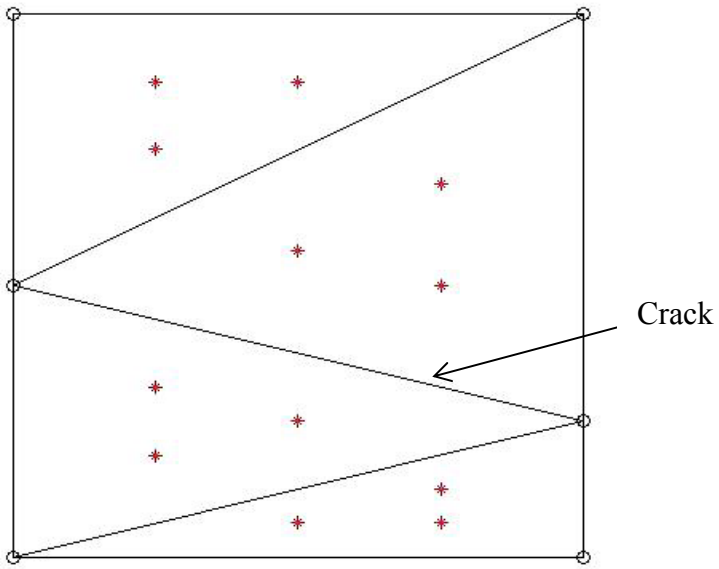

Figure 3-7 Sub-triangles of a 2D element with third order Gauss quadrature

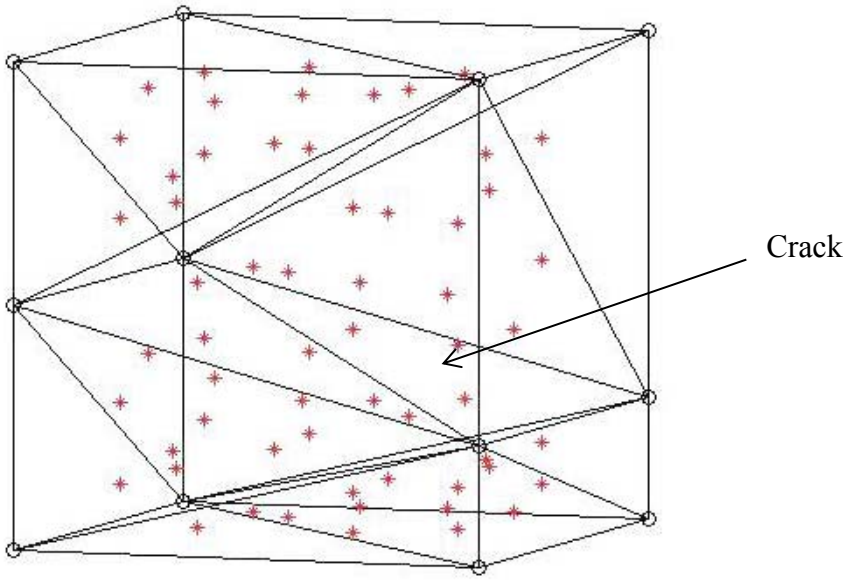

Figure 3-8 Sub-tetrahedrals of a 3D element with third order Gauss quadrature

The numerical integration of a discontinuous field with subdivided elements is similar but not identical to the continuous case. For instance, the numerical integration of an arbitrary continuous function, $f_1(X,Y,Z)$, over a single element can be summarized as:

$$\iiint_{\Omega_e} f_1(X,Y,Z)\,d\Omega = V_e \sum_{i=1}^{n_G} w^g{}_i f_1(\xi_1^i,\xi_2^i,\xi_3^i) + error \tag{3-42}$$

where V_e is the element volume, Ω_e is the element domain; n_G, w^g and (ξ_1, ξ_2, ξ_3) are the Gauss quadrature order, points weights and local coordinates, respectively.

In order to adapt the above formulation to a discontinuous function, $f_1'(X,Y,Z)$, the following modification should be considered:

$$\iiint_{\Omega_e} f'(X,Y,Z)\,d\Omega = V_e \sum_{j=1}^{m_{poly}} \sum_{i=1}^{n_G} w^p{}_j w^g{}_i f'(\xi_1^i,\xi_2^i,\xi_3^i) + error \tag{3-43}$$

where m_{poly} is the number of sub-polygons and w^p is the modification factor for the weight of each sub-polygon, which can be evaluated by the ratio of each sub-polygon volume, V^*, over the element volume:

$$w^p{}_j = \frac{V_j^*}{V_e} \tag{3-44}$$

3.5.3 Implementation of the Integration Bound Approach

Another numerical aspect of the interface contact and cohesive zone model simulation with XFEM is the integration (contact) bound. Application of the integration bound in the vicinity of the interface can eliminate the need for defining new integration points in the interface surface and decrease the computational time. It also prevents the elastic-plastic relationship to be mistakenly introduced to the integration points which are far from the interface. Despite the advantage of this method with regular sub-element methods, the contact bound dimension is not explicit and one should perform sensitivity analyses to obtain an optimum value in a given application. In Figure 3-9, integration points in the entire elements and sub-elements and within the integration bound is illustrated by red stars and blue dots.

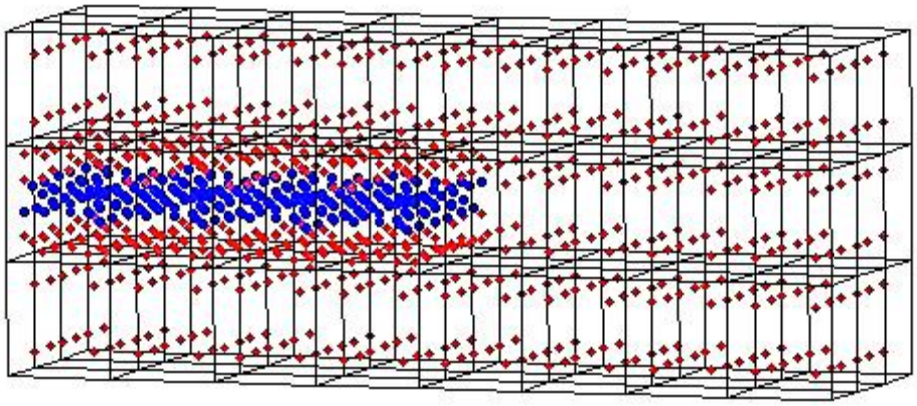

Figure 3-9 Integration points of a meshed object with enriched elements (red stars are integration points and blue dots are integration points within the integration bound)

3.5.4 Simulation Algorithm

A MATLAB code in concert with ABAQUS was implemented to perform the simulations. In the first step, MATLAB code reads the nodes coordinates, connectivity tables, material mechanical properties, crack surface and fracture information from a user defined data file (*.DAT). Using the level set technique, described in Section 3.4, the MATLAB code recognizes the ordinary elements and enriched elements of the model. It then assembles an input file for ABAQUS execution. ABAQUS utilizes the developed user element subroutine (UEL) along with generated input file (*.INP) to run the model and write the stress, strain and displacement fields in the results file. At this stage, MATLAB code reads these fields from the latter file and calculates the energy release rate using the *J*-integral to evaluate the stability of the delamination. If the delamination is unstable, MATLAB re-writes a new input file with extended delamination, otherwise, it only increases the grip opening displacement (with no delamination progression). The iterative procedure continues until the maximum number of steps (defined by the user prior to simulation) is reached. This number should be large enough

to capture the response of the structure accurately, while being not too large to make the simulations excessively costly; in the present simulation cases it varied between 500 to 1000 steps. The summary of the above implementation procedure is shown as a flow-diagram in Figure 3-10.

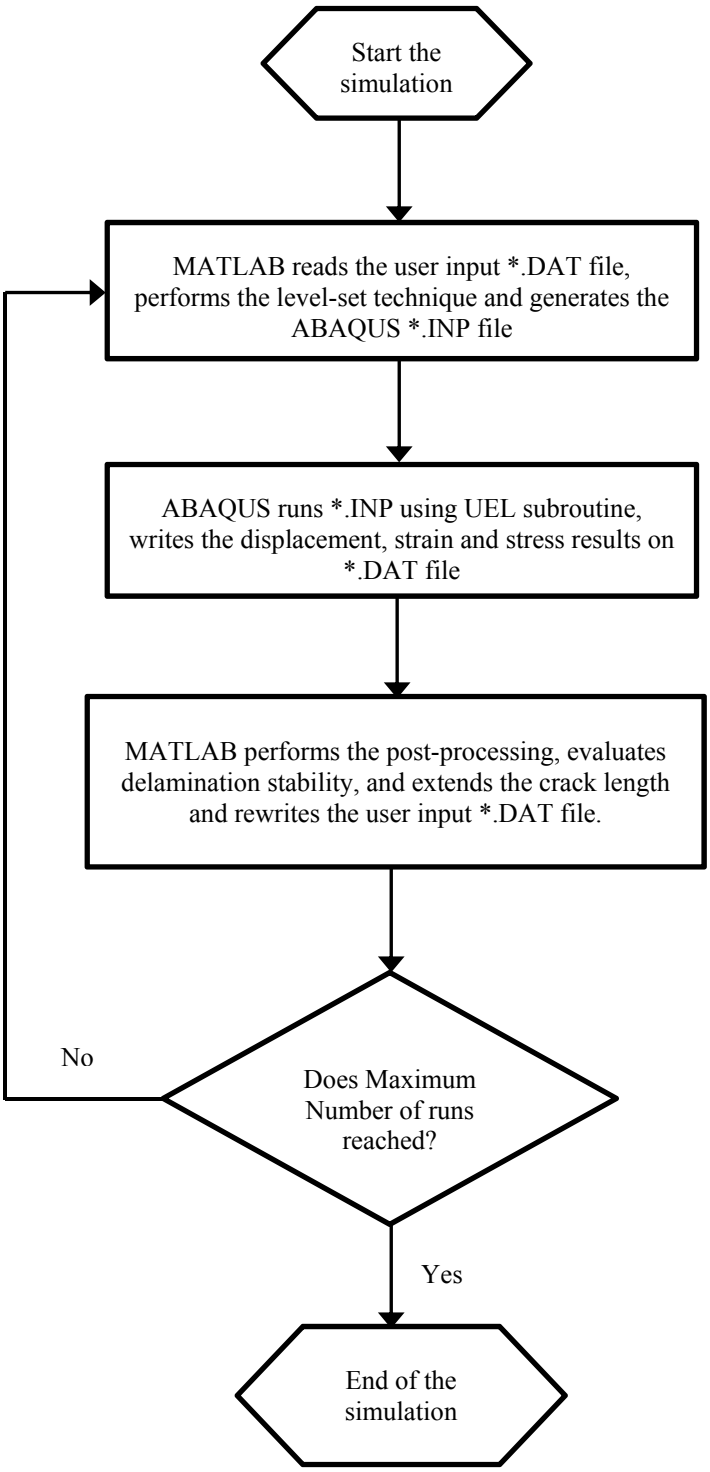

Figure 3-10 MATLAB-ABAQUS simulation algorithm employed for modeling the delamination

3.6 Numerical Examples of Mode I and II Fracture Tests: Validation of XFEM Code

In the next sections, several benchmark examples are numerically simulated using the new XFEM framework presented in the previous sections and the ABAQUS user-defined subroutine provided in the Appendix. These examples are well described in the literature and other researchers have similarly performed numerical modeling and experimental tests to verify their proposed approaches and codes as addressed below.

3.6.1 Numerical Simulation of the DCB Tests

The Double Cantilever Beam (DCB) is one of the standard tests to evaluate the mode I interlaminar fracture energy toughness and damage properties of materials. DCB samples are mainly fabricated based on the ASTM D5528-01 [97]. Composite materials considered in this example are T300/977-2 carbon fiber-reinforced epoxy and AS4/PEEK carbon fiber-reinforced poly ether ether ketone, which are widely used in the aerospace industries to manufacture airframe structures and to replace steel components especially when a high service temperature is required [52]. The T300/977-2 models had a 150 mm length, 20 mm width, and 1.98 mm thickness for each arm with 55 mm initial crack (Figure 3-11). For AS4/PEEK, model dimensions were 102 mm long, 25.4 mm wide and 1.56 mm thick for each arm, with a 32.9 mm initial crack. The material properties for each specimen are given in Table 3-1 [52].

Table 3-1 Mechanical properties of T300/977-2 and AS4/PEEK samples [52]

T300/977-2		AS4/PEEK	
Elastic Properties	**Fracture Properties**	**Elastic Properties**	**Fracture Properties**
E_{11} = 150 GPa	T_{max} = 45 MPa	E_{11} = 122.7 GPa	T_{max} = 80 MPa
$E_{22} = E_{33}$ = 11 GPa	G_{IC} = 268 J/m^2	$E_{22} = E_{33}$ = 10.1 GPa	G_{IC} = 969 J/m^2
$G_{12} = G_{13}$= 6 GPa		$G_{12} = G_{13}$ = 5.5 GPa	
G_{23} = 3 GPa		G_{23} = 2.2 GPa	
$\nu_{12} = \nu_{13}$ = 0.25		$\nu_{12} = \nu_{13}$ = 0.25	
ν_{23} = 0.5		ν_{23} = 0.48	

Previous works on both types of above composite samples have been reported using a cohesive interface layer method via the conventional FEM as well as the mesh-free method by Camanho et al. [25], Turon et al. [50], Barbieri and Meo [52]. In the present study, effects of different important modeling variables such as the interface stiffness (e.g., the penalty factor) and the cohesive region length are assessed via the XFEM model. Results (in the following sub-sections) are compared to the previous standard numerical approaches to provide further understanding of the advantages of the XFEM method in terms of numerical accuracy and stability.

3.6.1.1 Effects of Different Modeling Approaches

Turon et al. [50] investigated the effective cohesive zone length for T300/977-2 specimens. They suggested a cohesive zone length of 0.9 mm from numerical simulations on a very fine mesh (with element length, l_e, of 0.125 mm). Based on their work, the size of elements in the cohesive zone region should not exceed 0.5 mm, and a minimum of two elements are required in this region for acceptable modeling results. In Figure 3-11, the present XFEM global force-

displacement (F-Δ) results with the fine mesh simulation with the CZM penalty stiffness (K_{pen}) of 1×10^6 N/mm^3 and the cohesive zone length of 1.5 mm are compared to the results from Camanho et al. [25], Turon et al. [50], Barbieri and Meo [52] by means of different numerical approaches.

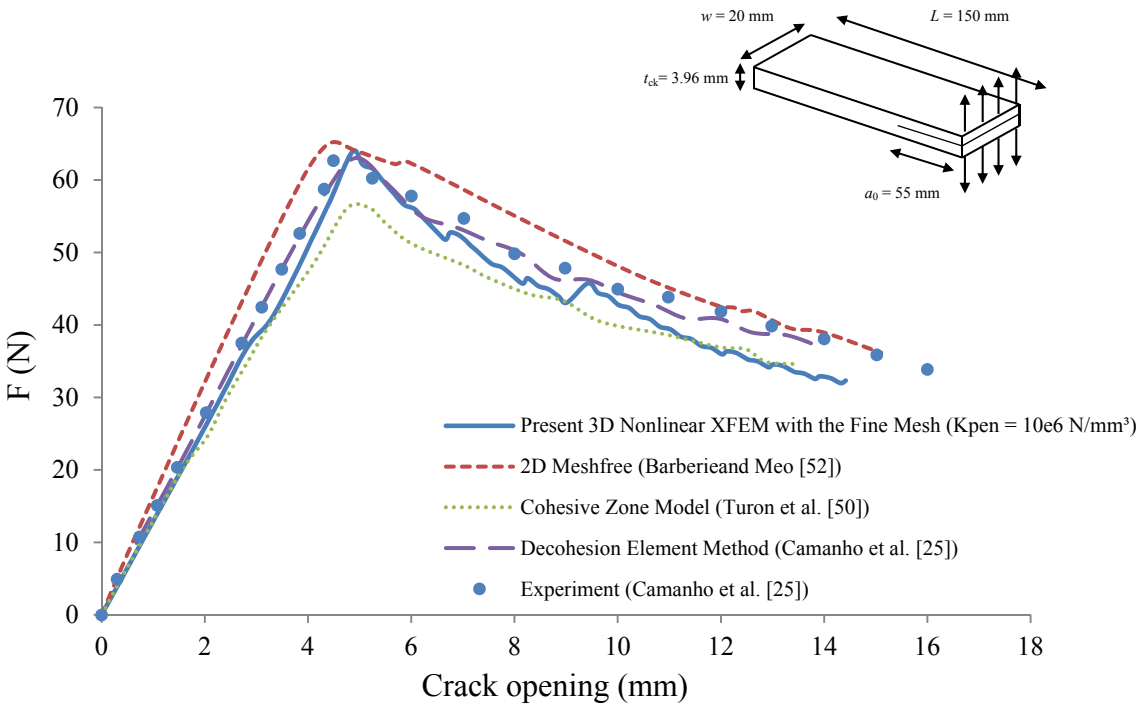

Figure 3-11 A comparison between DCB test results via different methods on T300/977-2 samples

Figure 3-11 shows that all models predict a similar trend of load-displacement during delamination of the sample. The mesh-free method [52] overestimates the stiffness of the material and leads to raising the peak opening force by 5%, while the Turon et al. [50] cohesive finite element approach underestimates the resisting force by 10% in comparison to the experimental data obtained by Camanho et al. [25]. The XFEM estimates the peak opening force with 3% difference from the experiment and, similar to Camanho et al. [25], it provides a more conservative estimation of the fracture behavior of the DCB samples.

3.6.1.2 Effects of Mesh Size and Cohesive Zone Length

DCB tests of T300/977-2 specimens were simulated using two different mesh sizes, namely element lengths of 0.4 mm and 1.25 mm, to demonstrate the effect of coarse and fine mesh on the XFEM results. In addition, in order to illustrate the influence of cohesive zone length in each case, XFEM simulations were re-run (Figures 3-12 and 3-13) with different l_{ch} values and the fixed penalty stiffness of 1×10^6 N/mm^3 [50].

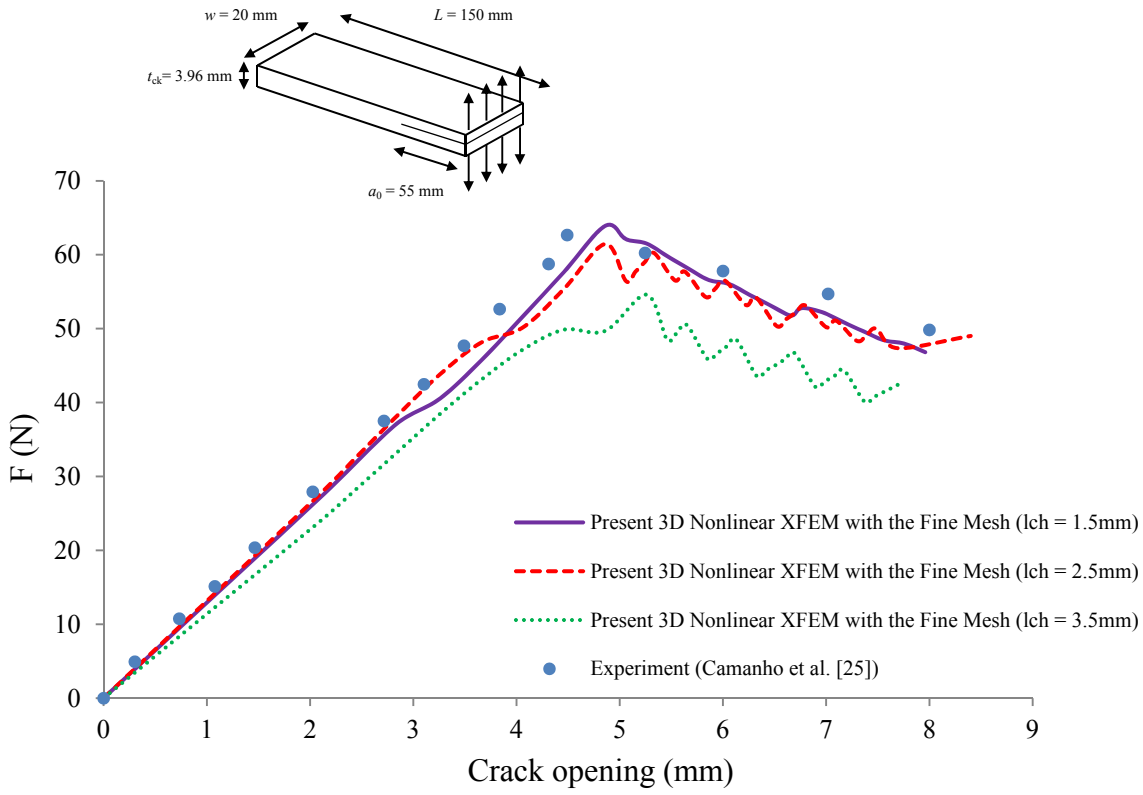

Figure 3-12 Load-Displacement DCB test results for the fine mesh (l_e = 0.4 mm) simulation with different cohesive zone lengths for T300/977-2 samples

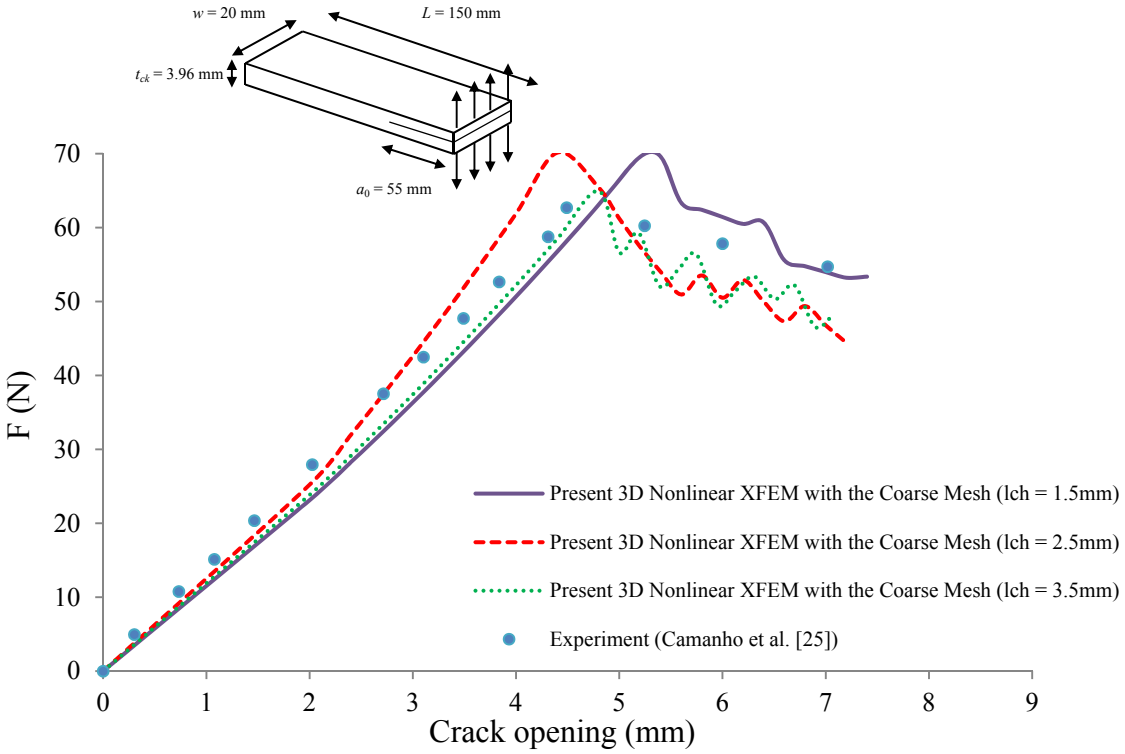

Figure 3-13 Load-Displacement DCB test results for the coarse mesh (l_e = 1.25 mm) simulation with different cohesive zone lengths for T300/977-2 samples

Recalling Figure 3-12, in the fine mesh (l_e = 0.4 mm) model, it is observed that using 3 (l_{ch} = 1.5 mm) to 6 (l_{ch} = 2.5 mm) elements within the cohesive zone would lead to an accurate estimation of the experimental data, while increasing this critical value to 8 (l_{ch} = 3.5 mm) elements would introduce an unrealistic global softening behavior to the model. In the coarse mesh (l_e = 1.25 mm) runs (Figure 3-13), only in the case with 3 (l_{ch} = 3.5 mm) elements the simulation result became relatively agreeable with the experimental values. It is worth adding that in an earlier work by Harper and Hallett [51], they had also obtained load-displacement results using different mesh sizes in the interface elements. Namely, for smoother numerical results, they decreased the elements size to prevent the dynamic effects of larger elements failure such as a sudden drop of the fracture energy release rate. They also introduced a global damping factor of 5% into the simulations to dissipate the oscillation caused by the cohesive element debonding and the loss of stiffness in each step of crack propagation. In the present study, the enriched elements in the cohesive zone have the aggregation of stiffness from XFEM approximation and the traction-separation law. Hence, when complete debonding occurs, the affected elements' stiffness does not completely disappear by elimination of the cohesive zone stiffness, and the XFEM approximation can inherently prevent the oscillations to a certain degree, without adapting a damping ratio into the model. This can be especially beneficial regarding computational time in the case of explicit analysis.

3.6.1.3 Effects of Different Penalty Stiffness Factors

As discussed in Section 3.4, the accuracy of the bilinear traction-separation law in modeling the process zone is directly dependent on the penalty stiffness value, whose optimum value may change from one material or fracture mode to another. In this section, in order to evaluate

the accuracy of XFEM predictions against different penalty stiffness values, a set of simulations with fine mesh were performed with a wide range of penalty stiffnesses, varying from 10^2 N/mm^3 to 10^5 N/mm^3, and a similar cohesive zone length (l_{ch} = 2.5 mm). Results were compared to the experimental data for both T300/977-2 and AS4/PEEK specimens, respectively (Figures 3-14 and 3-15).

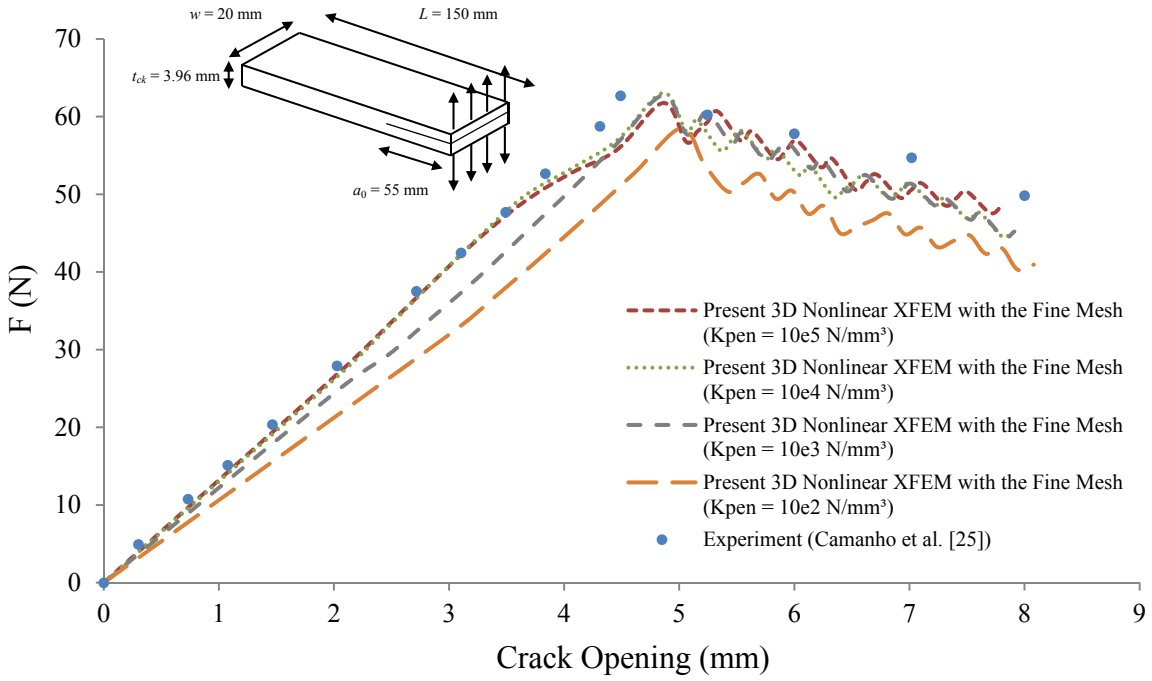

Figure 3-14 The comparison between DCB test load-displacement results of T300/977-2 samples with different penalty stiffnesses

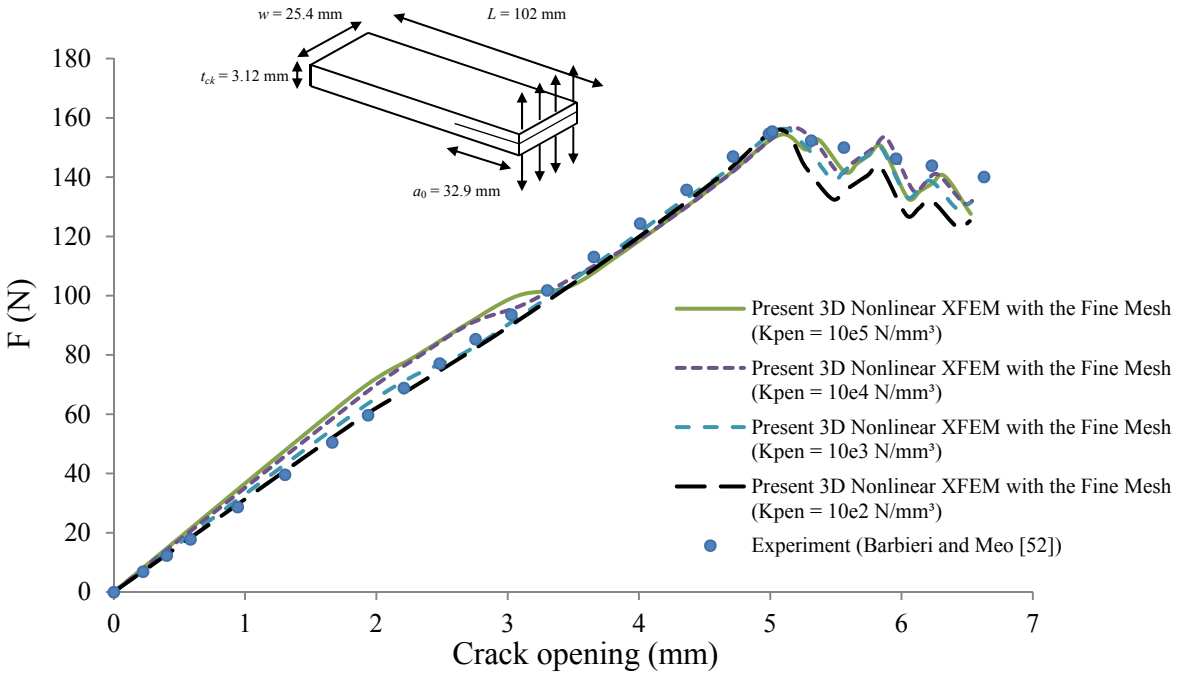

Figure 3-15 The comparison between DCB test load-displacement results of AS4/PEEK samples with different penalty stiffnesses

According to Figures 3-14 and 3-15, XFEM results are less sensitive to the larger order of penalty stiffness values (from 10^3 to 10^5 N/mm^3) in comparison to the conventional finite element method discussed by Turon et al. [50]. Also, within the above recommended K_{Pen} range, two sets of complimentary simulations on AS4/PEEK samples were run to see the effect of interaction between the mesh size and the penalty stiffness. According to the results in Figures 3-16 and 3-17, the mesh sensitivity decreases using lower values of the penalty stiffness, and vice versa. As AS4/PEEK has a higher critical energy release rate (Table 3-1), a larger cohesive zone region is expected in comparison to T300/977-2 samples and, hence, the sensitivity of simulations to the element size is reduced.

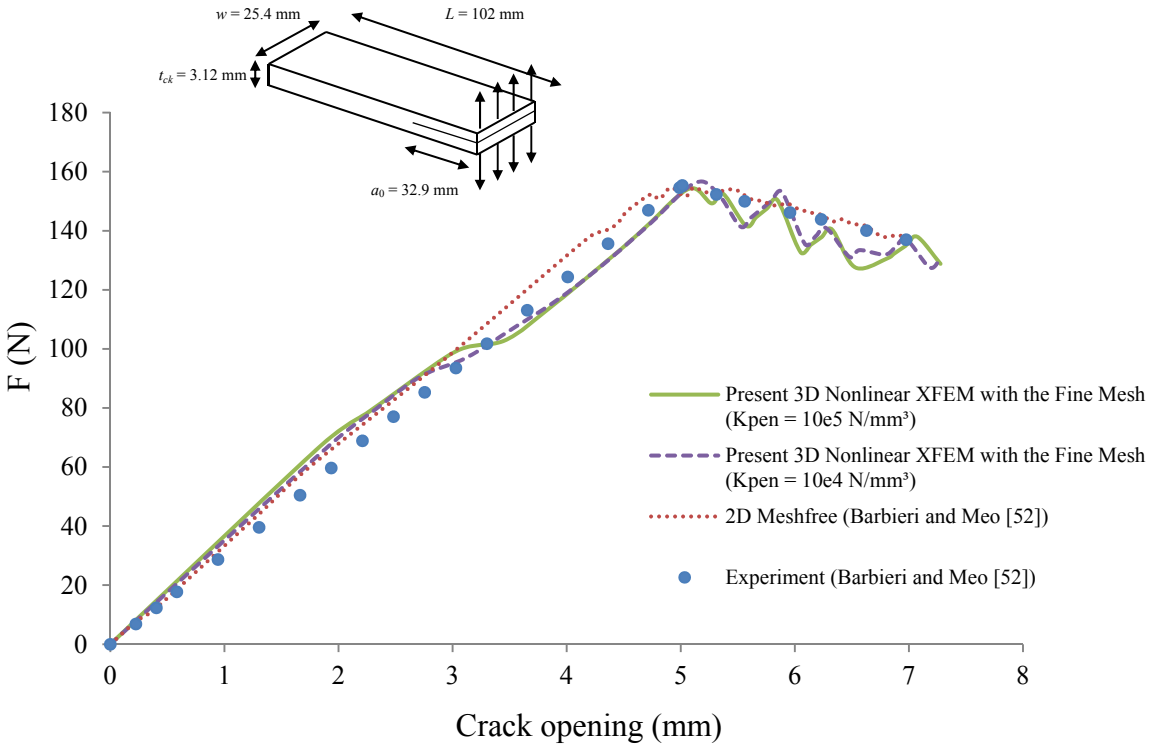

Figure 3-16 The comparison between DCB test load-displacement results for fine mesh analysis of AS4/PEEK and previous works

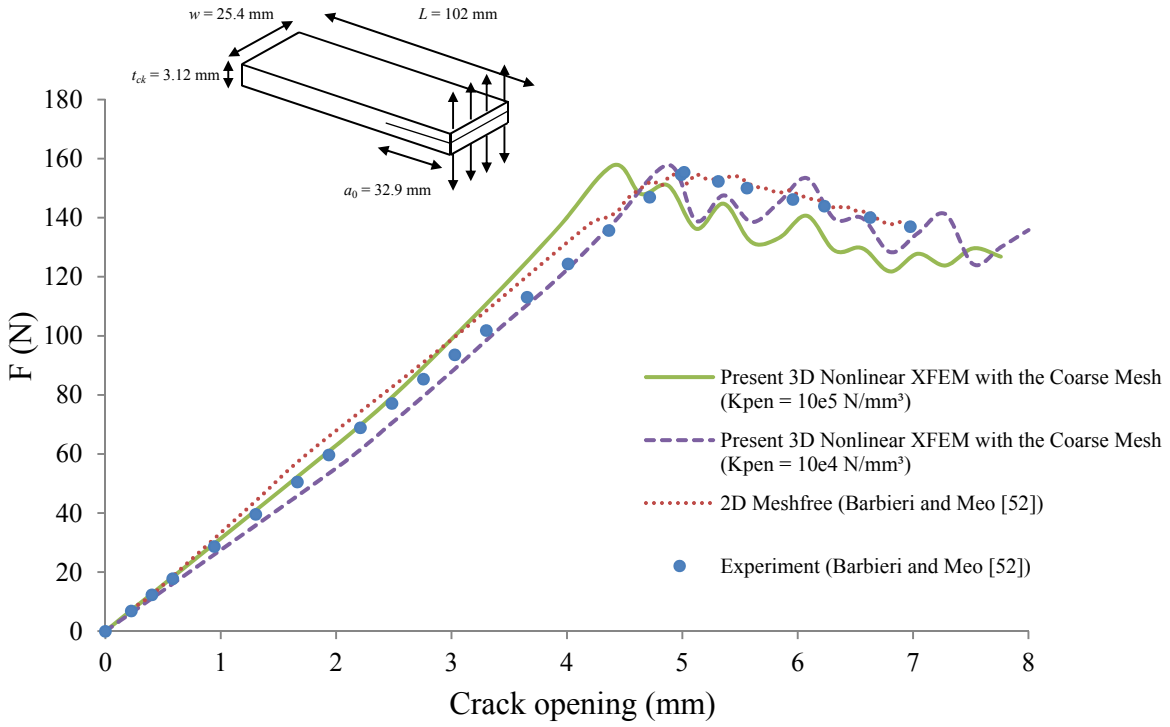

Figure 3-17 The comparison between DCB test load-displacement results for coarse mesh analysis of AS4/PEEK and previous works

3.6.2 Numerical Simulation of the ENF Tests

The End Notch Flexure (ENF) test was also employed in this research to verify the effectiveness of the XFEM model in studying the mode II fracture properties of composite materials. The ENF test configuration is similar to the three-point bending/DCB test, the only difference is that the sample has a pre-assigned crack in the middle layer. ENF samples can be prepared according to ASTM standard D5528-01 [97]. Similar to DCB tests, AS4/PEEK (Table 3-1) was utilized for ENF test simulations. The specimen is 102 mm long, 25.4 mm wide and 1.56 mm thick for each arm, with a 32.9 mm initial crack.

Barbieri and Meo [52] compared their mesh-free method results with the ENF experimental values. Based on their work, it was illustrated that the mode II failure has an abrupt nature and performing its numerical simulation requires a relatively larger cohesive zone, compared to DCB mode, to capture the entire failure in specimens. In the section to follow, we examine this effect using the XFEM model.

3.6.2.1 Effects of Cohesive Zone Length

Different sizes of cohesive region were considered to model a sudden mode II failure within one failure step and the results were compared with those by Barbieri and Meo [52] (Figure 3-18).

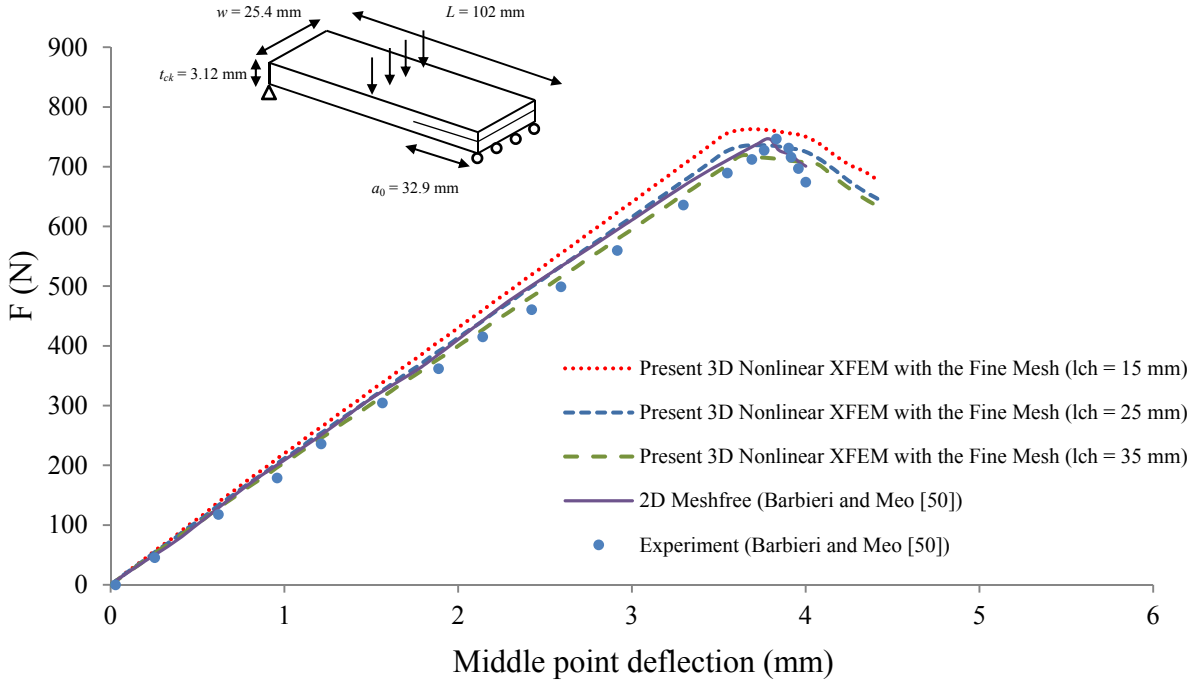

Figure 3-18 The comparison between ENF test load-displacement results for AS4/PEEK and previous works

The results from XFEM illustrate smoother softening behaviour at the peak point of the load-displacement curve. The difference between the experimental curve and the numerical simulation after the peak is perhaps related to the slanted behaviour of the ENF load-displacement curve after crack opening and may be interpreted as an abrupt crack extension under increasing load under only one-step simulation. Also from Figure 3-18, it is evident that increasing the cohesive zone length leads to material softening and consequently decreases the peak value of the numerical load-displacement curve. Finally, comparing l_{ch} values in Figures 3-12 and 3-18 confirms that, for ENF simulation, much larger process zone lengths are required when compared to DCB simulations.

3.6.2.2 Effects of Different Penalty Stiffness Factors

In this section, different penalty stiffness values, K_{Pen}, were employed to evaluate the mode II response of AS4/PEEK samples. The length of the cohesive zone was kept constant, l_{ch} = 15 mm, and the crack propagation happened within numerous steps. A range between 10^3 N/mm^3 to 10^6 N/mm^3 was considered. The effect of this parameter on simulation results is illustrated in Figure 3-19.

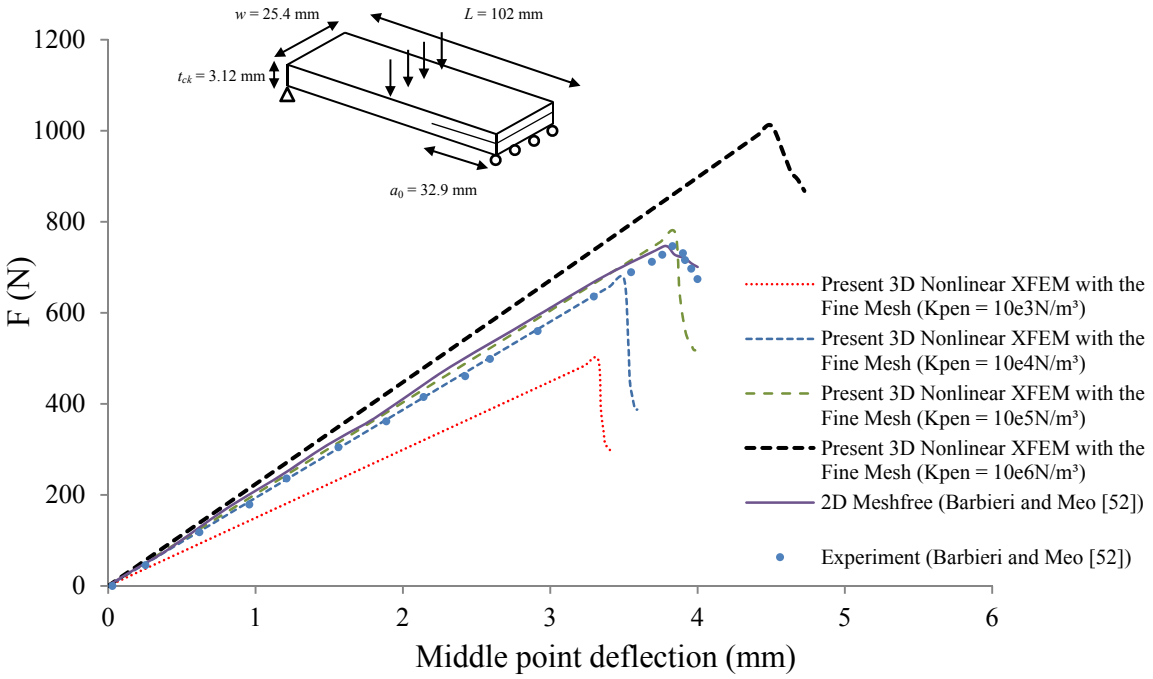

Figure 3-19 Effect of penalty stiffness value on the ENF test load-displacement results for AS4/PEEK sample

It is clear from Figure 3-19 that applying penalty stiffness lower than 10^4 N/mm^3 will result in extensive softening to the model which tremendously reduces the peak load. Such behaviour is derived from lower rigidity in the hardening region of the traction-separation law; however, such dependency of results on K_{pen} may become useful for adapting different material behaviours in different simulations. On the other hand, extensive hardening in the case with K_{pen} higher than 10^5 N/mm^3 can be unrealistic as it reduces the real deflection of the specimen and prevents the actual failure crack opening to be modeled. Finally, comparing Figures 3-14 and 3-19, it is evident the ENF test is much more sensitive to the range of K_{pen}, however, a value of 10^5N/mm^3 seems optimal for both DCB and ENF tests.

3.7 Summary

In this chapter, the nonlinear FEM formulation was summarized for delamination simulations and different solvers for extracting the structures response were introduced. The extension of the nonlinear formulation towards XFEM modeling was then introduced and numerical implementation of nonlinear XFEM in simulating the contact interfaces and CZM was demonstrated. Finally, two (DCB and ENF) example problems from the literature were simulated with the introduced XFEM method and results were compared with the conventional FEM, cohesive interface element and element free models. In the next chapter, the stochastic nature of FRP composite materials will be discussed and the randomness of fracture properties will be introduced to the DCB and ENF simulations of tested PPS/Glass material.

4 Chapter: Modeling Randomness Effect in UD Laminates Delamination: A Non-RVE Approach

As discussed in Chapter 1, the multi-scale nature of composite materials is tied to the mixture of multiple constituent materials. More specifically, in such materials, comingling of the matrix and fibers results in heterogeneous material characteristics and often cumbersome procedures needed to analyze their mechanical properties at different scales. Studying mechanical properties of FRP composite materials can be classified into three different groups. Macro-scale is the largest scale for analyzing the FRP composites and includes coupon size models for experimental, analytical or numerical analyses. In such a scale, anisotropic or orthotropic material properties may be assigned to the material structure. The other extent of this type of analysis is related to micro-scale behaviours of FRP composites with a focus on the constitutive relationships of individual components of the composite as well as the interaction between the matrix and the fibers. The intermediate level of composite materials study is known as meso-scale which links the micro-scale analysis to the macro-scale analysis. Investigation of a laminate lay-up with more concentration on individual plies' mechanical and geometrical properties and orientation is an example of the meso-level study which can also include fracture phenomena such as matrix cracking and fiber breakage as well as delamination and fiber bridging between layers. For an accurate analysis of structural behaviour of composites, it is required to account for the different scales of material properties and include their effects in simulations.

The most basic and yet tangible scale of material analysis in practice is perhaps the macro-scale since it can be implemented to determine the effective properties of large composite structures. Most homogenization techniques aim at this level of analysis and employ smaller-

scale representative volume elements (RVE's) to extract the averaged (effective) mechanical properties of the material at macro-level. The RVE should have specific characteristics; it has to be large enough to contain a sufficient number of heterogeneous characteristics of the composite under study and should assume a periodically distributed properties and boundary conditions in adjacent RVE's. Such distribution assumptions through the entire structure can make the RVE homogenization technique vulnerable to existing defects in specific plies and/or the random distribution of fibers and their bridging. It also may monitor the damage mechanism and propagation of a crack, as these phenomena are relatively present in a local scale rather than a global scale. As a result, full scale (non-RVE) modeling is required for more effective damage modeling.

The earliest attempts to assign statistical (random) properties to the crack location using stochastic modeling of laminates go back to the work of Wang et al. [44] and Fukunaga et al. [98]. More detailed investigation on the heterogeneous nature of laminates due to non-uniform fiber distribution was performed by Baxevanakis et al. [40] where they employed an image analysis technique and demonstrated the unreliable aspects of periodic and quasi-periodic assumptions of fiber distribution material, especially in the case of damage modeling of FRP composites. Further study on RVE assumptions by Bulsara et al. [99] suggested the efficient size effect of RVE's. Trias et al. [43] compared stress and strain distributions of a periodic (RVE) model with a random model and concluded that a periodic assumption should be employed for extracting the effective properties of structures in global scale, while including the randomness is required for local analysis of structures such as matrix cracking and crack propagation. Silberschmidt [100] connected the microstructural randomness to the macro-level analysis and revealed that the fluctuation of mechanical properties is a result of

non-uniform fiber distribution. In the most recent investigation, Ashcroft et al. [48] applied a Weibull distribution to a set of cohesive elements and modeled the damage evolution of CFRP laminates. In their work, fracture energy toughness was defined statistically and exploited from a random distribution.

The influence of the randomness of fiber distribution would increase in unidirectional (UD) FRP laminates as the possibility of fibers penetration within different adjacent layers of composite raises and leads to larger process zones in front of the crack. The response of the structure in such a case during the interlaminar crack growth will demonstrate a resistance while damage evolves and forms a resistance curve known as an R-curve. Fiber bridging results to an increase in fracture toughness of the material from initiation to steady-state delamination extension [101]. More studies on R-curves and fiber bridging showed that despite the fact that fiber bridging can directly affect the effective material properties and hence the shape of the R-curve, it can also be the case that the R-curve is affected by specimen geometry [102]. Nairn [103] combined the energy release rate of fracture mechanics with a CZM traction-separation law to represent the fiber bridging and extracted the R-curve of the model process zone. Airoldi and Dávila [104] applied experimental data and FEM to extract the cohesive element parameters and predicted the R-curve of delamination tests with fiber bridging. As also evident from their work, a high scatter of fiber bridging can exist in UD laminates and would have a significant effect on their macro-level performance.

In the next sections of this chapter, the elastic mechanical properties of PPS/Glass will be assessed. R-curves of fracture experimental tests (DCB and ENF) with regards to uneven fiber/bridging distribution in the fabricated PPS/Glass UD laminates (Section 2.2) will be

studied first. Then, stochastic fracture properties of the material will be adapted into the developed XFEM model and used to capture non-repeatable material response.

4.1 Sample Preparation: Poly (phenylene Sulfide) (PPS)/Glass FRP

In recent decades the fiber reinforced thermoplastic composites have drawn more attention to some high-tech industries as compared to thermoset composites, as they are lighter, tougher, more sustainable, and more cost-effective with the right manufacturing process. Among different polymers used in thermoplastic composite industries, Poly Phenylene Sulfide (PPS), Poly Butylene Terephthalate (PBT) and Poly Ether Ether Ketone (PEEK) have demonstrated strong thermal and mechanical performances [105]. In the present work, PPS resin was chosen as a base material for manufacturing in-house test laminates. PPS is a semi-crystalline polymer and has excellent mechanical, thermal and physical properties. Its strength and affordability can help PPS to fill the gap between the partially crystalline industrial plastics and semi-crystalline resins such as PEEK. In addition, reinforced PPS with glass fibers offers economical advantages in comparison to carbon fibers by delivering high resistance characteristics against chemical and solvents, low moisture absorption, short thermoforming mould cycles with a greater creep strength and durability against temperature changes [105]. Typical applications of PPS/Glass composites in current industries vary from components in construction equipment, pumps parts and impellers to plastic parts in motor vehicles. In Figure 4-1, a microscopic image of UD tape of PPS/Glass, commercialized by TENCATE ADVANCED COMPOSITES [105], is depicted at two different regions of a sample. This particular product has an average void level less than 0.2% with a more even fiber-matrix distribution in the corner of the tape.

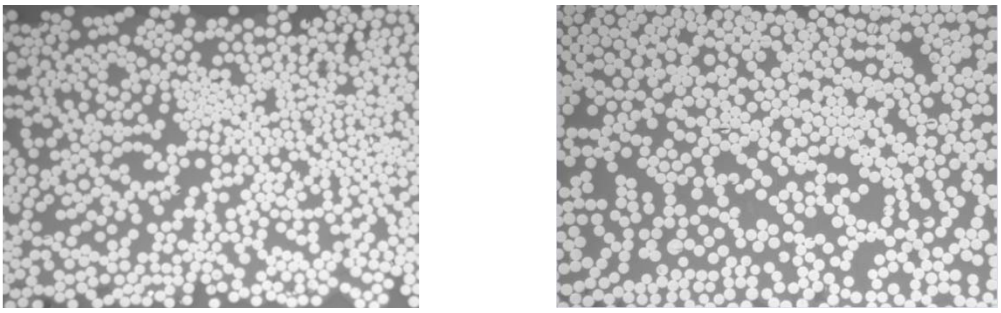

(a) (b)

Figure 4-1 Microscopic images of fibers and matrix distribution of PPS/Glass UD tape: (a) Corner of the tape, and (b) Middle of the tape [105]

The common forming procedures used for making PPS/Glass laminates are mainly similar and their minor differences, apart from cost, lie on the range of required temperature or pressure as follows.

1- **Press Lamination**: In this process, PPS/Glass UD plies can be stacked in any desired orientation in a frame mould. Then, the frame is placed into a heated platen press where the assembly temperature is increased to approximately 330-360^{o}C at a contact pressure until the PPS matrix melting point is reached. Namely, the platen pressure can be raised to 1.7 MPa and the assembly kept under this state for approximately 30 minutes. Then, the assembly fixture temperature is reduced by a cooling cycle flow passing through platens while the pressure is maintained.

2- **Autoclave Lamination**: Similar to the press lamination process, in this process PPS/Glass laminas are laid-up in any desired orientation and placed in a vacuum bag throughout the entire process. A high temperature resisting material is used for the vacuum bag. The fixture

assembly is placed in the autoclave for 30 minutes in a temperature close to 315-330^{o}C. During this time, the pressure on the fixture is increased from ambient to 0.68 MPa. After the heating process, the part is cooled down to a temperature less than 93^{o}C and the pressure can be dropped to ambient while the vacuum is released.

In the present work, the press lamination method (using a Wabash 100 Ton Press shown in Figure 4-2) was utilized to form the required test laminates. In the assembly process, 14 layers of PPS/Glass UD lamina were stacked. Polyimide Teflon (0.147 mm) with high temperature performance (melting at 426^{o}C) was placed in the middle of the stacked pile to represent the predefined crack in the specimens. The entire assembly was brought together in a preheated moulding fixture and then placed in a heated platen press where the assembled fixture's temperature was sustained at approximately 350^{o}C. The heating platen pressure was raised to 0.44 MPa and was kept in this state for approximately 28 minutes. This timing span let the inside of the mould reach the melting point of PPS at 350^{o}C within 23 minutes and permitted the fibers to consolidate over 5 minutes in the molten matrix. Then, the assembly's temperature was reduced via a cooling flow passing through platens for 20 minutes while the pressure was maintained at 0.44 MPa (Figure 4-2).

It is worth adding that, 2D thermoplastic composite plies can also be formed into 3D complex shapes using the above apparatuses and appropriate moulds. For the PPS/Glass laminate, it can be stacked and heated to around 330-345^{o}C using an infrared oven for a maximum of 8 minutes and then transferred to a predesigned core/cavity mould where it can be formed to a 3D shape under a pressure between 0.1-0.4 MPa. Depending on the part shape and dimensions, the production process may take under 10 minutes. This process is often referred to as thermoforming or stamping.

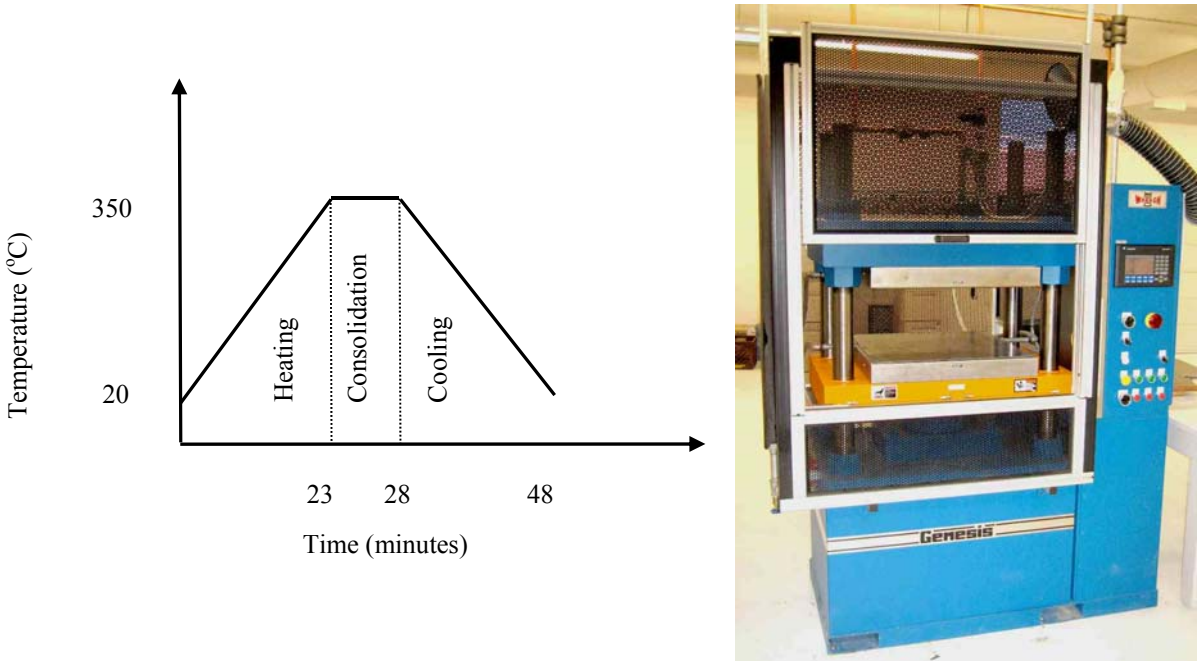

Figure 4-2 (a) Forming cycle used for preparing PPS/Glass test samples using (b) an automated press apparatus (Wabash MPI 100 ton)

4.2 Elastic Mechanical Properties of PPS/Glass FRP Composites

As mentioned earlier, the American Society for Testing and Materials (ASTM) standards [55-57] can be employed to extract the material elastic constants. In the first step, the longitudinal and transverse elastic moduli of the PPS/Glass samples were measured based on ASTM D 3039/D 3039M [56]. The test specimens were prepared with 250 mm length, 20 mm width, and 3 mm thickness. After the test specimen was firmly aligned and tightened in the tensile machine grips, a transducer was mounted on the mid-span, mid-width of the specimen. Then, the loading cell started to load the specimen with the rate of 2 mm/min. Observed failure was explosive failure in the gage area at the middle of specimen (XGM) for longitudinal fibers, while in the transverse direction, lateral failure happened close to the grip at top or bottom

(LAT/LAB) of the specimen. Table 4-1 contains the test results for longitudinal and transverse directions.

Table 4-1 Mechanical properties extracted from tensile testing

Test repeat	**Longitudinal (fiber) Direction**		**Transverse (perpendicular to fiber) Direction**	
	Elongation (%)	**Modulus of Elasticity** (MPa)	**Elongation** (%)	**Modulus of Elasticity** (MPa)
1	5.77	45326.07	0.13	3490.58
2	9.68	43303.08	0.06	1334.61
3	9.64	43601.28	0.08	1176.69
4	8.34	50547.07	0.09	1797.79
5	6.84	46821.49	0.10	1513.28
6	8.91	39836.18	0.09	1289.65
7	6.30	38975.62	0.02	2100.46
Average	7.93	44058.68	0.08	1814.72
Standard Deviation	1.40	3460.23	0.03	697.73

As we needed to acquire the remaining material properties for subsequent numerical simulations, the average Young's modulus extracted from experimental data above were compared to the supplied material data sheets and brochures (see Figure 4-3 for a snapshot) to find and adjust the closest set of material properties given the actual fiber volume fraction, reinforcement architecture, etc (for confidentiality reasons the material's full specification and composition have not been disclosed). The final set of elastic properties implemented in the subsequent simulations of this thesis is given in Table 4-2.

Tensile strength warp	35.7	ksi	246	MPa
Tensile strength weft	39.6	ksi	273	MPa
Tensile modulus warp	2.8	Msi	20	GPa
Tensile modulus weft	2.6	Msi	18	GPa
Compression strength warp	24.4	ksi	169	MPa
Compression strength weft	16.9	ksi	117	MPa
Compression modulus warp	2.9	Msi	20	GPa
Compression modulus weft	2.5	Msi	18	GPa
In plane shear strength	9.1	ksi	63	MPa
In plane shear modulus	109.0	ksi	752	MPa

Figure 4-3 Snapshot of elastic mechanical properties for a typical woven PPS/Glass ply from material data sheets

Table 4-2 Final set of elastic properties of manufactured UD PPS/Glass FRP composites with "1" being the fibers direction; "2" and "3" are perpendicular directions to fibers.

Effective Elastic Properties		
E_{11} = 44,400 MPa	G_{12} = 880 MPa	v_{12} = 0.25
E_{22} = 1800 MPa	G_{23} = 660 MPa	v_{23} = 0.48
E_{33} = 1800 MPa	G_{13} = 880 MPa	v_{13} = 0.25

4.3 Fracture Tests on the Fabricated PPS/Glass Composites

Both DCB and ENF tests were conducted on the PPS/Glass UD specimens according to the procedure described in ASTM D5528-01 [97]. The main goal of these tests was to measure the mode I and II fracture energy toughness properties of the material. In DCB test, specimens with pre-inserted delamination were put in the tensile machine and underwent opening displacement with the rate of 2 mm/min on the grips. At the onset of delamination extension,

the force on the loading cell was recorded while delamination is was permitted to propagate for 5 mm, observed and controlled visually, before unloading the specimen for the next loading step with extended delamination length. In the case of ENF test, a similar specimen configuration with pre-inserted delamination was employed while the test set-up was coincided with the three point bending test. The loading on the mid-span was increased with a rate of 2 mm/min until the delamination commenced in the specimen (Figure 4-4). At this point, the force was recorded and used in energy release rate calculation. The calculation steps via recorded data from DCB and ENF tests have been described in Appendix B.

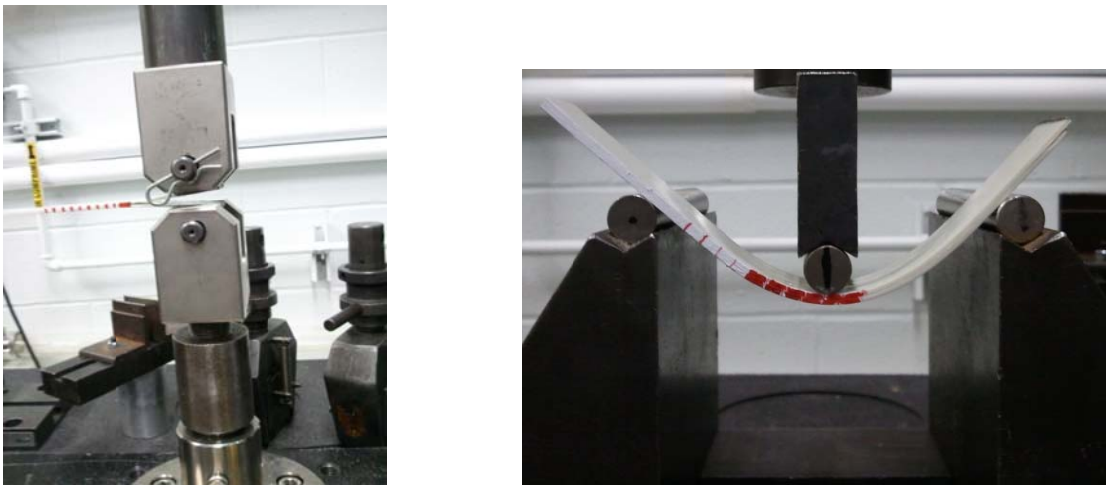

(a) (b)

Figure 4-4 Experimental test set-ups: (a) DCB, and (b) ENF

4.3.1 DCB and ENF Test Results

In order to measure the mode I fracture energy toughness, three different calculation methods were employed over the DCB test results with three repeats: Compliance Calibration Method, Modified Beam Theory Method and Modified Compliance Calibration Method. For the ENF

test, based on the nature of the mode II failure, crack propagation happens due to excessive shear deformation and has an abrupt nature as addressed in Chapter 3. Such behaviour makes it difficult to control the external load to achieve a target crack extension. Due to this test limitation, in the present study only the first step of crack propagation in ENF tests was considered while the test repeats were carried out with the same pre-assigned crack length (43 mm).

Figures 4-5 and 4-6 depict the obtained experimental data from three repeats of the DCB test. According to the observed increasing trend between crack length and the critical energy release rate, it could be concluded that the material experiences fiber bridging during delamination. This was further verified by macro- and micro- imaging of samples (Figure 4-7). It is worth adding that fiber bridging is more likely to occur in unidirectional laminates than in woven fabric composites, since the layers in UD's are laid-up in a single orientation and during the moulding phase, as the matrix melts, there is less geometrical confinement to prevent fibers from penetrating into adjacent layers. The clear data scatter through the test repeats in Figure 4-5 also shows that, despite the DCB sample coupons have been cut from the same large (master) plate, the distribution of effective material properties could randomly vary from one coupon to another. This observation may be due to a non-uniform reinforcement pattern, uneven pressure or heating/cooling effect during the compression moulding stage of the master plate. Even within the same plate, more uniform pressure or heat concentration in the middle section of the plate may have been present compared to its edge sections (also recall Figure 4-1).

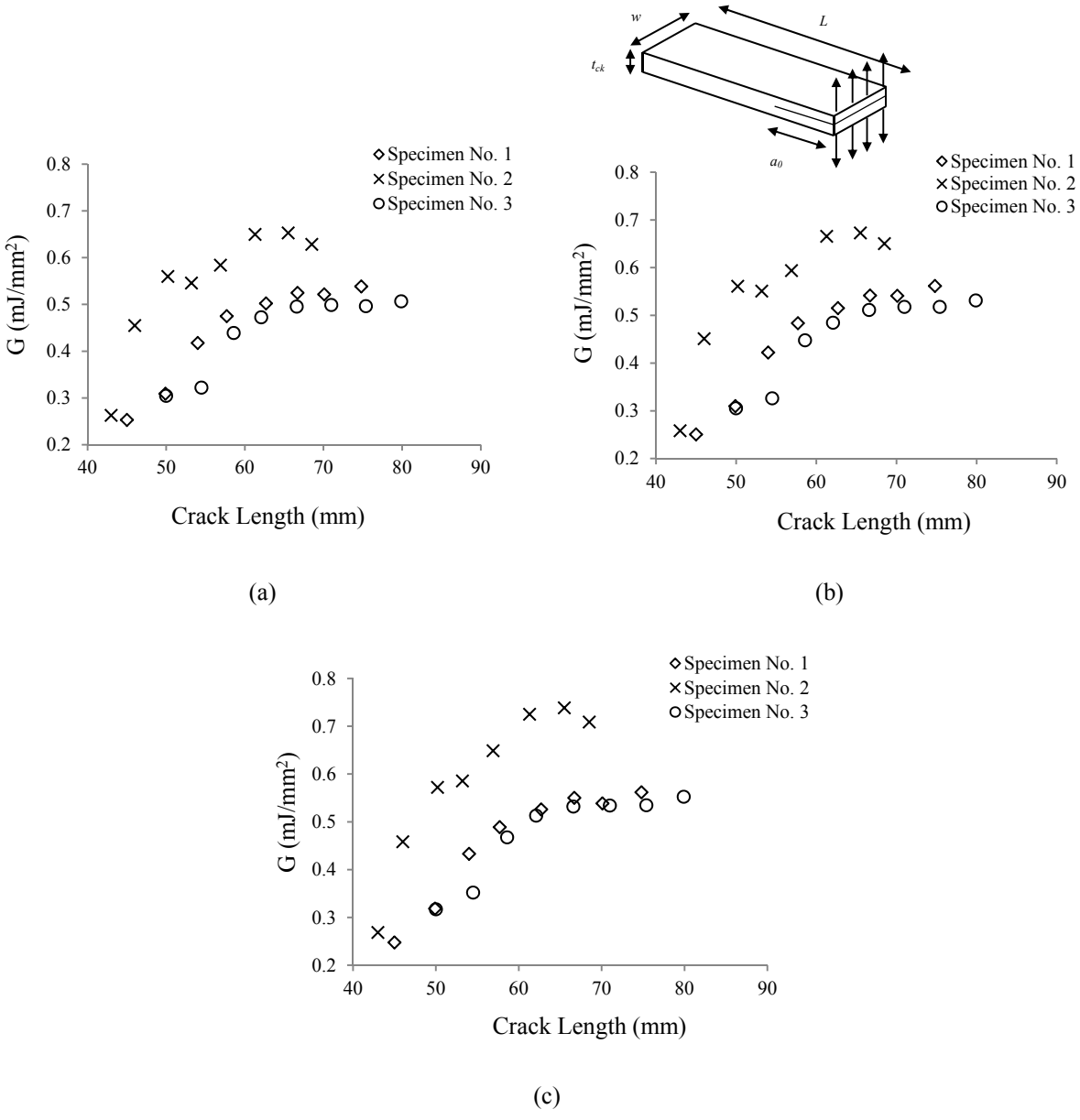

Figure 4-5 The variation of fracture energy toughness versus crack length for the three tested samples using: (a) Compliance Calibration Method, (b) Modified Beam Theory Method, (c) Modified Compliance Calibration Method [97]

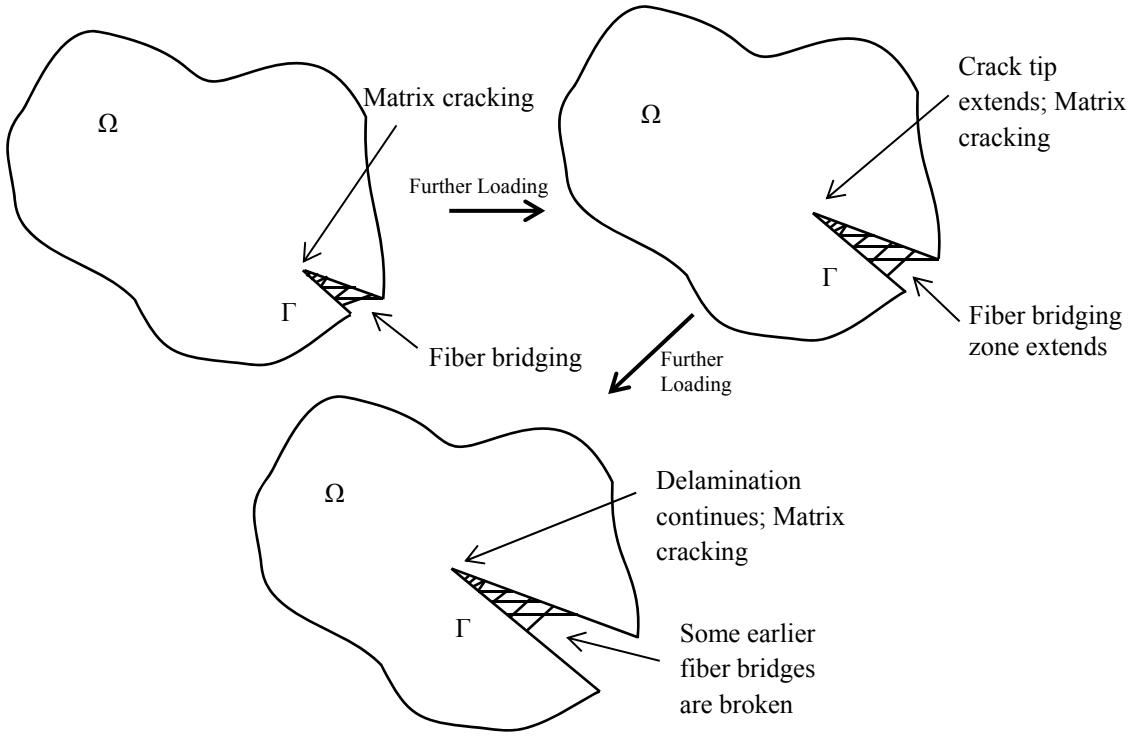

Figure 4-6 Illustration of the fiber bridging zone (FBZ) during crack propagation; as the crack length increases, FBZ emerges in the cracked region up to the fiber's rupturing displacement; after fiber breakage, the FBZ effect vanishes from the region which has exceeded the failure opening displacement

According to ASTM 5528-01 [97], the modified beam theory provides more conservative result in comparison to other methods, and hence it is recommended for design purposes. Finally, in addition to the ASTM D5528-01 [97] discontinuous DCB test, continuous crack-opening tests, i.e., without unloading and re-loading for the next initial crack length configuration, were performed to monitor the effect of progressive failure in the specimens (results to be discussed in Section 4.5).

(a)

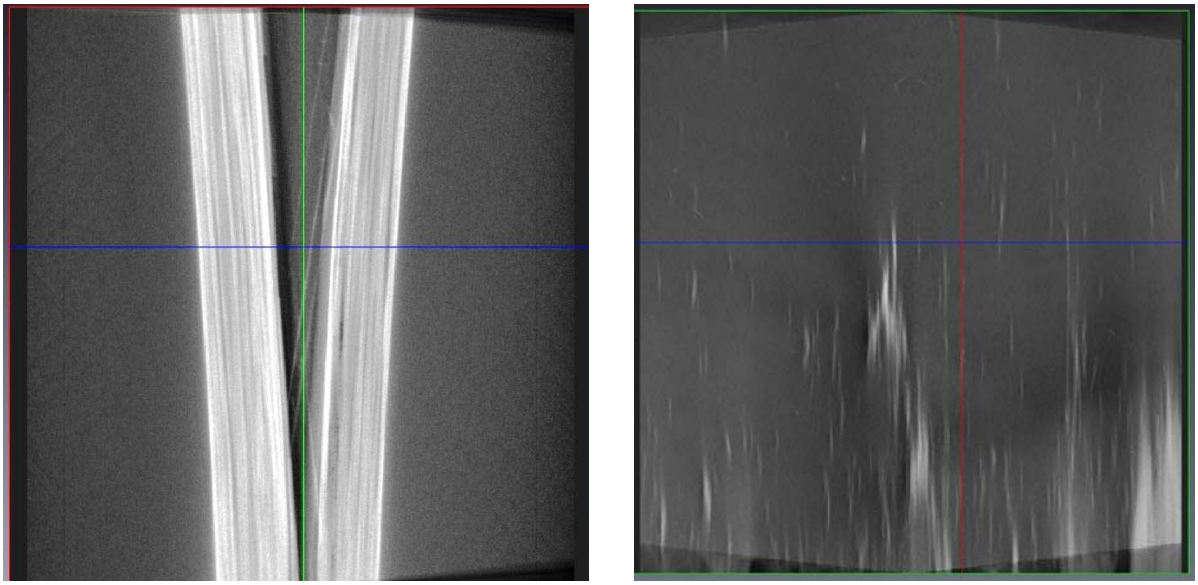

(b) (c)

Figure 4-7 Different images of a DCB test sample: (a) macro scale image of fiber bridging, (b) X-ray micro-tomography image of fiber bridging along the sample thickness, and (c) attenuation of the X-ray reflection due to absorption; demonstrating uneven distribution of fibers

For ENF tests, as mentioned earlier capturing the step-by-step crack propagation was not feasible, therefore only the initial step of crack propagation was used for the analysis (Figure 4-8). Similar to the DCB test, continuous loading was also employed for the ENF test to observe the effect of fiber bridging with extensive crack evolution in the test coupons (results

to be discussed in Section 4.5). The summary of fracture properties extracted from DCB and ENF tests is shown in Table 4-3.

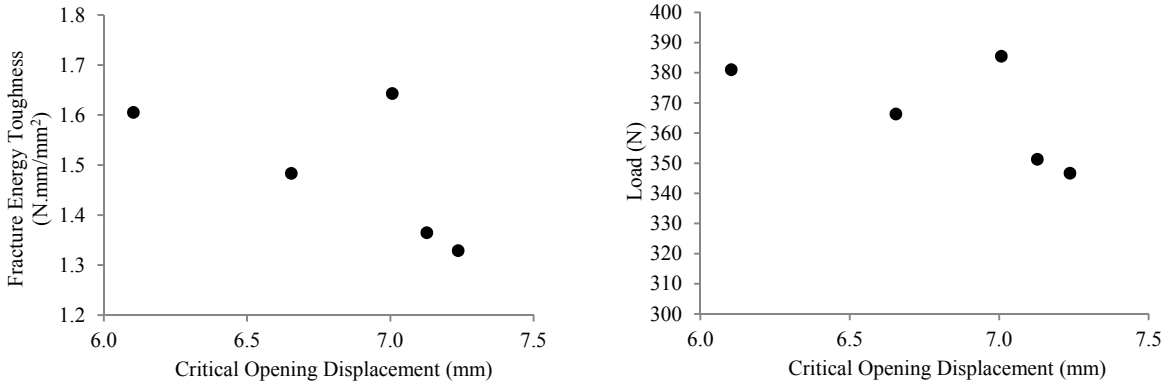

(a) (b)

Figure 4-8 ENF test repeat results with a constant crack length (43 mm): (a) the variation of fracture energy toughness versus the mid-span displacement, and (b) the variation of bending load versus the mid-span displacement.

Table 4-3 Fracture properties of PPS/Glass samples extracted from DCB and ENF tests

Fracture Properties	
Mode I (DCB)	**Mode II (ENF)**
T_{max} = 9.6 MPa	T_{max} = 5.5 MPa
$G_{IC(ave)}$ = 0.48 kJ/m^2	$G_{IIC(ave)}$ = 1.48 kJ/m^2
As a function of delamination length:	As a function of delamination length:
$G_{IC} = 0.0075a_{cr} + 0.04$ kJ/m^2 (For a_{cr}> 40 mm)	$G_{IIC} = 0.045a_{cr} - 0.5$ kJ/m^2 (For a_{cr}> 40 mm)
$\delta_0 = 9.6e^{-05}$ mm	$\delta_0 = 5.5e^{-05}$ mm

4.4 Stochastic Fracture Properties

As addressed in Section 4.1, FRP composite materials demonstrate a large amount of randomness in material properties due to an uneven distribution of fibers in the matrix, and the possible penetration of fibers within different layers of laminate during the forming processes (especially in the case of unidirectional laminates). In the present work, fracture properties of the tested samples are considered to have a stochastic nature based on non-repeatability observed in repeated experiments, as opposed to deterministic approaches where averaged values of experimental results are assumed for the estimation of material properties. Namely, a random number within the range of experimentally measured fracture energy

toughness values was picked to form a stochastic bilinear traction-separation law of enriched elements in the cohesive zone (Figure 4-9):

$$G_C = G_{C(ave)} + (-1)^{Rand_1} Rand_2 \times G_{C(std)} \tag{4-1}$$

where $Rand_1$, $G_{C(ave)}$ and $G_{C(std)}$ are the random integer (odd or even to assign a random sign), average and standard deviations of fracture energy toughness, respectively.

.

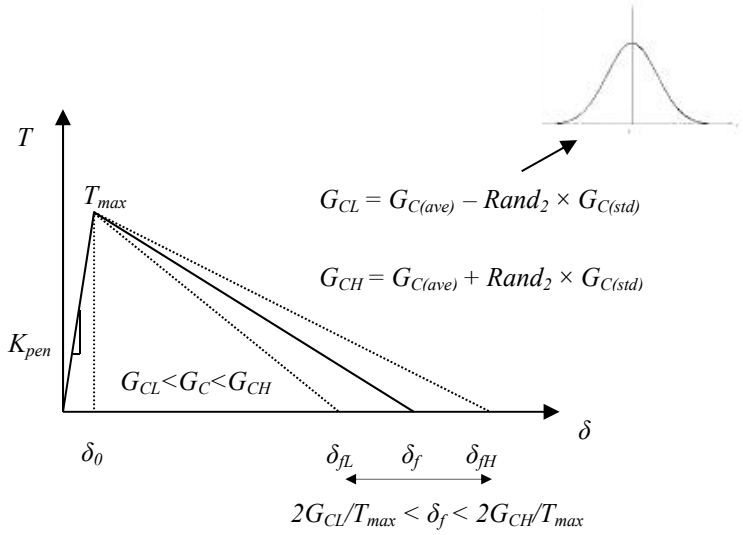

Figure 4-9 Proposed stochastic bilinear traction-separation behaviour ($Rand_2$ is a random number taken from a 2-parameter Weibull distribution; G_{CL} and G_{CH} correspond to the lower and upper limits of G_C via Equation 4-1)

Following the fiber bridging discussion in Section 4.3 and the observed experimental trend in Figure 4-1, the fracture energy toughness distribution was considered to be a function of the crack length and hence, a linear interpolation was utilized to extract $G_{C(ave)}$ for each specific crack length. For $G_{C(std)}$, it can be a constant or in a more general form it can scale with $G_{C(ave)}$, which in turn becomes a function of crack length. The second random number ($Rand_2$)

corresponding to individual enriched elements in each stage of damage evolution was taken from a uniform distribution with a range of 0 to 1. The randomly selected values were then converted to a Weibull two-parameter distribution between 0 and 1 via:

$$Rand_{2\,weibull} = \left[\frac{-1}{\alpha_1}\ln\left(1 - Rand_{2\,uniform}\right)\right]^{\frac{1}{\beta_1}} \tag{4-2}$$

where $\alpha_1 > 0$ is a shape parameter and $\beta_1 > 0$ is the scale parameter of distribution and both are considered to be equal to 3. It should be added that, according to conventional bilinear traction-separation behaviour, a direct relationship exists between the critical fracture energy toughness, G_C, failure crack opening displacement, δ_f, and maximum interface strength, $T_{\max}$:

$$G_C = \frac{T_{\max}\delta_f}{2} \tag{4-3}$$

Therefore, the obtained statistical distribution of the fracture energy toughness can be converted into the variation of failure crack opening and/or maximum interface strength of material via Equation (4-1). Khokhar et al. [106] introduced the randomness into their simulation by implementing a relationship between random fracture energy toughness and the maximum interface strength by keeping the failure crack opening displacement constant. To improve the numerical simulation's convergence, the present study assumes a constant value for the maximum interface strength (see Table 4-3) while the failure crack opening displacement is randomly varied during damage evolution (see Figure 4-4). This approach relies on constant penalty stiffness and prevents the over-strengthening of elements' stiffness in the process zone. It also stands with the fact that the crack length extension in test

specimens is a function of the crack-tip opening displacement (CTOD) and the energy release rate in front of crack-tip.

4.5 Numerical Results and Discussions

An XFEM model of the PPS/Glass composite samples under DCB tests were established using the developed ABAQUS user-defined element subroutine. To consider the stochastic aspect of fracture properties in conjunction with Equation (4-1), two different approaches were employed. In the first approach, the standard deviation of fracture energy toughness was assumed to be constant during the crack propagation (i.e., equal to the standard deviation of the entire DCB experimental points in Figure (4-5). In the second approach, a linear function was assigned using test data to relate the fracture energy toughness standard deviation to the crack length (Table 4-4).

Table 4-4 Employed standard deviation schemes in stochastic simulations of DCB test

Standard Deviation	
Constant	**Function of delamination size**
$G_{C(std)} = 0.121$ kJ/m^2 (For $a_{cr} > 40$ mm)	$G_{C(std)} = 0.2125 - 0.0016a_{cr}$ kJ/m^2 (For $a_{cr} > 40$ mm)

Figure 4-9 shows a comparison of opening force between measured and predicted values via the above two approaches under the standard (discontinuous) DCB tests [97].

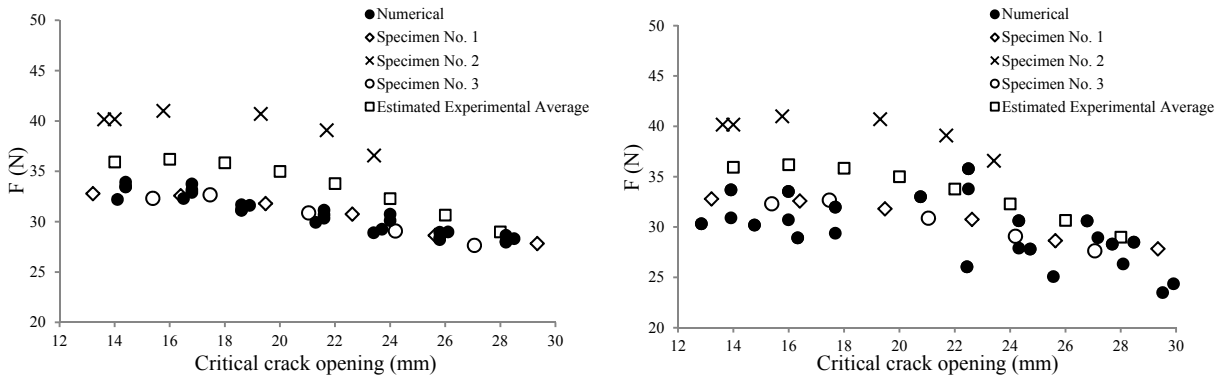

Figure 4-10 Comparison of the opening force in stochastic simulations of DCB tests with experimental data using: (a) constant standard deviation formulation, and (b) standard deviation as a function of crack length

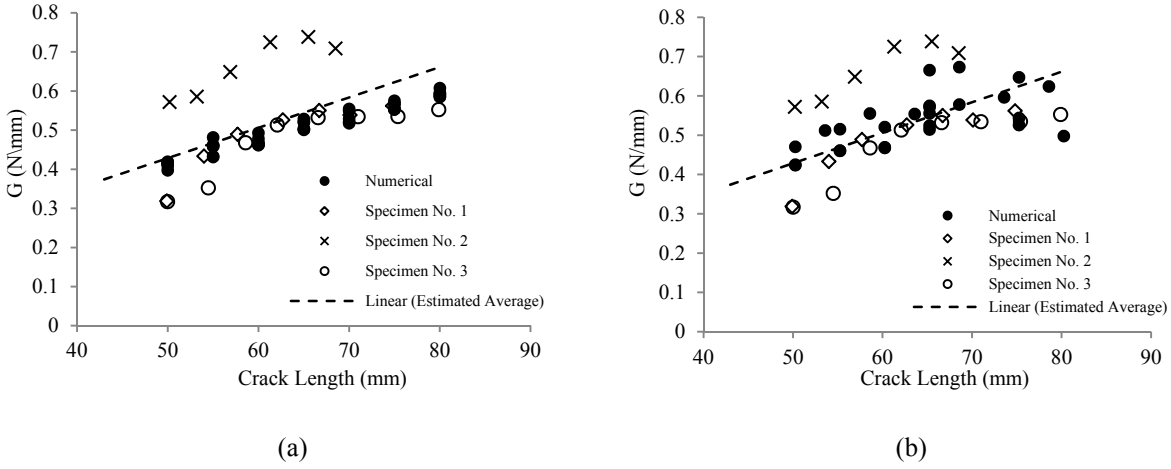

Figure 4-11 Comparison of predicted fracture energy toughness via stochastic simulations of DCB tests with experimental data using: (a) constant standard deviation formulation, and (b) standard deviation as a function of crack length

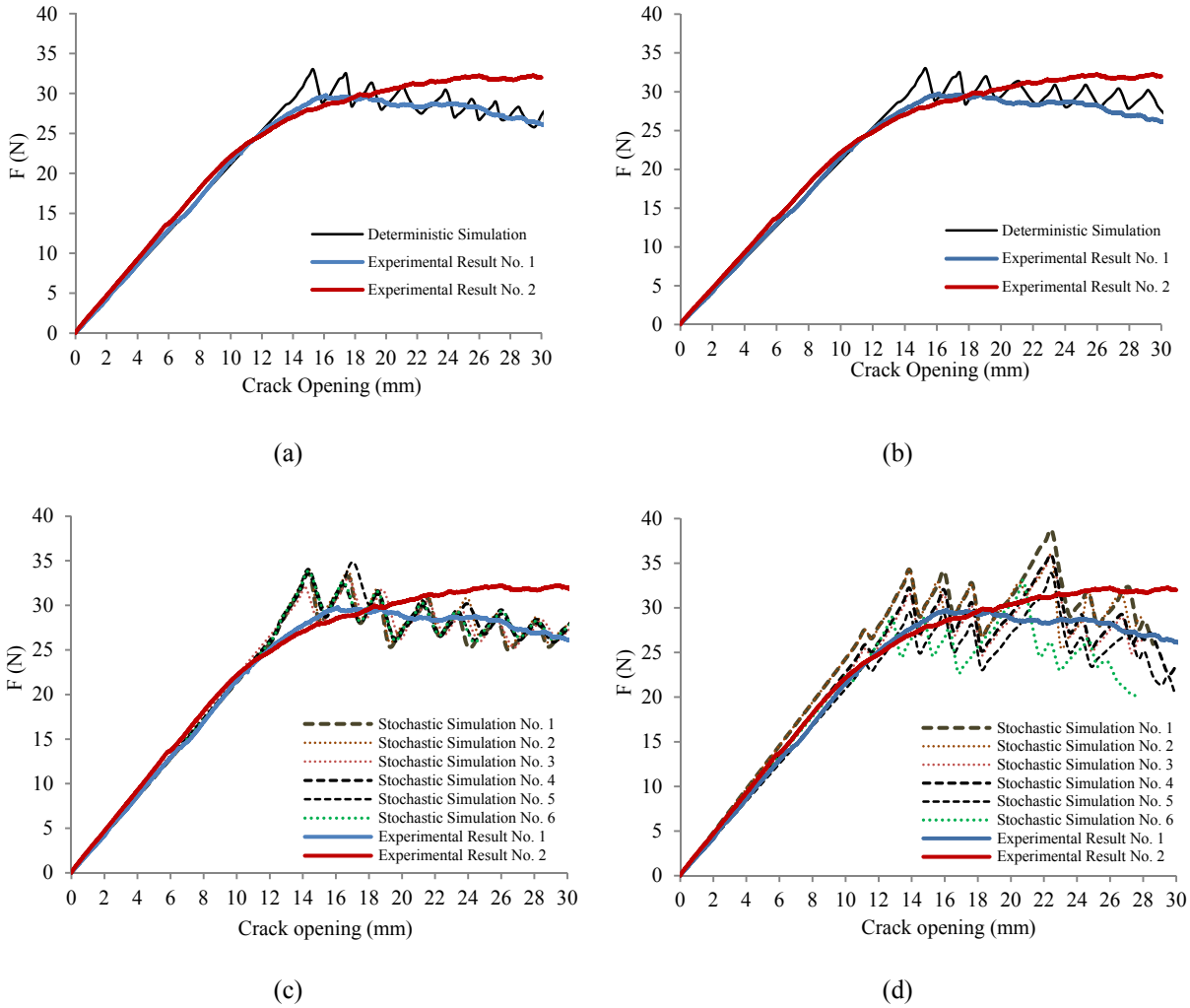

Figure 4-12 Comparison of measured opening force with predicted values in stochastic and deterministic simulations of continuous DCB test using: (a) fracture energy/toughness remains equal to the average value of experiments, (b) fracture toughness only changes with increase in delamination length, (c) fracture toughness increases with extension of delamination with constant standard deviation formulation, and (d) fracture toughness increases with extension of delamination with standard deviation as a function of delamination length

The stochastic fracture energy toughness values (via the XFEM force values in Figure 4-10 and the standard formulas of ASTM D5528-01 [97]) were also calculated and compared to the measured values in Figure 4-11. Similarly, the comparison of results under the continuous test mode, i.e. progressive damage, is depicted in Figure 4-12.

According to Figure 4-11, prediction results for the discrete (standard) DCB case with constant standard deviation tend to follow experimental results that are closer to the average data points. This observation has been directly reflected in the continuous-mode tests in Figure 4-12. As depicted in Figure 4-12(a), the XFEM simulation with constant fracture toughness and no stochastic effect (i.e., similar to a deterministic simulation) tends to follow the lower bond of experimental repeats. Choosing the lower bond fracture limit can be quite acceptable in practical applications where the safety has the highest impact on design. In Figure 4-12(b) the XFEM simulation with fracture toughness as a function of delamination length, and with no standard deviation effect, shows an increase in resisting force during crack evolution, and a better overall prediction capability. This response in particular demonstrates that the implemented XFEM model in macro-level simulations can capture the effect of fiber bridging in the meso/micro level by increasing the fracture energy toughness during each step of delamination extension. Studying stochastic prediction cases, Figures 4-12(c) and (d), it is seen that having the standard deviation varying with the crack length can reproduce a more realistic (wider) range of results by means of a higher variation introduced to fracture properties. It can also be observed from Figures 4-12(c) and (d) that utilizing a constant standard deviation reduces the fluctuation of stochastic simulations and demonstrates a smoother trend, while the variable standard deviation method leads to larger fluctuations during the crack propagation steps. Interestingly, the highest scatter/fluctuation at the opening

displacement of 22 mm in Figures 4-12(d) coincides with the high deviation observed in mode I fracture experiments in Figure 4-11(b) when the delamination length is close to 65 mm. The numerical results oscillation in Figure 4-12 would have been caused at each crack propagation stage when the energy release rate reaches the critical fracture energy toughness values. More specifically, when CTODs reaches its onset (i.e., crack starts opening), the corresponding elements in front of the crack are progressed within the rigid (high stiffness) portion of the bilinear traction-separation law up to the apex where the maximum interface strength is reached. After this point, the material faces sudden softening and the opening force reduces to the complete failure of elements, leading to the propagation of the crack into the next element where again a local increase of the global opening load is expected. Also, the delamination propagation inherits different size of kinks/jumps which links to the fact that we are allowing the failure opening displacement to vary for different enriched elements. This assumption causes the numerical model to deviate from a smooth trend observed in experimental results. Figures 4-13 and 4-14 show the schematic of crack evolution based on the bilinear traction-separation law and the XFEM model at different stages of delamination.

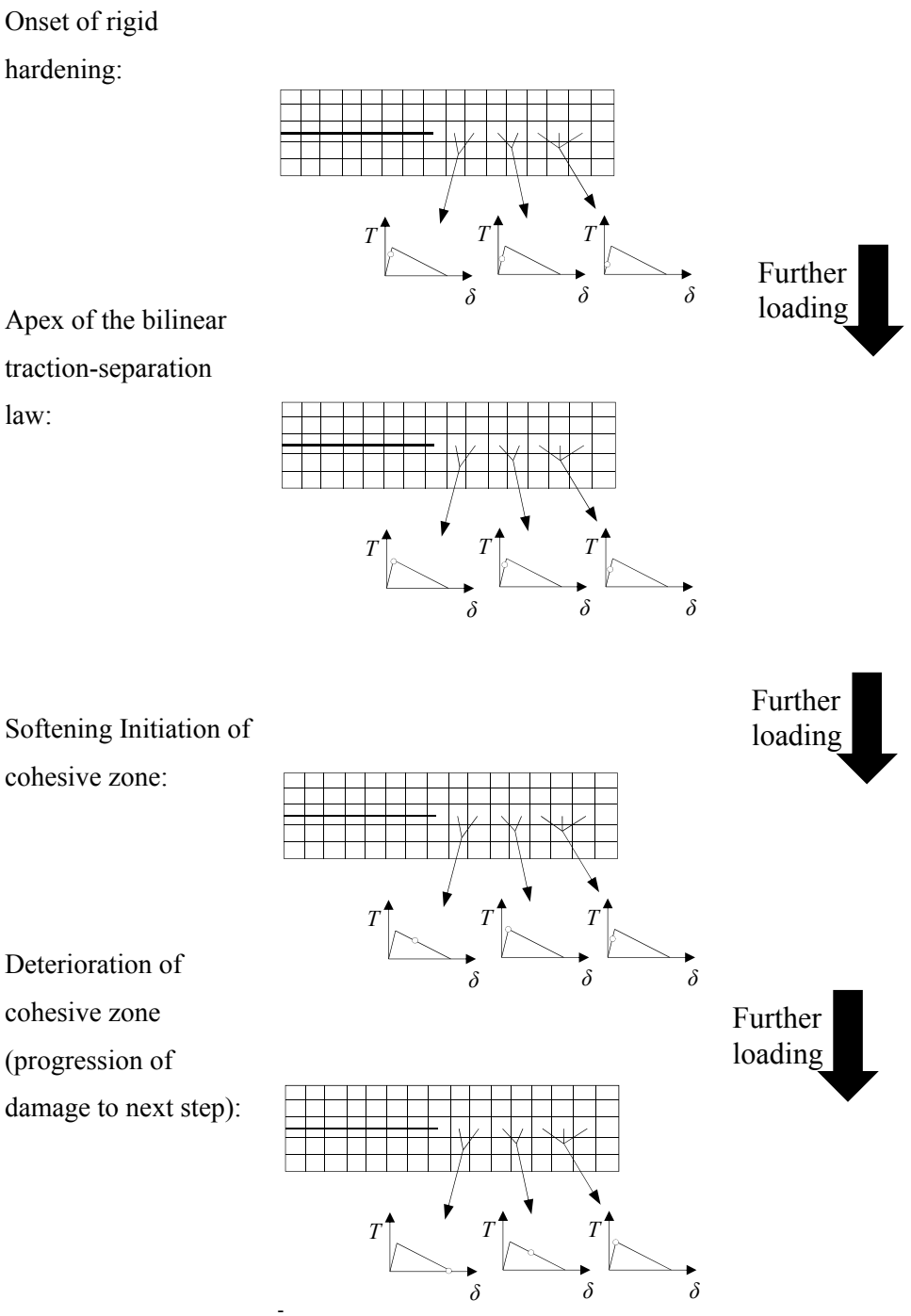

Figure 4-13 Evolution of the cohesive zone in front of crack upon loading in a given simulation step

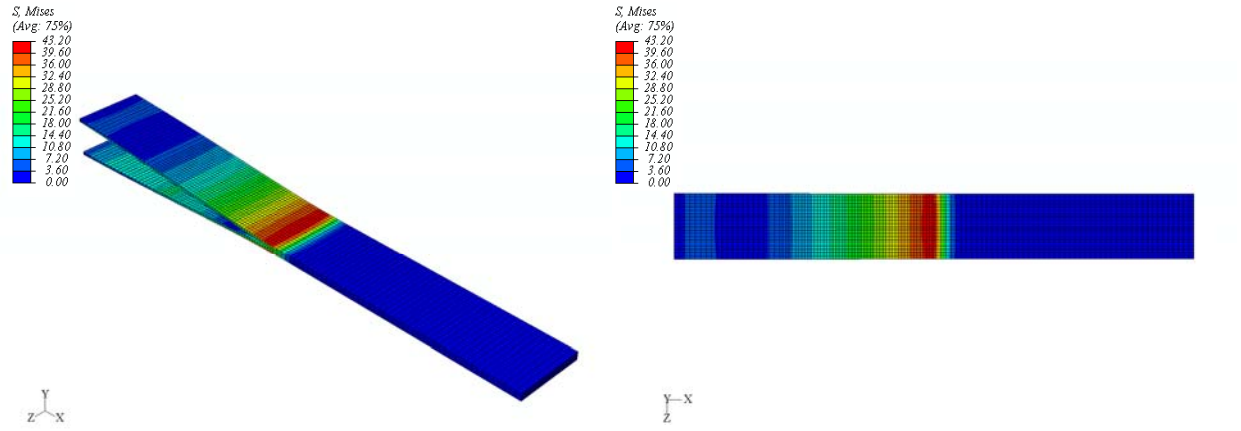

(a)

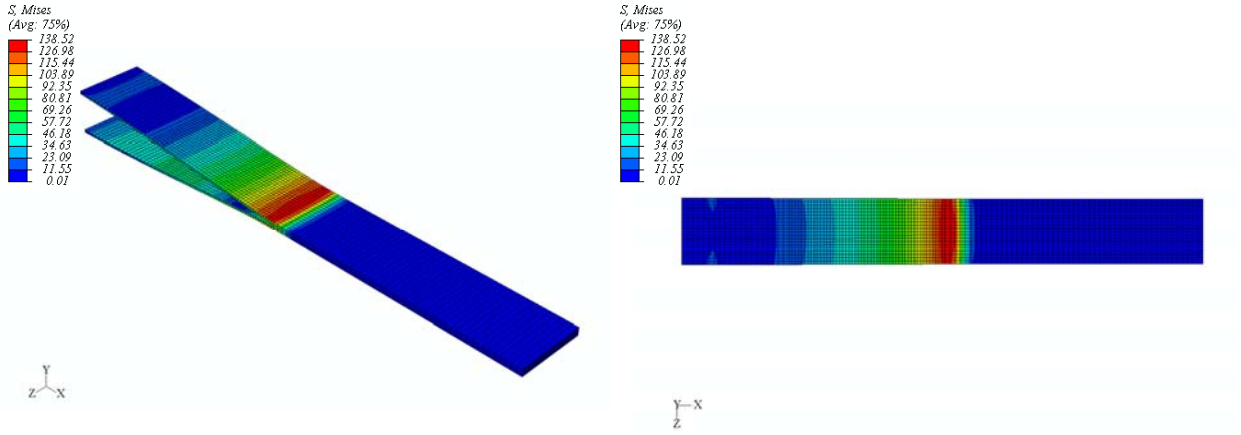

(b)

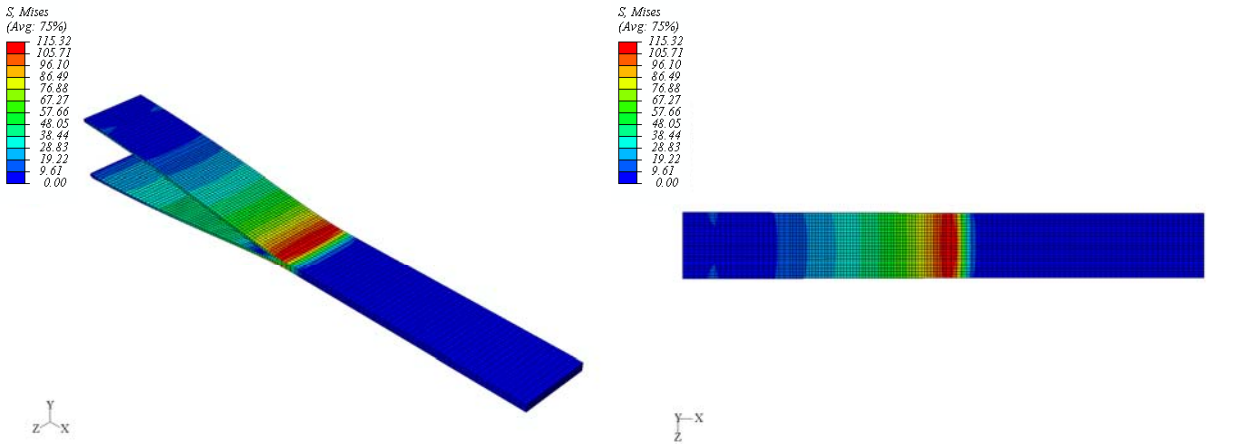

(c)

Figure 4-14 Stages of delamination propagation within the DCB numerical model: (a) Onset of rigid hardening in the process zone, (b) Apex of the bilinear traction-separation law, and (c) Deterioration of the cohesive stiffness

In the case of ENF tests, the experimental set-up was simulated using the same ABAQUS user-element subroutine. Randomness was introduced into the analysis only by means of the constant standard deviation method. The results for continuous delamination are depicted in Figure 4-15.

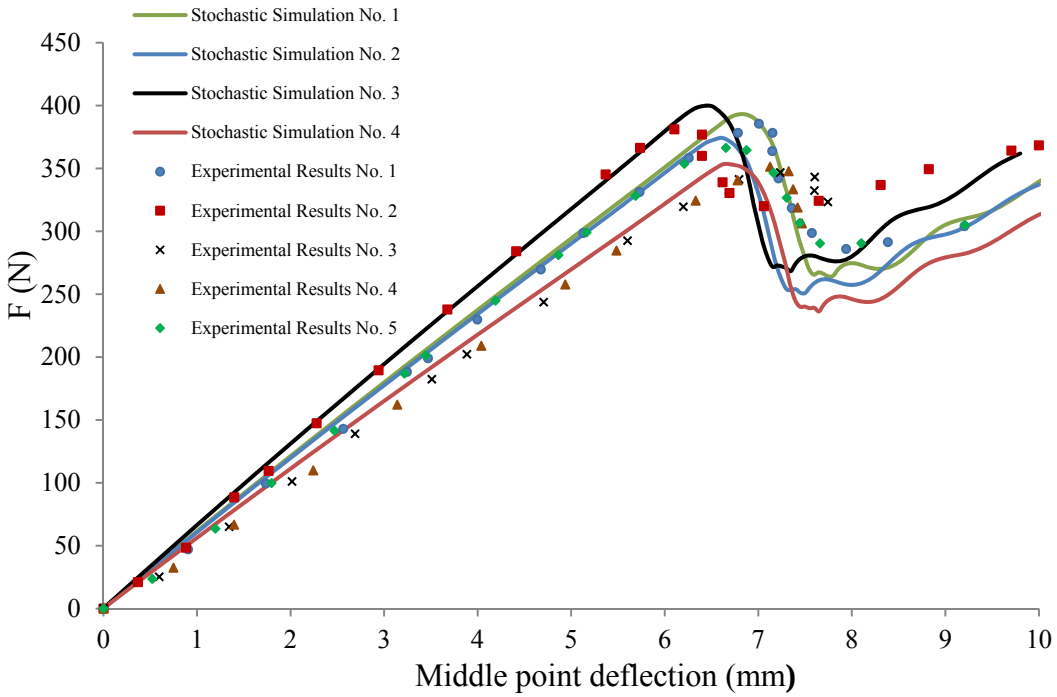

Figure 4-15 Comparison of stochastic measured and predicted force-displacement values in ENF tests on the PPS/Glass samples

As illustrated in Figure 4-15, the stochastic simulations of the ENF test have resulted in a great agreement with non-repeatable experimental data. In performed simulations, critical (opening) deflection varied due to the traction-separation law's dependency on the failure crack sliding displacement and, as illustrated, it also affects the variation of the maximum critical flexural load. Based on the observed trend in simulation data, it can be concluded that

the fiber bridging effect in ENF test has a minimal effect in global behaviour of the results. Figure 4-16 shows the XFEM model contours under different stages of delamination in ENF test. It should be added that from an application perspective, for forming processes of composite preparation, such as compression moulding set-up in Figure 1-10, mode II fracture would be more relevant due to sliding between layers of the laminate under the punch load.

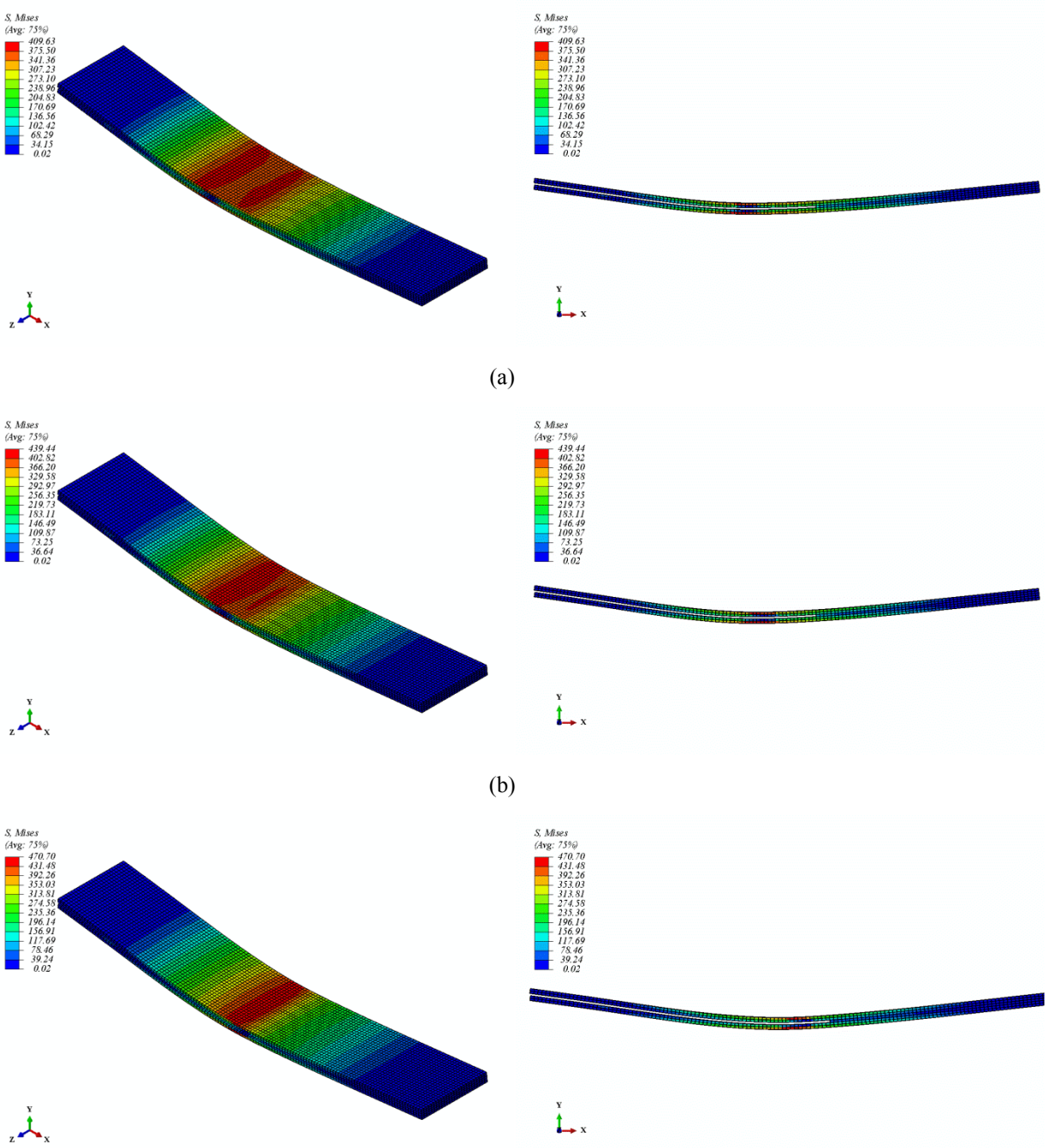

Figure 4-16 Stages of delamination propagation within the ENF numerical model: (a) Apex of rigid hardening in the process zone, (b) Initial stage of crack propagation, and (c) Extensive deterioration of material

4.6 Summary

In this chapter, different methods of fabricating PPS/Glass test samples were reviewed and their elastic mechanical properties were extracted. The stochastic nature of DCB and ENF tests on PPS/Glass composite was illustrated. This characteristic was next introduced into the XFEM numerical analysis by means of a random fracture energy toughness distribution. Failure crack opening/sliding displacements were employed to relate the fracture energy toughness randomness to the traction-separation law. In order to demonstrate the capability of the present method in capturing the DCB and ENF test results, several stochastic simulations were performed and the results were compared to experimental data.

5 Chapter: Conclusions and Future Work Recommendation

5.1 XFEM Model Development

A new framework was presented to numerically simulate the fracture behaviour of FRP composite materials and, more specifically, the unidirectional PPS/Glass laminates. For this purpose, the ABAQUS finite element package was utilized as a simulation engine. In order to extend the capability of ABAQUS in modeling crack and delamination contact interfaces in large delaminations, a user-element subroutine was developed to introduce nonlinear XFEM element properties including CZM and contact. In these elements, the right hand side vector and the stiffness matrix were defined and, according to the employed degrees of freedom, were assembled into the global system of equations. In addition, the stochastic fracture properties of the composite samples were adapted into the code to capture the randomness seen through non-repeatable test results. The model may be used with both implicit and explicit nonlinear solvers for both deterministic and stochastic simulations.

5.2 Performed Deterministic Simulations

Following earlier works in the literature, the performed benchmark deterministic simulations demonstrated the effectiveness of the combined XFEM - cohesive zone model (CZM) and contact interface modeling approach in 3D numerical analysis of mode I and II fracture mechanics of fiber reinforced composites in the presence of large deformation effects and interface material nonlinearity. Sets of sensitivity analysis were also performed to evaluate the effect of modeling parameters on the XFEM numerical predictions. For more reliable simulations, it was found that a minimum of two elements is required within the cohesive zone region (regardless of critical length) in front of the crack tip. On the other hand,

considering a very long cohesive zone would introduce a global softening of material into simulations and can lead to an underestimation of the peak opening force. A maximum of six elements with a fine mesh is recommended as the limit within the cohesive zone region for mode I fracture analysis of the studied unidirectional composites. It was also observed that reducing the penalty stiffness value in the traction-separation law improves the convergence of numerical simulations and reduces the mesh size sensitivity. However, using conventional FEM this can again cause a softening problem and reduce the peak opening force. The XFEM approach with embedded CZM was found to be less sensitive to the aforementioned effects, particularly when the penalty stiffness value is chosen arbitrarily within the range of transverse and longitudinal moduli of the composite. In the case of mode II fracture analysis, an increase in the penalty stiffness could cause extensive flexural deformation without any crack formation while a small value for the penalty stiffness may lead to a lower critical flexural force.

5.3 Performed Stochastic Simulations

For stochastic analysis, the prediction of fracture behaviour of fabricated unidirectional PPS/Glass composites was presented. DCB tests, both in the standard and continuous modes, were conducted for extracting the experimental material fracture properties along with their variation through test non-repeatabilities. Based on the experimental data and obtained x-ray images, it was concluded that fiber bridging was present in the specimens during delamination and the energy release rate can be a function of the crack length. In order to reproduce the experimental results with numerical simulations, under the stochastic behaviour of the material the bilinear traction-separation cohesive behaviour was applied within the framework

of nonlinear XFEM. It was found that the approach is capable of predicting delamination surfaces with the traction due to possible fiber bridging effects. To take the present stochastic material properties effect into account, even under a given crack length, the fracture energy toughness value was randomized using two different standard deviation methods. Specifically, applying the constant standard deviation method (i.e., using the overall standard deviation of the entire data sets) demonstrated a low variation of predicted/model values, but induced fewer numerical fluctuations in the continuous test mode. In contrast, considering a standard deviation as a function of crack length captured a wider range of experimental data points by increasing randomness effects in the fracture properties, though it induced some fluctuations in the numerical curves.

For the ENF test, performed to study the mode II fracture energy toughness of the same PPS/Glass samples, due to the abrupt nature of shear failure, capturing the dependency of the mode II fracture energy toughness on the crack length was not possible. Such failure behaviour, however, demonstrated a lower randomness as represented by more repeatable continuous mode test data. Therefore, the average fracture energy toughness in this mode was assumed to be independent of the crack length and was only affected by the standard deviation of the test results. The numerical simulation results were well-agreeing with the experimental ones and the variation of the failure deflection was captured by the stochastic XEM model.

5.4 Potential Future Work

Future works may be defined based on three different areas. First, improvements can be made to the FEM shell analysis by introducing a similar nonlinear XFEM into the standard shell

element formulation, employing the mass and damping matrices for dynamic analysis of fracture tests and applying different traction-separation laws for modeling different material types. Second, both DCB and ENF tests can be repeated with larger size specimens to capture the stabilizing regions of R-curves observed in experiments with longer delamination sizes. Such tests can help to scrutinize the stable and unstable nonlinear regions of fiber bridging. Third, other fracture tests such as the end loaded split (ELS), mixed-mode bending (MMB) and edge crack torsion (ECT) can be studied to verify the advantages of the XFEM method in modeling more complex fracture tests and potentially improving the traction-separation law application for such tests. Another significant aspect of stochastic modeling is to understand the effect of number of random simulations. A larger number of simulations would produce a more distinguished region of predictions between upper bond and lower bonds of data. Finally, more focus can be put on increasing the number of experimental repeats to gain a better estimation of deviation of data from mean values and hence to improve the reliability of the simulations. This can also include the introduction of a more precise random distribution of fracture properties, specifically by including a non-liner dependency of the fracture energy toughness, mean and standard deviation on the crack length via further experimentation and statistical analysis. Also, an integration of a microscopic analysis with a signal-to-noise ($G_{C(ave)}$/$G_{C(std)}$) based stochastic XFEM modeling framework can be worthwhile.

References

[1] Tuakta, Ch (2005) Use of fiber reinforced polymer composite in bridge structures. *University of Massachusetts Institute of Technology. USA*.

[2] Meier, U (2000) Advanced solution with composites in construction. *Proceeding of the international Conference on Composites in Construction*, (Figueiras, J, Juvandes, L, Faria, R, & Eds.), pp. 3-7.

[3] Mazumdar, S (2002) Composites manufacturing: materials, products and process engineering. *CRC Press*.

[4] Potluri, P, & Manan, A (2007) Mechanics of non-orthogonally interlaced textile composites. *Composites Part A: Applied Science and Manufacturing* 38:1216-1226.

[5] Keller, T (2001) Recent all-composites and hybrid fiber-reinforced polymer bridges and buildings. *Progress in Structural Engineering Materials* 3(2):132-140.

[6] Durham, SD, & Pagett, WJ (1997) Cumulative damage models for system failure with application to carbon fibers and composites. *American Statistical Association and the American Society for Quality Control* 39(1):34-44.

[7] Zhang, TF, Yang, XH, Sun, WSh, & Cai, ZJ (2011) A two-parameter model of FRP laminates stiffness reduction. *Advanced Materials Research* 236-238:1187-1194.

[8] Prasad, MS, Venkatesha, CS, & Jayaraju, T (2011) Experimental methods of determining fracture toughness of fiber reinforced polymer composites under various loading conditions. *Journal of Minerals & Materials Characterization & Engineering* 10(13):1263-1275.

[9] Sriramula, S, & Chryssanthopoulos, MK (2009) Quantification of uncertainty modelling in stochastic analysis of FRP composites. *Composites Part A: Applied Science and Manufacturing* 40(11):1673–1684.

[10] Baxter, SC, & Graham, LL (2000) Characterization of random composites using moving-window technique. *Journal of Engineering Mechanics* 126(4):389-397.

[11] Guilleminot, J, Soize, C, Kondo, D, & Binetruy, C (2008) Theoretical framework and experimental procedure for modelling mesoscopic volume fraction stochastic fluctuations in fiber reinforced composites. *International Journal of Solids and Structures* 45(21):5567–5583.

[12] Soize, C (2008) Tensor-valued random fields for meso-scale stochastic model of anisotropic elastic microstructure and probabilistic analysis of representative volume element size. *Probabilistic Engineering Mechanics* 23(2–3):307–323.

[13] Whitcomb, J, Srirengan, K, & Chapman, CS (1994) Evaluation of homogenization for global/local stress analysis of textile composites. *Collection of Technical Papers-AIAA/ASME/ASCE/AHS/ASC Structures, Structural Dynamics and Materials Conference* 3:1649-1663.

[14] Mehrez, L, Moens, D, & Vandepitte, D (2012) Stochastic identification of composite material properties from limited experimental databases, part I: Experimental database construction. *Mechanical Systems and Signal Processing* 27:471–483.

[15] Owen, MJ, Bishop, PT (1973) Critical stress intensity factors applied to glass reinforced polyester resins. *Journal of Composite Materials* 7:146-159.

[16] Gaggar, S, Broutman, LJ (1977) Fracture toughness of random glass fiber epoxy composites: an experimental investigation. *Flaw Growth and Fracture* ASTM STP 631:310-330.

[17] Mower, TM, Li, VC (1987) Fracture characterization of short fiber reinforced *thermoset* resin composites. *Engineering Fracture Mechanics* 26(4):593-603.

[18] ASTM-International (2001) Standard Test Method for Mode I, D 5528 01: interlaminar fracture toughness of unidirectional fiber-reinforced polymer matrix composites. West Conshohocken: *American Society for Testing and Materials*.

[19] O'Brien, TK (1998) Interlaminar fracture toughness: the long and winding road to standardization. *Composites Part B: Engineering* 29B(1): 57–62.

[20] Davies, P (1993) ESIS protocols for interlaminar fracture testing of composites. *France, IFREMER brochure*.

[21] Lee, SM (1993) An edge crack torsion method for mode III delamination fracture testing. *Journal of Composite Technology and Research* 15(3): 193-201.

[22] Hillerborg, A, Modeer, M, & Petersson, PE (1976) Analysis of crack formation and crack growth in concrete by means of fracture mechanics and finite elements. *Cement and Concrete Research* 6:773-782.

[23] Xu, XP, & Needleman, A (1994) Numerical simulations of fast crack growth in brittle solids. *Journal of the Mechanics and Physics of Solids* 42:1397-1434.

[24] Camacho, GT, & Ortiz, M, (1996) Computational modelling of impact damage in brittle materials. *International Journal of Solids and Structures* 33:2899-2938.

[25] Camanho, PP, Davila, CG, & De Moura, MF (2003) Numerical simulation of mixed-mode progressive delamination in composite materials. *Journal of Composite Materials*, 37:1415-24.

[26] Blackman, BRK, Hadavinia, H, Kinloch, AJ, & Williams, JG (2003) The use of a cohesive zone model to study the fracture of fiber composites and adhesively-bonded joints. *International Journal of Fracture* 119:25-46.

[27] Gao, YF, & Bower, AF (2004) A simple technique for avoiding convergence problems in finite element simulations of crack nucleation and growth on cohesive interfaces. *Modelling and Simulation in Materials Science and Engineering* 12:453-463.

[28] Segurado, TMJ, & LLorca, CTJ (2004) A new three-dimensional interface finite element to simulate fracture in composites. *International Journal of Solids and Structures* 41:2977-2993.

[29] Cox, B, & Yang, Q (2005) Cohesive models for damage evolution in laminated composites. *International Journal of Fracture*133:107-37.

[30] Nishikawa, M, Okabe, T, & Takeda, N (2007) Numerical simulation of interlaminar damage propagation in CFRP cross-ply laminates under transverse loading. *International Journal of Solids and Structures* 44:3101-3113.

[31] Belytschko, T, & Black, T (1999) Elastic crack growth in finite elements with minimal remeshing. *International Journal for Numerical Methods in Engineering* 45: 601-620.

[32] Moës, N, Dolbow, J, & Belytschko, T (1999) A finite element method for crack growth without remeshing. *International Journal for Numerical Methods in Engineering* 46: 131-150.

[33] Melenk, JM, & Babuška, I (1996) The partition of unity finite element method: basic theory and applications. *Computer Methods in Applied Mechanics and Engineering* 139: 289-314.

[34] Xiao, QZ, Karihaloo, BL, & Liu, XY (2006) Incremental-secant modulus iteration scheme and stress recovery for simulating cracking process in quasi-brittle materials using XFEM. *International Journal for Numerical Methods in Engineering* 69(12):2606-2635.

[35] Unger, JF, Eckardta, S, & Könke, C (2007) Modelling of cohesive crack growth in concrete structures with the extended finite element method. *Computer Methods in Applied Mechanics and Engineering* 196(41):4087-4100.

[36] Benvenuti, E (2008) A regularized XFEM framework for embedded cohesive interfaces. *Computer Methods in Applied Mechanics and Engineering* 197:4367-78.

[37] Sosa, JLC, & Karapurath, N (2012) Delamination modelling of GLARE using the extended finite element method. *Composites Science and Technology* 72:788–791.

[38] Kaw, AK (1997) Mechanics of composite materials. *New York: CRC Press*.

[39] Peng, X, & Cao, J (2002) A dual homogenization and finite element approach for material characterization of textile composites. *Composites Part B: Engineering* 33: 45–56.

[40] Baxevanakis, C, Jeulin, D, & Renard, J (1995) Fracture statistics of a unidirectional composite. *International Journal of Fracture* 73(2):149–181.

[41] Elleithy, R (2000) The hierarchical structure and flexure behavior of woven carbon fiber epoxy composite. *Polymer Composites* 27(5):716-723.

[42] Sejnoha, M, & Zeman, J (2008) Micromechanical modeling of imperfect textile composites. *International Journal of Engineering Science* 46(6):513-526.

[43] Trias, D, Costa, J, Mayugo, J, & Hurtado, J (2006) Random models versus periodic models for fiber reinforced composites. *Computational Materials Science* 38(2):316-324.

[44] Wang, ASD, Chou, PC, & Lei, SC (1984) A Stochastic Model for the Growth of Matrix Cracks in Composite Laminates. *Journal of Composite Materials* 18(3):239-254.

[45] Yushanov, S, & Bogdanovich, A (1998) Stochastic theory of composite materials with random waviness of the reinforcements. *International Journal of Solids and Structures* 35(22):2901-2930.

[46] Silberschmidt, VV (2005) Matrix cracking in cross-ply laminates: effect of randomness. *Composites Part A: Applied Science and Manufacturing* 36(2):129-135.

[47] Skordos, A, & Sutcliffe, M (2008) Stochastic simulation of woven composites forming. *Composites Science and Technology* 68(1):283-296.

[48] Ashcroft, IA, Khokar, ZR, & Silberschmidt VV (2012) Modelling the effect of micro-structural randomness on the mechanical response of composite laminates through the application of stochastic cohesive zone elements. *Computational Materials Science* 52(1):95–100.

[49] Espinosa, HD, Dwivedi, S, & Lu, HC (2000) Modeling impact induced delamination of woven fiber reinforced composites with contact/cohesive laws. *Computer Methods in Applied Mechanics and Engineering* 183:259-290.

[50] Turon, A, Da'vila, CG, Camanho, PP, & Costa, J (2007) An engineering solution for mesh size effects in the simulation of delamination using cohesive zone models. *Engineering Fracture Mechanics*, 74:1665-1682.

[51] Harper, P, & Hallett, SR (2008) Cohesive zone length in numerical simulations of composite delamination. *Engineering Fracture Mechanics*, 75(16):4774-4792.

[52] Barbieri, E, & Meo, M (2009) A mesh-free penalty-based approach to delamination in composites. *Composites Science and Technology* 69(13):2169-2177.

[53] Khoei, AR, Biabanaki, SOR, & Anahid, M (2009) A Lagrangian extended finite element method in modeling large plasticity deformations and contact problems. *International Journal of Mechanical Sciences* 51(5):384-401.

[54] Bhattacharyya, D, Bowis, M, & Jayaraman, K (2003) Thermoforming woodfibre–polypropylene composite sheets. *Composites Science and Technology* 63(3):353-365.

[55] ASTM-International (2011) Test Method D 4762 11A: Standard Guide for Testing Polymer Matrix Composite Materials. West Conshohocken: *American Society for Testing and Materials*.

[56] ASTM-International (2011) Test Method D 3039/D 3039M - 00: Standard Test Method for Tensile Properties of Polymer Matrix Composite. West Conshohocken: *American Society for Testing and Materials*.

[57] ASTM-International (2011) Test Method D 7617/7617M 11: Standard Test Method for Transverse Shear Strength of Fiber-reinforced Polymer Matrix Composite Bars. West Conshohocken: *American Society for Testing and Materials*.

[58] Bisby, LA, & Fitzwilliam, J (2006) An introduction to FRP composites for construction. *ISIS, A Canadian Network of Centres of Excellence*.

[59] Hellen, K (1984) Introduction to Fracture Mechanics. *McGraw-Hill, New York*.

[60] Westergaard, HM (1939) Bearing pressures and cracks. *Journal of Applied Mechanics.*

[61] Wells, AA (1961) Unstable crack propagation in metals: cleavage and fast fracture. *Proceedings of the Crack Propagation Symposium*, Paper 84.

[62] Rice, JR (1968) Path-independent integral and the approximate analysis of strain concentration by notches and cracks. *Journal of Applied Mechanics*, *Transactions ASME* 35 (2):379–386.

[63] Erdogan, F, & Sih, GC (1963) On the crack extension in plane loading and transverse shear. *Journal of Basic Engineering* 85:519-527.

[64] Hoffman, O (1967) The brittle strength of orthotropic materials. *Journal of Composite Materials* 1(2):200-206.

[65] Tsai, SW (1965) Strength characteristics of composite materials. NASA CR-224.

[66] Tsai, SW, & Wu, EM (1971) A general theory of strength for anisotropic materials. *Journal of Composite Materials* 5(1):58-80.

[67] Hashin, Z (1980) Failure criteria for unidirectional fiber composites. *Journal of Applied Mechanics* 47(2):329-334.

[68] Gdoutos, EE (2005) Fracture mechanics: An introduction. *Springer, Netherland*s.

[69] Lekhnitskii, SG (1963) Theory of an anisotropic elastic body. *San Francisco, Holden-Day*.

[70] Sih, GC, Paris, PC, & Irwin, GR (1965) On cracks in rectilinearly anisotropic bodies. *International Journal of Fracture Mechanics*. 1:189–203.

[71] Asadpoure, A, & Mohammadi, S (2007) Developing new enrichment functions for crack simulation in orthotropic media by the extended finite element method. *International Journal for Numerical Methods in Engineering*. 69:2150-2172.

[72] Dolbow, J, Moës, N, & Belytschko, T (2001) An extended finite element method for modeling crack growth with frictional contact. *Computational Methods in Applied Mechanics and Engineering*, 190:6825-6846.

[73] Kim, JH, & Paulino, GH (2003) The interaction integral for fracture of orthotropic functionally graded materials: evaluation of stress intensity factors. *International Journal of Solids and Structures,* 40(1):3967-4001.

[74] Irwin, GR (1961) Plastic zone near a crack and fracture toughness. *Proceedings, Seventh Sagamore Ordnance Materials Conference, Syracuse University Research Institute, 1:4-63.*

[75] Dugdale, DS (1960) Yielding in steel sheets containing slits. *Journal of the Mechanics and Physics of Solids,* 8(2):100-104.

[76] Barenblatt, GI (1962) The mathematical theory of equilibrium cracks in brittle fracture. *Advances in Applied Mechanics*, 7(1):55-129.

[77] Eshelby, JD (1956) The continuum theory of lattice defects. *Solid State Physics*, 3(1):79-144.

[78] Motamedi, D, & Mohammadi, S (2010) Dynamic crack propagation analysis of orthotropic media by the extended finite element method. *International Journal of Fracture*, 161(1):21-39.

[79] Motamedi, D, & Mohammadi, S (2011) Fracture analysis of composites by time independent moving-crack orthotropic XFEM. *International Journal of Mechanical Sciences*, 54(1):20–37.

[80] Aliabadia, MH, & Sollero, P (1998) Crack growth analysis in homogeneous orthotropic laminates. *Composites Science and Technology*, 58(10):1697–1703.

[81] Wu, KC (2000) Dynamic crack growth in anisotropic material. *International Journal of Fracture*, 106:1-12.

[82] Dongye, C, & Ting, TCT (1989) Explicit expressions of Barnett-Lothe tensors and their associated tensors for orthotropic materials. *Quarterly of Applied Mathematics*, 47: 723-734.

[83] Needleman, A (1987) A continuum model for void nucleation by inclusion debonding. *Journal of Applied Mechanics*, 54(3):525-531.

[84] Tvergaard, V, & Hutchinson, JW (1992) The relation between crack growth resistance and fracture process parameters in elastic–plastic solids. *Journal of the Mechanics and Physics of Solids*, 40(6):1377-1397.

[85] Cui, W, & Wisnom, MR (1993) A combined stress-based and fracture-mechanics based model for predicting delamination in composites. *Composites*, 24(6):467-474.

[86] Geubelle, PH, & Baylor, JS (1998) The impact-induced delamination of laminated composites: A 2D simulation. *Composites Part B: Engineering*, 29(5):589-602.

[87] Ortiz, M, & Pandolfi, A (1999) Finite-deformation irreversible cohesive elements for three-dimensional crack-propagation analysis. *International Journal of Numerical Methods and Engineering*, 44:1267-1282.

[88] Mi, U, Crisfield, MA, & Davies, GAO (1998) Progressive delamination using interface elements. *Journal of Composite Materials*, 32(14):1246-1272.

[89] Alfano, G, & Crisfield, MA (2001) Finite element interface models for the delamination analysis of laminated composites: mechanical and computational issues. *International Journal for Numerical Methods in Engineering*, 50:1701-1736.

[90] Fan, C, Ben Jar, PY, & Cheng ,JJR (2008) Cohesive zone with continuum damage properties for simulation of delamination development in fiber composites and failure of adhesive joints. *Engineering Fracture Mechanics*, 75:3866-3880.

[91] Planas, J, & Elices, M (1991) Nonlinear fracture of cohesive materials. *International Journal of Fracture*, 51:139-57.

[92] Jin, ZH, & Sun, CT (2005) Cohesive zone modeling of interface fracture in elastic bi-materials. *Engineering Fracture Mechanics*, 72(12):1805-1817.

[93] Yang, QD, Cox, BN, Nalla, RK, & Ritchie, RO (2006) Fracture length scales in human cortical bone: the necessity of nonlinear fracture models. *Biomaterials*, 27:2095-113.

[94] Carpinteri, A, Cornetti, P, Barpi, F, & Valente, S (2003) Cohesive crack model description of ductile to brittle size-scale transition: dimensional analysis vs. renormalization group theory. *Engineering Fracture Mechanics*, 70:1809-939.

[95] Giner, E, Sukumar, N, Tarancon, JE, & Fuenmayor, FJ (2009) An ABAQUS implementation of the extended finite element method. *Engineering Fracture Mechanics*, 76(3):347‑68.

[96] SIMULIA (2008) ABAQUS 6.8-1 Documentation, *Rhode Island*, USA.

[97] ASTM-International (2001) Standard Test Method for Mode I, D 5528 01: interlaminar fracture toughness of unidirectional fiber-reinforced polymer matrix composites. West Conshohocken: *American Society for Testing and Materials*.

[98] Fukunaga, H, Tsu-Wei, C, Peters, PWM, & Schulte, K (1984) Probabilistic failure strength analysis of graphite epoxy cross ply laminates. *Journal of Composite Materials*, 18(4):339-56.

[99] Bulsara, VN, Talreja, R, & Qu, J (1999) Damage initiation under transverse loading of unidirectional composites with arbitrarily distributed fibers. *Composites Science and Technology*, 59(5):673-82.

[100] Silberschmidt, VV (2006) Effect of micro-randomness on macroscopic properties and fracture of laminates. *Journal of Material Science*, 41(20):6768-776.

[101] Spearing, SM, & Evans, AG (1992) The role of fiber bridging in the delamination resistance of fiber-reinforced composites. *Acta Metallurgica et Materialia*, 40(9):2191-9.

[102] Tamuzs, V, Tarasovs, S, & Vilks, U (2001) Progressive delamination and fiber bridging modeling in double cantilever beam composite specimens. *Engineering Fracture Mechanics*, 68(5):513‑25.

[103] Nairn, J (2009) Analytical and numerical modeling of R curves for cracks with bridging zones. *International Journal of Fracture*, 155(2):167‑81.

[104] Airoldi, A, & Dávila, CG (2012) Identification of material parameters for modeling delamination in presence of fiber bridging. *Composite Structures*, 94:3240-9.

[105] TENCATE ADVANCED COMPOSITES USA, INC. (www.tencate.com)

[106] Khokhar, ZR, Ashcroft, IA, & Silberschmidt, VV (2009) Simulations of delamination in CFRP laminates: Effect of microstructural randomness. *Computational Materials Science*, 46(2):607-13.

Appendices

Appendix A: ABAQUS User-element Subroutine for Nonlinear XFEM Analysis

```
      SUBROUTINE UEL(RHS,AMATRX,SVARS,ENERGY,NDOFEL,NRHS,NSVARS,
     1 PROPS,NPROPS,COORDS,MCRD,NNODE,U,DU,V,A,JTYPE,TIME,DTIME,
     2 KSTEP,KINC,JELEM,PARAMS,NDLOAD,JDLTYP,ADLMAG,PREDEF,NPREDF,
     3 LFLAGS,MLVARX,DDLMAG,MDLOAD,PNEWDT,JPROPS,NJPROP,PERIOD)
C
      INCLUDE 'ABA_PARAM.INC'

            PARAMETER ( ZERO = 0.D0, HALF = 0.5D0,
     +     ONE = 1.D0, SEVEN=7.0D0, EIGHT=8.0D0 )
C
      DIMENSION RHS(NDOFEL,*),AMATRX(NDOFEL,NDOFEL),PROPS(*),
     1 SVARS(*),ENERGY(8),COORDS(MCRD,NNODE),U(NDOFEL),
     2 DU(NDOFEL,*),V(NDOFEL),A(NDOFEL),TIME(2),PARAMS(*),
     3 JDLTYP(MDLOAD,*),ADLMAG(MDLOAD,*),DDLMAG(MDLOAD,*),
     4 PREDEF(2,NPREDF,NNODE),LFLAGS(*),JPROPS(*)
C
C
      REAL*8 GAUSSPOINT(140,MCRD),
     +       XCR(MCRD+1,MCRD),
     +       dNdx(NNODE,MCRD+1),
     +       U_MIDPNT(NNODE,MCRD),
     +       B(MCRD*MCRD, NDOFEL),
     +       DNDXi(NNODE,MCRD),
     +       C_COORDS(NNODE,MCRD),
     +       Gs(2*MCRD,MCRD*MCRD),
     +       U_Ms(MCRD*MCRD,MCRD*MCRD),
     +       C(2*MCRD,2*MCRD),
     +       Dep(MCRD,MCRD),
     +       QT(MCRD,MCRD),
     +       QTT(MCRD,MCRD),
     +       QR(MCRD,MCRD),
     +       QRT(MCRD,MCRD),
     +       DGep(MCRD,MCRD),
     +       FB(MCRD,MCRD),
     +       FBT(MCRD,MCRD),
     +       STRGLB(MCRD,MCRD),
     +       STRGLOB(MCRD,MCRD),
     +       dUdx(MCRD,MCRD),
     +       Nx(1,NNODE),
     +       GWEIGHT(140),
     +       FF(MCRD*MCRD),
     +       STRSG(MCRD*MCRD),
     +       COOR(MCRD),
     +       DLTU(MCRD),
     +       dV(MCRD)
C     USER-ELEMNT ARRAYS
C     GENERAL ELEMENT VALUES
C     GAUSS INTEGRATION VARIABLES (3 INTEG POINT)
C     ARRAYS FOR 3D ELEMENT
      REAL*8 U_PHI(NNODE)
      REAL*8 UNeg(MCRD),
     +       UPos(MCRD),
```

```
     +      UNg(MCRD),
     +      UPs(MCRD),
     +      U1(MCRD),
     +      UBAS(NDOFEL),
     +      EC(2*MCRD),
     +      STRS(2*MCRD),
     +      BTSTRS(NDOFEL),
     +      Trct(MCRD),
     +      LHSC(NDOFEL),
     +      RHSC(NDOFEL)
      REAL*8 BT(NDOFEL,MCRD*MCRD),
     +      GsT(MCRD*MCRD,2*MCRD)
      REAL*8 JACB(MCRD,MCRD),
     +      INVJACB(MCRD,MCRD),
     +      INVFB(MCRD,MCRD),
     +      INVFBT(MCRD,MCRD),
     +      IUNIT(MCRD,MCRD),
     +      DGBc(MCRD,NDOFEL),
     +      BTGT(NDOFEL,2*MCRD),
     +      GB(2*MCRD,NDOFEL),
     +      MsB(MCRD*MCRD,NDOFEL),
     +      BTMsB(NDOFEL,NDOFEL),
     +      BcTDGBc(NDOFEL,NDOFEL),
     +      KMAT(NDOFEL,NDOFEL),
     +      KGEM(NDOFEL,NDOFEL),
     +      KCON(NDOFEL,NDOFEL)
      REAL*8 Bc(MCRD,NDOFEL),
     +      BcT(NDOFEL,MCRD),
     +      CSTRN(MCRD,MCRD),
     +      EEC(MCRD,MCRD),
     +      BcRes(NDOFEL,MCRD)
      REAL*8 Xi, Yi, Zi, WEIGHT, ENRCOH, ENRJC,
     +      E11, E22, E33, G12, G23, G31,
     +      Nu12, Nu21, Nu23, Nu32, Nu31, Nu13,
     +      DETFB, DETJ, nu, uacrt, Jsdv,
     +      HPOINT, ENRELM, NNINT, KPEN,TMAX,
     +      Jcrt, Dmg1, Dmg2, Dmg3
C
      INTEGER COUNT1, COUNT2, INTP, IINTP, I, J, K, L, M, N
C
C     ********************************************************************************
C     *** INITIALISATION: IMPORTANT!! FORTRAN DOES NOT PUT ZEROS IN THERE
AUTOMATICALLY ***
C     ********************************************************************************
C     OPEN LEVEL-SET VALUES FROM PRE-PROCESSING
      OPEN(16, FILE='C:/ABAQUS-Matlab/IOstat
     +/philvlst.dat',STATUS='OLD')
C
      NINTP = 24        ! Number of integration points
            uacrt  = PROPS(1) ! Crack Lenght
      dV(1) = PROPS(2)  ! Material Initiation Opening Failure
      dV(2) = PROPS(3)  ! Material Final Opening Failure
      E11   = PROPS(4)  ! Material Constant
      E22   = PROPS(5)  ! Material Constant
      E33   = PROPS(6)  ! Material Constant
      G12   = PROPS(7)  ! Material Constant
      G23   = PROPS(8)  ! Material Constant
      G31   = PROPS(9)  ! Material Constant
      Nu12  = PROPS(10) ! Material Constant
```

```
      Nu23  = PROPS(11) ! Material Constant
      Nu31  = PROPS(12) ! Material Constant
            KPEN  = PROPS(13) ! Material Constant
            Jsdv  = PROPS(14)  ! G Standard Deviation
C
C     CALCULATING THE TRACTION-SEPARATION CONSTANT
            TMAX = KPEN*dV(1)
            Jcrt = TMAX*dV(2)/2
      WIDTH = 1 ! Element Tickness
C     **********************************
C     *** ZERO THE REQUIRED MATRICES ***
C     **********************************
      ENRELM  = 0.0
C
      DO I = 1, NNODE
        Nx(1,I) = 0.0
        U_PHI(I)  = 0.0
        DO J = 1, MCRD+1
          dNdx(I,J) = 0.0
        ENDDO
      ENDDO
C
      DO J = 1, MCRD
        COOR(J) = 0.0
      ENDDO
C
      DO I = 1, 2*MCRD
        DO J = 1, 2*MCRD
          C(I,J) = 0.0
        ENDDO
      ENDDO
C
      DO I = 1, MCRD*MCRD
        DO J = 1, NDOFEL
          B(I,J)  = 0.0
          BT(J,I) = 0.0
        ENDDO
      ENDDO
C
      DO I = 1, 2*MCRD
        DO J = 1, MCRD*MCRD
          Gs(I,J) = 0.0
                        GsT(J,I) = 0.0
        ENDDO
      ENDDO
C
      DO I = 1, NNODE
        DO J = 1, MCRD
          C_COORDS(I,J) = 0.0
             ENDDO
          ENDDO
C
      DO I = 1, MCRD
        DO J = 1, MCRD
               IUNIT(I,J)   = 0.0
          JACB(I,J)    = 0.0
          INVJACB(I,J) = 0.0
          Dep(I,J)     = 0.0
          DGep(I,J)    = 0.0
```

```
          QT(I,J)      = 0.0
          QTT(I,J)     = 0.0
          QR(I,J)      = 0.0
          QRT(I,J)     = 0.0
        ENDDO
      ENDDO
C
      DO I = 1, NNODE
        DO J = 1, MCRD
          U_MIDPNT(I,J) = 0.0
        ENDDO
      ENDDO
C
      DO I = 1, NSVARS
        SVARS(I) = 0.0
      ENDDO
C
      DO I = 1, NDOFEL
        DO J = 1, NDOFEL
          AMATRX(I,J) = 0.0
                KGEM(I,J) = 0.0
                KMAT(I,J) = 0.0
                KCON(I,J) = 0.0
        ENDDO
      ENDDO
C
      DO I = 1, NDOFEL
        RHS(I,1) = 0.0
        RHSC(I) = 0.0
        LHSC(I) = 0.0
        UBAS(I) = 0.0
      ENDDO
C     **********************
C     *** DUMMY ARRAYS ***
C     **********************
      DO I = 1, MCRD
        IUNIT(I,I) = 1.0
      ENDDO
            INTS  = 1  ! Integration point scheme (1: gauss)
      STYPE = 1  ! Element type (1: B8, 2: T4)
C     ****************
C     *** HOOK LAW ***
C     ****************
      Nu21 = Nu12*E22/E11
      Nu32 = Nu23*E33/E22
      Nu13 = Nu31*E11/E33
      Delt = (1-Nu12*Nu21-Nu23*Nu32-Nu13*Nu31-2*Nu12*Nu23*Nu31)
C
      C(1,1) = E11*(1-Nu32*Nu23)/Delt
      C(1,2) = E11*(Nu21+Nu31*Nu23)/Delt
      C(1,3) = E11*(Nu31+Nu21*Nu32)/Delt
      C(2,1) = E22*(Nu12+Nu13*Nu23)/Delt
      C(2,2) = E22*(1-Nu13*Nu31)/Delt
      C(2,3) = E22*(Nu32+Nu31*Nu12)/Delt
      C(3,1) = E33*(Nu13+Nu12*Nu23)/Delt
      C(3,2) = E33*(Nu23+Nu13*Nu21)/Delt
      C(3,3) = E33*(1-Nu12*Nu21)/Delt
      C(4,4) = G12/2
      C(5,5) = G23/2
```

```
      C(6,6) = G31/2
C     ****************************************
C     *** FINDING DEFORM SHAPE OF COORDINATES ***
C     ****************************************
      DO I = 1, NNODE
        DO J = 1, MCRD
          C_COORDS(I,J) = COORDS(J,I) + U(2*MCRD*(I-1)+J)
        ENDDO
      ENDDO
C     ************************************************
C     *** FINDING REFERENCE COORDINATE DEFORMATION ***
C     ************************************************
      DO I = 1, NDOFEL
        U(I) = U(I)  - DU(I,1)
      ENDDO
C     ************************
C     *** CALLING LEVEL SET ***
C     ************************
      CALL LVLSETRDR(U_PHI,JELEM,NNODE) ! READ THE Level-Set FROM MATLAB
C     ********************************************************
C     *** CALLING THE LOCAL CRACK'S PLANE IN EACH ELEMENT ***
C     ********************************************************
      CALL MIDPLNFIND(NNINT,U_MIDPNT,QT,U_PHI,COORDS,NNODE,MCRD)
C
      DO I = 1, MCRD
        DO J = 1, MCRD
          QTT(I,J) = QT(J,I)
        ENDDO
      ENDDO
C     *********************************
C     *** CALLING GAUSS COORDINATES ***
C     *********************************
      CALL SUBTGAUSS(GAUSSPOINT,GWEIGHT,NNODE,MCRD)
C     ***************************************
C     *** LOOKING FOR OPENING DISPLACEMENT ***
C     ***************************************
      COUNT1 = 0
      COUNT2 = 0
C
      DO I = 1, MCRD
        UPos(I) = 0.0
        UNeg(I) = 0.0
        UPs(I)  = 0.0
        UNg(I)  = 0.0
      ENDDO
C     ***********************************
C     *** LOOP OVER INTEGRATION POINTS ***
C     ***********************************
      DO INTP = 1, NINTP
        HPOINT  = 0.0
        DO I = 1, MCRD
          U1(I)   = 0.0
          DLTU(I) = 0.0
        ENDDO
C
        COOR(1) = GAUSSPOINT(INTP,1)
        COOR(2) = GAUSSPOINT(INTP,2)
        COOR(3) = GAUSSPOINT(INTP,3)
        WEIGHT  = GWEIGHT(INTP)
```

```
C     **********************************
C     *** CALLING THE SHAPE FUNCTIONS ***
C     **********************************
      CALL LAGRANGEBASIS(COOR,Nx,dNdx,NNODE,MCRD)
C     **********************************
C     *** CALCULATING Gpt-LEVEL SET ***
C     **********************************
      DO I = 1, NNODE
        HPOINT = HPOINT + U_PHI(I)*dNdx(I,4)/ABS(U_PHI(I))
      ENDDO
            IF (HPOINT .GT. 0.0) THEN
              HPOINT = 1.0
            ELSEIF (HPOINT .LT. 0.0) THEN
        HPOINT = -1.0
            ELSE
              HPOINT = 0.01
              WEIGHT = 0.0
            ENDIF
C     ******************************************
C     *** CHECKING FOR Gpt WITHIN CONTACTBOUND ***
C     ******************************************
      DO I = 1, NNODE
        DO J = 1, MCRD
          U1(J) = U1(J) + dNdx(I,4)*U(6*(I-1)+J)
     +       + (HPOINT - ABS(U_PHI(I))/U_PHI(I))*
     +       (dNdx(I,4)*U(6*(I)+J-3))
        ENDDO
      ENDDO
C
      IF (HPOINT .LT. 0.0)THEN
        COUNT1  = COUNT1  + 1
        UNeg(1) = UNeg(1) + U1(1)
        UNeg(2) = UNeg(2) + U1(2)
        UNeg(3) = UNeg(3) + U1(3)
      ELSE
        COUNT2  = COUNT2  + 1
        UPos(1) = UPos(1) + U1(1)
        UPos(2) = UPos(2) + U1(2)
        UPos(3) = UPos(3) + U1(3)
      ENDIF
C
    ENDDO
    DO I = 1, MCRD
      DO J = 1, MCRD
        UPs(I) = UPs(I) + QT(I,J)*UPos(J)/COUNT2
        UNg(I) = UNg(I) + QT(I,J)*UNeg(J)/COUNT1
      ENDDO
    ENDDO
C
    DLTU(1) = UPs(1) - UNg(1)
    DLTU(2) = UPs(2) - UNg(2)
    DLTU(3) = UPs(3) - UNg(3)
c
C     ******************************************
C     *** FORMING STIFFNESS AND RESIDUAL MATRIX ***
C     ******************************************
C
C     ****************************
C     *** CALLING ELAST-PLAST RELATIONSHIP ***
```

```
C     ******************************
      DO I = 1,MCRD
        DO J = 1,MCRD
          DGep(I,J) = 0.0
        ENDDO
      ENDDO
C
      CALL ELSPLC(Dep,DLTU,dV,uacrt,C,MCRD,ENRELM,JTYPE,KPEN,
     1          Dmg1, Dmg2, Dmg3)
C
C     ASSIGNING DAMAGE INDECES AND CRACK OPENING DISPLACEMENT TO USER-VARIABLES
C
      SVARS(1)=Dmg1
      SVARS(2)=Dmg2
      SVARS(3)=Dmg3
      SVARS(4)=DLTU(1)
      SVARS(5)=DLTU(2)
      SVARS(6)=DLTU(3)
C
C     TRANSFORIMG THE ELASTIC-PLASTIC RELATIONSHIP INTO LOCAL CRACK PLANE
C
      DO I = 1, MCRD
        DO J = 1, MCRD
          DO K = 1, MCRD
            DO L = 1, MCRD
              DGep(I,J) = DGep(I,J) + QTT(I,K)*Dep(K,L)*QT(L,J)
            ENDDO
          ENDDO
        ENDDO
      ENDDO
C
C     ***********************************
C     *** LOOP OVER INTEGRATION POINTS ***
C     ***********************************
            DO I = 1, NDOFEL
        DO J = 1, NDOFEL
                BTMsB(I,J) = 0.0
              ENDDO
            ENDDO
C
      DO IINTP = 1, NINTP
        COOR(1) = GAUSSPOINT(IINTP,1)
        COOR(2) = GAUSSPOINT(IINTP,2)
        COOR(3) = GAUSSPOINT(IINTP,3)
        WEIGHT  = GWEIGHT(IINTP)
C     ***********************************
C     *** CALLING THE SHAPE FUNCTIONS ***
C     ***********************************
        CALL LAGRANGEBASIS(COOR,Nx,dNdx,NNODE,MCRD)
        Xi = COOR(1)
        Yi = COOR(2)
        Zi = COOR(3)
              DO I = 1, MCRD
          DO J = 1, MCRD
            JACB(I,J) = 0.0
          ENDDO
        ENDDO
C     ******************************
C     *** FORMING JACOBIAN MATRIX ***
```

```
C     ******************************
      DO I = 1, MCRD
        DO J = 1, MCRD
          DO K = 1, NNODE
            JACB(I,J) = JACB(I,J) + COORDS(I,K)*dNdx(K,J)
          ENDDO
        ENDDO
      ENDDO
C
      DETJ = JACB(1,1)*(JACB(2,2)*JACB(3,3) - JACB(2,3)*JACB(3,2)) -
     +       JACB(1,2)*(JACB(2,1)*JACB(3,3) - JACB(3,1)*JACB(2,3)) +
     +       JACB(1,3)*(JACB(2,1)*JACB(3,2) - JACB(2,2)*JACB(3,1))
      IF (DETJ .LT. 0.0) THEN
        DETJ = (-1)*DETJ
      ENDIF
      INVJACB(1,1) = (JACB(2,2)*JACB(3,3) - JACB(2,3)*JACB(3,2))/DETJ
      INVJACB(1,2) = (JACB(1,3)*JACB(3,2) - JACB(1,2)*JACB(3,3))/DETJ
      INVJACB(1,3) = (JACB(1,2)*JACB(2,3) - JACB(1,3)*JACB(2,2))/DETJ
      INVJACB(2,1) = (JACB(2,3)*JACB(3,1) - JACB(2,1)*JACB(3,3))/DETJ
      INVJACB(2,2) = (JACB(1,1)*JACB(3,3) - JACB(1,3)*JACB(3,1))/DETJ
      INVJACB(2,3) = (JACB(1,3)*JACB(2,1) - JACB(1,1)*JACB(2,3))/DETJ
      INVJACB(3,1) = (JACB(2,1)*JACB(3,2) - JACB(2,3)*JACB(3,1))/DETJ
      INVJACB(3,2) = (JACB(1,2)*JACB(3,1) - JACB(1,1)*JACB(3,2))/DETJ
      INVJACB(3,3) = (JACB(2,2)*JACB(1,1) - JACB(2,1)*JACB(1,2))/DETJ
C     ******************************
C     *** FORMING DERIVATIES dN/dx ***
C     ******************************
      DO I = 1, NNODE
        DO J = 1, MCRD
          DNDXi(I,J) = 0.0
        ENDDO
      ENDDO
C
      DO I = 1, NNODE
        DO J = 1, MCRD
          DO K = 1, MCRD
            DNDXi(I,J) = DNDXi(I,J) + dNdx(I,K)*INVJACB(K,J)
          ENDDO
        ENDDO
      ENDDO
C     ******************************
C     *** CALCULATING B-LEVEL SET ***
C     ******************************
      HPOINT = 0.0
            DO I=1,MCRD
              DO K=1,MCRD
          dUdx(I,K)=0.0
        ENDDO
      ENDDO
C
            DO I=1,MCRD
              DO K=1,MCRD
                DO J=1,NNODE
                  dUdx(I,K)=dUdx(I,K)+DNDXi(J,K)*U(6*(J-1)+I)
                ENDDO
              ENDDO
            ENDDO
C     ******************************
C     *** CALCULATING Gpt-LEVEL SET ***
```

```
C     ********************************
      DO I = 1, NNODE
        HPOINT = HPOINT + U_PHI(I)*dNdx(I,4)/ABS(U_PHI(I))
      ENDDO
            IF (HPOINT .GT. 0.0) THEN
              HPOINT = 1.0
            ELSEIF (HPOINT .LT. 0.0) THEN
        HPOINT = -1.0
            ELSE
              HPOINT = 0.01
              WEIGHT = 0.0
            ENDIF
      DO I=1,MCRD
               DO K=1,MCRD
                 DO J=1,NNODE
                   dUdx(I,K) = dUdx(I,K)+(HPOINT-ABS(U_PHI(I))/U_PHI(I))*
     +                DNDXi(J,K)*U(6*(J-1)+I+MCRD)
                 ENDDO
               ENDDO
            ENDDO
C     ************************
C     *** FORMING B MATRIX ***
C     ************************
      DO I = 1, MCRD*MCRD
        DO J = 1, NDOFEL
          B(I,J)  = 0.0
          BT(J,I) = 0.0
        ENDDO
      ENDDO
C
      CALL GRADB(B,DNDXi,HPOINT,U_PHI,NNODE,MCRD,NDOFEL)
C
      BT = TRANSPOSE(B)
C
            DO I = 1, MCRD*MCRD
        FF(I) = 0.0
      ENDDO
      DO I = 1, 2*MCRD
        EC(I)=0.0
      ENDDO
C
      DO I = 1, MCRD
               DO J = 1, MCRD
                 FB(I,J) = 0.0
                 FBT(I,J) = 0.0
               ENDDO
            ENDDO
C
      FF = MATMUL(B,U)
C
      dUdx(1,1) = FF(1)
      dUdx(2,1) = FF(2)
      dUdx(3,1) = FF(3)
      dUdx(1,2) = FF(4)
      dUdx(2,2) = FF(5)
      dUdx(3,2) = FF(6)
      dUdx(1,3) = FF(7)
      dUdx(2,3) = FF(8)
      dUdx(3,3) = FF(9)
```

```
C
C     ***********************************************
C     *** FORMING  GREEN-LAGRANGIAN & LARGE STRAINS  ***
C     ***********************************************
C
      DO I = 1, MCRD*MCRD
        IF (I .EQ. 1 .OR. I .EQ. 5 .OR. I .EQ. 9) THEN
          FF(I) = FF(I) + 1.0
        ENDIF
      ENDDO
C
      FB(1,1) = FF(1)
      FB(2,1) = FF(2)
      FB(3,1) = FF(3)
      FB(1,2) = FF(4)
      FB(2,2) = FF(5)
      FB(3,2) = FF(6)
      FB(1,3) = FF(7)
      FB(2,3) = FF(8)
      FB(3,3) = FF(9)
C     ******************************
C     *** FORMING INVF & GRADF    ***
C     ******************************
      DO I = 1, MCRD
        DO J = 1, MCRD
          INVFB(I,J) = 0.0
        ENDDO
      ENDDO
      DETFB = FB(1,1)*(FB(2,2)*FB(3,3) - FB(2,3)*FB(3,2)) -
     +        FB(1,2)*(FB(2,1)*FB(3,3) - FB(3,1)*FB(2,3)) +
     +        FB(1,3)*(FB(2,1)*FB(3,2) - FB(2,2)*FB(3,1))
      IF (DETFB .LT. 0.0) THEN
        DETFB = (-1)*DETFB
      ENDIF
      INVFB(1,1) = (FB(2,2)*FB(3,3) - FB(2,3)*FB(3,2))/DETFB
      INVFB(1,2) = (FB(1,3)*FB(3,2) - FB(1,2)*FB(3,3))/DETFB
      INVFB(1,3) = (FB(1,2)*FB(2,3) - FB(1,3)*FB(2,2))/DETFB
      INVFB(2,1) = (FB(2,3)*FB(3,1) - FB(2,1)*FB(3,3))/DETFB
      INVFB(2,2) = (FB(1,1)*FB(3,3) - FB(1,3)*FB(3,1))/DETFB
      INVFB(2,3) = (FB(1,3)*FB(2,1) - FB(1,1)*FB(2,3))/DETFB
      INVFB(3,1) = (FB(2,1)*FB(3,2) - FB(2,3)*FB(3,1))/DETFB
      INVFB(3,2) = (FB(1,2)*FB(3,1) - FB(1,1)*FB(3,2))/DETFB
      INVFB(3,3) = (FB(2,2)*FB(1,1) - FB(2,1)*FB(1,2))/DETFB
C
            FBT = TRANSPOSE(FB)
            INVFBT = TRANSPOSE(INVFB)
C
            DO I = 1, 2*MCRD
        DO J = 1, MCRD*MCRD
          Gs(I,J)  = 0.0
                                GsT(J,I) = 0.0
        ENDDO
      ENDDO
C
            CALL TANGSMS(Gs,FF,MCRD)
C
      GsT = TRANSPOSE(Gs)
            GB = MATMUL(Gs,B)
            EC = MATMUL(GB,U)
```

```
C     ************************
C     *** STRESS CALCULATION ***
C     ************************
      DO I = 1, 2*MCRD
        STRS(I) = 0.0
      ENDDO
      DO I = 1, MCRD*MCRD
        STRSG(I) = 0.0
      ENDDO
      DO I = 1, MCRD
        DO J = 1, MCRD
          STRGLB(I,J)  = 0.0
          STRGLOB(I,J) = 0.0
        ENDDO
      ENDDO
C
      STRS = MATMUL(C,EC)
C
      STRGLOB(1,1) = STRS(1)
      STRGLOB(2,2) = STRS(2)
      STRGLOB(3,3) = STRS(3)
      STRGLOB(2,1) = STRS(4)
      STRGLOB(1,2) = STRS(4)
      STRGLOB(1,3) = STRS(5)
      STRGLOB(3,1) = STRS(5)
      STRGLOB(2,3) = STRS(6)
      STRGLOB(3,2) = STRS(6)
C
      STRGLB = MATMUL(STRGLOB,IUNIT)
      STRSG(1) = STRGLB(1,1)
      STRSG(2) = STRGLB(1,2)
      STRSG(3) = STRGLB(1,3)
      STRSG(4) = STRGLB(2,1)
      STRSG(5) = STRGLB(2,2)
      STRSG(6) = STRGLB(2,3)
      STRSG(7) = STRGLB(3,1)
      STRSG(8) = STRGLB(3,2)
      STRSG(9) = STRGLB(3,3)
C     ***********************************
C     ****  FORMING Gs & Ms MATRICES  ****
C     ***********************************
      DO I = 1, MCRD**2
        DO J = 1, MCRD**2
          U_Ms(I,J) = 0.0
        ENDDO
      ENDDO
C
     DO I = 1, MCRD
       U_Ms(I,I) = STRSG(1)
       U_Ms(I+MCRD,I+MCRD) = STRSG(5)
       U_Ms(I+2*MCRD,I+2*MCRD) = STRSG(9)
       U_Ms(I+MCRD,I) = STRSG(4)
       U_Ms(I,I+MCRD) = STRSG(2)
       U_Ms(I+2*MCRD,I) = STRSG(7)
       U_Ms(I,I+2*MCRD) = STRSG(3)
       U_Ms(I+2*MCRD,I+MCRD) = STRSG(8)
       U_Ms(I+MCRD,I+2*MCRD) = STRSG(6)
     ENDDO
C     ****************************************
```

```
C     *** FORMING COHESIVE & CONTACT Bc MATRIX ***
C     ********************************************
      DO I = 1, MCRD
        DO J = 1, NDOFEL
          Bc(I,J)  = 0.0
          BcT(J,I) = 0.0
          BcRes(J,I) = 0.0
        ENDDO
      ENDDO
      DO I = 1, NNODE
        BcRes(6*I-5,1) = 0.0
        BcRes(6*I-4,2) = 0.0
        BcRes(6*I-3,3) = 0.0
        BcRes(6*I-2,1) = dNdx(I,4)*(HPOINT-ABS(U_PHI(I))/U_PHI(I))
        BcRes(6*I-1,2) = dNdx(I,4)*(HPOINT-ABS(U_PHI(I))/U_PHI(I))
        BcRes(6*I,3)   = dNdx(I,4)*(HPOINT-ABS(U_PHI(I))/U_PHI(I))
        Bc(1,6*I-2) = -2*dNdx(I,4)*(HPOINT-ABS(U_PHI(I))/U_PHI(I))
        Bc(2,6*I-1) = -2*dNdx(I,4)*(HPOINT-ABS(U_PHI(I))/U_PHI(I))
        Bc(3,6*I)   = -2*dNdx(I,4)*(HPOINT-ABS(U_PHI(I))/U_PHI(I))
      ENDDO
C
      BcT = TRANSPOSE(Bc)
C     *********************************
C     *** FORMING STIFFNESS MATRIX ***
C     *********************************
      DO I = 1, 2*MCRD
        DO J = 1, NDOFEL
          GB(I,J) = 0.0
                BTGT(J,I) = 0.0
              ENDDO
            ENDDO
C
            GB = MATMUL(Gs,B)
      BTGT = TRANSPOSE(GB)
C
            DO I=1, NDOFEL
            DO J=1, NDOFEL
            DO K=1, 2*MCRD
            DO L=1, 2*MCRD
              KMAT(I,J) = KMAT(I,J) +
     +     BTGT(I,K)*C(K,L)*GB(L,J)*WEIGHT*DETJ*WIDTH
      ENDDO
      ENDDO
      ENDDO
      ENDDO
C
            MsB = MATMUL(U_Ms,B)
            BTMsB = MATMUL(BT,MsB)
C
      DO I = 1, NDOFEL
        DO J = 1, NDOFEL
          KGEM(I,J) = KGEM(I,J) + BTMsB(I,J)*WEIGHT*DETJ*WIDTH
              ENDDO
            ENDDO
C
      DGBc = MATMUL(DGep,Bc)
            BcTDGBc = MATMUL(BcT,DGBc)
C
      DO I = 1, NDOFEL
```

```
        DO J = 1, NDOFEL
          KCON(I,J) = KCON(I,J) + BcTDGBc(I,J)*WEIGHT*DETJ*WIDTH
              ENDDO
          ENDDO
C
      DO I = 1, MCRD
        Trct(I) = 0.0
      ENDDO
C
      DO I = 1, MCRD
        DO J = 1, NDOFEL
          Trct(I) = TrcT(I) + DGBc(I,J)*(U(J)+DU(J,1))
              ENDDO
            ENDDO
C     ****************************
C     *** RESIDUAL CALCULATION ***
C     ****************************
            DO I = 1, MCRD*MCRD
        FF(I) = 0.0
      ENDDO
      DO I = 1, 2*MCRD
        EC(I)=0.0
      ENDDO
C
      DO I = 1, MCRD*MCRD
        DO J = 1, NDOFEL
          FF(I) = FF(I) + B(I,J)*(U(J)+DU(J,1))
              ENDDO
            ENDDO
C     ***********************************************
C     *** FORMING  GREEN-LAGRANGIAN & LARGE STRAIN  ***
C     ***********************************************
      DO I = 1, MCRD*MCRD
        IF (I .EQ. 1 .OR. I .EQ. 5 .OR. I .EQ. 9) THEN
          FF(I) = FF(I) + 1.0
        ENDIF
      ENDDO
C
      FB(1,1) = FF(1)
      FB(2,1) = FF(2)
      FB(3,1) = FF(3)
      FB(1,2) = FF(4)
      FB(2,2) = FF(5)
      FB(3,2) = FF(6)
      FB(1,3) = FF(7)
      FB(2,3) = FF(8)
      FB(3,3) = FF(9)
C
            DO I = 1, 2*MCRD
        DO J = 1, MCRD*MCRD
          Gs(I,J)  = 0.0
        ENDDO
      ENDDO
C
            CALL TANGSMS(Gs,FF,MCRD)
C
            GB = MATMUL(Gs,B)
            BTGT = TRANSPOSE(GB)
C
```

```
      DO I=1, MCRD
        DO J=1, MCRD
          CSTRN(I,J) = 0.0
          EEC(I,J) = 0.0
        ENDDO
      ENDDO
C
      DO I=1, MCRD
        DO J=1, MCRD
          DO K=1, MCRD
            CSTRN(I,J) = FB(K,I)*FB(K,J)+CSTRN(I,J)
          ENDDO
        ENDDO
      ENDDO
      DO I=1, MCRD
        DO J=1, MCRD
          IF (I .EQ. J) THEN
            EEC(I,J) = 0.5*CSTRN(I,J)-0.5
          ELSE
            EEC(I,J) = 0.5*CSTRN(I,J)
          ENDIF
        ENDDO
      ENDDO
C
      EC(1) = EEC(1,1)
      EC(2) = EEC(2,2)
      EC(3) = EEC(3,3)
      EC(4) = EEC(1,2)
      EC(5) = EEC(2,3)
      EC(6) = EEC(3,1)
C
      STRS = MATMUL(C,EC)
C
C     XFEM ELEMENTS RESIDUAL FORCES DUE TO LARGE DEFORMATION
C
      DO I=1, NDOFEL
            DO J=1, 2*MCRD
              RHS(I,1) = RHS(I,1) -
     +            BTGT(I,J)*STRS(J)*WEIGHT*DETJ*WIDTH
        ENDDO
      ENDDO
C
C     XFEM RESIDUAL FORCES DUE TO COHESIVE REGION OR CONTACT INTERFACE
C
      DO I=1, NDOFEL
            DO J=1, MCRD
              RHS(I,1) = RHS(I,1) +
     +            BcRes(I,J)*Trct(J)*WEIGHT*DETJ*WIDTH
          RHSC(I) = RHSC(I) +
     +            BcRes(I,J)*Trct(J)*WEIGHT*DETJ*WIDTH
        ENDDO
      ENDDO
     ENDDO ! END IF LOOP OVER GAUSS POINTS
C     ************************************
C     *** FORMING RIGHT-HAND-SIDE MATRIX ***
C     ************************************
     AMATRX = KMAT + KGEM  + KCON
     RETURN
     END
```

Appendix B: Experimental Calculations According to ASTM D5528-01 [97]

Double Cantilever Beam (DCB) Test:

I. The Modified Beam Theory (MBT) Method:

Based on the beam theory expressions, the critical energy release rate for the DCB test is written as follows [97] (see also Figure 1-4):

$$G_{IC} = \frac{3P_{grip}\Delta}{2wa_{cr}} \tag{B-1}$$

where P_{grip}, Δ, w and a_{cr} are the applied load, the displacement of the load, specimen width and the delamination length, respectively. Due to possible rotation in the crack tip front, which is neglected in standard beam theory, a correction factor is considered by treating the test with a longer crack length, $a_{cr}+\Delta a_{cr}$. To determine the crack length increase, Δa_{cr}, experimentally, the cube root ratio of the opening displacement over the applied load, known as beam compliance, must be plotted versus delamination length, a_{cr}, at onset of all delamination propagations. The least square root method should then be utilized to find the y-intercept which is equal to the crack length increase. By substituting the new crack length into the above beam theory equation, one obtains:

$$G_{IC} = \frac{3P_{grip}\Delta}{2w(a_{cr} + \Delta a_{cr})} \tag{B-2}$$

II. The Compliance Calibration (CC) Method:

In the compliance calibration (CC) method, the least squares of $\log(\frac{\Delta}{P_{grip}})$ versus $\log(a_{cr})$ at onset of all delamination propagations must be plotted and the slope of this line, *n*, is implemented to correct the energy release rate:

$$G_{IC} = \frac{nP_{grip}\Delta}{2wa_{cr}} \tag{B-3}$$

III. The Modified Compliance Calibration (MCC) Method:

In the modified compliance calibration (CC) method, the normalized delamination length over the thickness versus the cube root ratio of opening displacement over the applied load at onset of all delamination propagations must be plotted and the slope of this line, m_{Line}, is implemented to calculate the energy release rate:

$$G_{IC} = \frac{3P_{grip}{}^{2}(\frac{\Delta}{P_{grip}})^{2/3}}{2m_{Line}wt_{ck}} \tag{B-4}$$

where t_{ck} is the specimen thickness.

Finally, in order to account for shortening of arm of moment and the rotation of the loading block, a large displacement correction factor should be multiplied into the energy release value calculated from either of the above methods. This correction factor is calculated as follows:

$$A_{large} = 1 - \frac{3}{10}\left(\frac{\Delta}{a_{cr}}\right)^2 - \frac{3}{2}\left(\frac{\Delta\left(\frac{t_{ck}}{4} + \frac{t_{Block}}{2}\right)}{a_{cr}}\right) \tag{B-5}$$

where t_{Block} is the loading block thickness.

End Notch Flexure (ENF) Experimental Test:

Similar to the DCB test, for ENF test data the compliance method is employed to calculate the critical energy release rate [19]:

$$G_{IIC} = \frac{9 a_{cr}{}^2 P_{grip}{}^2}{2 E_{Longitudinal} w^2 t_{ck}{}^3} \tag{B-6}$$